NUMERICAL MODELING AND ANALYSIS OF FLOW AROUND STATIONARY AND OSCILLATING CIRCULAR CYLINDER

NIAZ BAHADUR KHAN

FACULTY OF ENGINEERING
UNIVERSITY OF MALAYA
KUALA LUMPUR

2018

NUMERICAL MODELING AND ANALYSIS OF FLOW AROUND STATIONARY AND OSCILLATING CIRCULAR CYLINDER

NIAZ BAHADUR KHAN

THESIS SUBMITTED IN FULFILMENT OF THE REQUIREMENTS FOR THE DEGREE OF DOCTOR OF PHILOSOPHY

FACULTY OF ENGINEERING
UNIVERSITY OF MALAYA
KUALA LUMPUR

2018

UNIVERSITY OF MALAYA

ORIGINAL LITERARY WORK DECLARATION

Name of Candidate: Niaz Bahadur Khan

Matric No: KHA140047

Name of Degree: Doctor of Philosophy

Title of Project Paper/Research Report/Dissertation/Thesis: Numerical Modeling and Analysis of Flow around Stationary and Oscillating Circular Cylinder

Field of Study: Structural Engineering & Materials

 I do solemnly and sincerely declare that:

(1)   I am the sole author/writer of this Work;
(2)   This Work is original;
(3)   Any use of any work in which copyright exists was done by way of fair dealing and for permitted purposes and any excerpt or extract from, or reference to or reproduction of any copyright work has been disclosed expressly and sufficiently and the title of the Work and its authorship have been acknowledged in this Work;
(4)   I do not have any actual knowledge nor do I ought reasonably to know that the making of this work constitutes an infringement of any copyright work;
(5)   I hereby assign all and every rights in the copyright to this Work to the University of Malaya ("UM"), who henceforth shall be owner of the copyright in this Work and that any reproduction or use in any form or by any means whatsoever is prohibited without the written consent of UM having been first had and obtained;
(6)   I am fully aware that if in the course of making this Work I have infringed any copyright whether intentionally or otherwise, I may be subject to legal action or any other action as may be determined by UM.

Candidate's Signature   Date:

Subscribed and solemnly declared before,

Witness's Signature   Date:

Name:

Designation:

NUMERICAL MODELING AND ANALYSIS OF FLOW AROUND STATIONARY AND OSCILLATING CIRCULAR CYLINDER

ABSTRACT

The fluid–structure interaction problems associated between cylinder and fluid has gained considerable attention because of its importance in a wide range of applications including marine equipment, nuclear reactors, skyscrapers, bridges, wind turbines and chimneys. When a flow passes through a circular cylinder, vortex shedding would occur behind the cylinder alternately at the top and bottom sides resulting in an unwanted structural vibration, especially when the frequency of vortex shedding is equal to or near to the natural frequency of the structure. This phenomenon is known as a vortex-induced vibration (VIV). Despite the wide range of research on flow around cylinder at Reynolds number 3900, the study of mesh density in spanwise direction, use of cost effective turbulent model and impact of mesh pattern on flow around cylinder problems is limited. Flow around fixed cylinder provide basis for the VIV problem which is associated with oscillating cylinder case. The main objective of this study is to numerically investigate the unsteady nature of the flow around cylinder using computational fluid dynamics. This study is divided into two parts: fixed cylinder case and oscillating cylinder case. The first section analysed the effects of the spanwise domain, the spanwise mesh resolution and mesh resolution near-field grid on the recirculation length, the angle of separation and hydrodynamic coefficients. The effects of non-dimensional timestep and time statistic average on the accuracy of the statistical quantities are also investigated. In the first section, extensive numerical simulations have been performed using large eddy simulation (LES) code and Smagorinksy–Lilly SGS models to investigate the unsteady nature of the flow around a fixed cylinder at a Reynolds number (Re)=3900. Meshing and analysis are performed using ICEM-CFD

and an ANSYS-fluent tool, respectively. The second section mainly focused on the VIV phenomenon for elastically mounted rigid cylinders. The objective of this section is to test the capability and accuracy of 2D and 3D RANS models to compute the maximum amplitude, the mode of vortex, and other hydrodynamic coefficients, and compare the performance of these models to that of computationally expensive models. In addition, the performance and capability of SST-kω is compared with realizable-kε (RKE) equations. In this study, a user-defined function code written in C language is used to facilitate the oscillation of the cylinder and record the fluid forces with the amplitude of the cylinder through dynamic mesh update method. Several important results are obtained in this study. For the fixed cylinder, the mesh density in the spanwise domain and near-field grids significantly affect the calculation of the recirculation length, the angle of separation, the hydrodynamic coefficients and the statistic in the wake region behind the cylinder. In addition, the recirculation length is observed to be a key parameter for assessing the accuracy of the numerical method. For the oscillating cylinder, the 2D RANS SST k-ω turbulent model, which is relatively less expensive, can predict the hydrodynamic forces, the maximum amplitude and all modes of the vortex at Re=10^4. In the RKE model, a delayed transition is observed between the upper and lower branches, resulting in the broad range of the 'lock-in' region. With very small mass-damping ratio, the 2D RANS SST k-ω turbulent model successfully predicted the maximum amplitude during the VIV analysis. The findings of this study significantly reduced the computational cost for the flow around fixed and oscillating cylinders.

Keywords: Flow around cylinder, Reynolds number, computational fluid dynamic, vortex induced vibration, numerical.

PERMODELAN BERANGKA DAN ANALISA BAGI ALIRAN DI KELILING SILINDER BULAT TETAP DAN BERAYUN

ABSTRAK

Masalah interaksi cecair-struktur yang berkaitan antara silinder dan bendalir telah mendapat banyak perhatian daripada para penyelidik kerana kepentingannya dalam pelbagai aplikasi yang merangkumi peralatan marin, reaktor nuklear, bangunan pencakar langit, jambatan, turbin angin dan cerobong. Apabila aliran melalui silinder bulat, pembentukan vorteks (vortex shedding) akan berlaku di belakang silinder berselang-seli di bahagian atas dan bawah yang boleh menyebabkan getaran struktur yang tidak diingini, terutamanya apabila frekuensi bagi pembentukan vorteks adalah sama dengan atau berhampiran dengan frekuensi semula jadi struktur. Fenomena ini dikenali sebagai vorteks penyebab getaran (VIV). Walaupun terdapat pelbagai penyelidikan mengenai aliran di sekitar silinder pada nombor Reynolds 3900, kajian ketumpatan jejaring dalam arah rentang, penggunaan kos model bergelora yang berkesan dan kesan corak jejaring pada masalah aliran di sekitar silinder adalah terhad. Aliran disekitar silinder tetap menyediakan asas bagi masalah VIV yang berkaitan dengan kes silinder berayun. Objektif utama kajian ini adalah untuk menyiasat secara berangka sifat tak tetap bagi aliran di sekeliling silinder menggunakan pengiraan dinamik bendalir. Kajian penyelidikan ini di bahagikan kepada dua bahagian; kes silinder tetap dan kes silinder berayun. Bahagian pertama menganalisa kesan domain arah rentang, resolusi jejaring arah rentang dan resolusi jejaring grid kawasan-dekat bagi panjang edaran semula, sudut pemisahan dan pekali hidrodinamik. Kesan bagi step-masa tanpa-dimensi dan purata statistik masa bagi ketepatan kuantiti statistik juga di siasat. Dalam bahagian pertama kajian, simulasi berangka menyeluruh telah dilakukan untuk menyiasat sifat tak mantap aliran di sekeliling silinder tetap di nombor Reynolds = 3900 menggunakan kod simulasi eddy besar (LES) dan model SGS Smagorinksy-lilly. Jejaring dan analisis dilakukan dengan menggunakan ICEM-CFD dan alat ANSYS-fluent, masing-masing.

Bahagian kedua kajian memberi tumpuan kepada fenomena VIV untuk silinder tegar dipasang anjal. Objektif bagi bahagian ini adalah untuk menguji keupayaan dan ketepatan model 2D dan 3D RANS dalam mengira amplitud maksimum, mod vorteks dan lain-lain pekali hidrodinamik dan membandingkan prestasi model-model ini dengan model-model pengiraan yang mahal.

Tambahan lagi, prestasi dan keupayaan SST-kω juga di bandingkan dengan persamaan nyata-kε (RKE). Dalam kajian ini, kod fungsi ditakrif-pengguna (UDF) ditulis dalam bahasa C telah digunakan untuk memudahkan ayunan silinder dan merekodkan daya cecair dengan amplitud silinder menggunakan kaedah kemaskini jejaring dinamik. Beberapa keputusan penting telah dihasilkan dari kajian ini. Bagi silinder tetap, ketumpatan jejaring dalam domain arah rentang dan grid kawasan-dekat mempunyai kesan yang besar ke atas kiraan panjang edaran semula, sudut pemisahan, pekali hidrodinamik dan statistik di rantau bangun di belakang silinder. Tambahan lagi, panjang edaran semula adalah parameter penting untuk menilai ketepatan kaedah berangka. Bagi silinder berayun, 2D RANS SST k-ω model bergelora, yang agak lebih murah, mempunyai keupayaan untuk meramalkan daya hidrodinamik, amplitud maksimum dan semua mod vorteks di nombor Reynolds = 10^4. Bagi model nyata-kε, diperhatikan terdapat kelewatan transisi di antara cawangan atas dan bawah, yang menyebabkan julat yang lebar bagi kawasan 'tertutup'. Dengan nisbah jisim-redaman yang sangat kecil, 2D RANS SST k-ω model gelora berjaya meramalkan amplitud maksimum semasa analisa VIV. Dapatan dari kajian ini mengurangkan kos pengiraan dengan amat ketara untuk aliran di sekitar silinder tetap dan silinder berayun.

Kata kunci: Aliran di sekeliling silinder; nombor Reynolds; pengiraan dinamik bendalir; vorteks mencetuskan getaran (VIV); berangka.

ACKNOWLEDGEMENTS

TABLE OF CONTENT

LIST OF FIGURES

LIST OF TABLES

LIST OF SYMBOLS AND ABBREVIATIONS

St	:	Strouhal number
D	:	Diameter of cylinder
f_v	:	Vortex shedding frequency
f_n	:	Cylinder natural frequency
U	:	Uniform inlet velocity
U_r	:	Reduced velocity
CFD	:	Computational fluid dynamics
VIV	:	Vortex-Induced Vibration
Re	:	Reynolds number
F_D	:	Drag force
F_L	:	Lift force
m^*	:	Mass ratio
ρ	:	Density
ζ	:	Damping ratio
c	:	Damping coefficient
$ω_n$	:	Natural angular frequency
Δt	:	time step
FSI	:	Fluid-structure interaction
LES	:	Large Eddy Simulation
RANS	:	Reynold Average Navier Stoke
DNS	:	Direct Numerical Simulation
C1	:	Case Study 1
C2	:	Case Study 2
Cs	:	Smagorinsky constant

C	:	Number of elements at Circumference of cylinder
Δ	:	Filter
R	:	Number of elements in radial direction of near field grid
PIV	:	Particle image velocimetry
Lr/D	:	Recirculation length
θs	:	Angle of separation

CHAPTER 1: INTRODUCTION

1.1 Research Background

Over the past few decades, flow around circular cylinder is one of the highly research topic in the field of offshore engineering and fluid-structure interaction (FSI). This topic received interest after the dramatic collapse of the Tacoma Narrows Bridge in 1940 because of a vortex induced vibration phenomenon (VIV) [Figure 1.1]. VIV is a widely encountered hydrodynamic phenomenon caused by the excitation of the vortex shed from bluff bodies. This phenomenon results in excessive stresses and the reduction of fatigue life, both of which may be responsible for the complete collapse of or partial damage to the structures. Chimney stacks, heat exchangers, skyscrapers, towers, pipes and bridges are examples of structures which may collapse or be damaged by unwanted VIV phenomenon. In the past few decades, the global inclination toward deep-sea oil production has heightened the need to investigate and predict the VIV of offshore structures. Insufficient knowledge on the design and construction of offshore structures lead to higher cost because of the application of numerous safety factors.

(a)   (b)
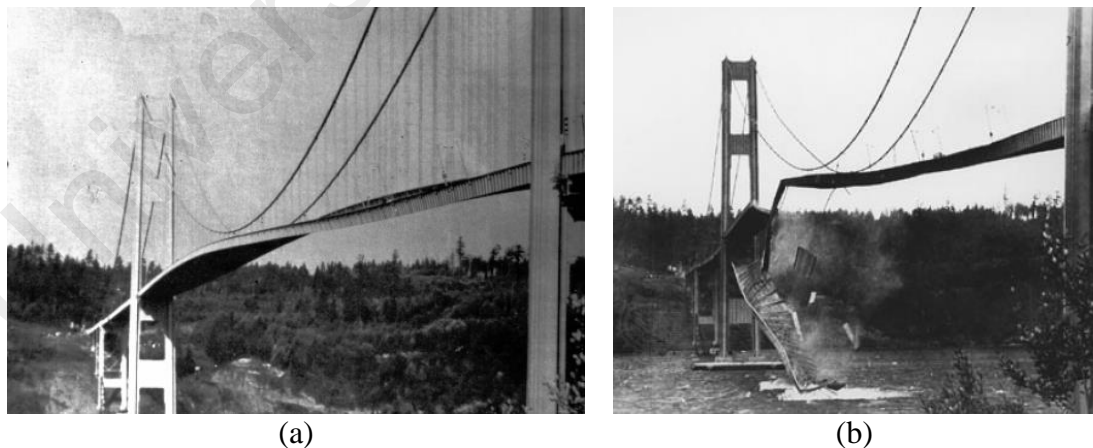
Figure 1.1: Tacoma Narrow bridge collapse

The collapse of the Tacoma Narrow Bridge has highlighted the need to assess the influence of wind forces in the design. VIV, which may result in large oscillations, cannot be underestimated in the design of long and slender structures. In addition,

pseudo-static design analysis cannot adequately address the disastrous aerodynamic vibration. Towers, skyscrapers and suspensions bridges are applications of VIV in structural engineering. Farquharson, Smith, & Vincent, (1950), Karman, (1938) and Amann (1941) are pioneers in this field who implemented the airfoil theory to bridge decks. In 1995, the failure in the thermowells of Japanese nuclear reactors (Monju) was due to VIV. In 2002, one of the towers of the thriller ride VertiGo at Cedar Point in Sandusky, Ohio, collapsed because of VIV. These major incidents further motivated researchers to minimize the unwanted VIV during the construction of towers and other structures. Wind turbines are also FSI field applications.

The offshore industry is facing the problem of VIV because of the usage of long slender structures, pipes and risers. Given that energy reservoirs are depleting at exponential rates, therefore, such deposits must be increasingly developed in considerably deeper water. Conventional fixed jacket-type and bottom-supported compliant platforms were found inefficient for exploring these resources. Floating platforms in which the mooring system constituted of tethers were suitable alternatives for deep water regions [Figure 1.2]. The structure behaved as a rigid cylinder in the vertical direction and as a flexible cylinder in the horizontal direction. The long, slender and flexible risers used to transport fluids from the seabed to the surface were subjected to wave, current and wind loading, all of which probable caused the VIV and the ultimate failure. Specifically, the effect of the current on the riser increases with water depth, suggesting that it may be the main contributor towards riser failure due to VIV (Bourdier, 2008). Therefore, the non-linearity present under wind, wave and current loading must be identified and analysed. In pipe joint failures in the offshore industry, VIV is responsible for excessive fatigue loading and to some extent for the external loading (internal pressure, axial loading and bending loading), which may result in major safety concerns, environmental hazards and economic loss.
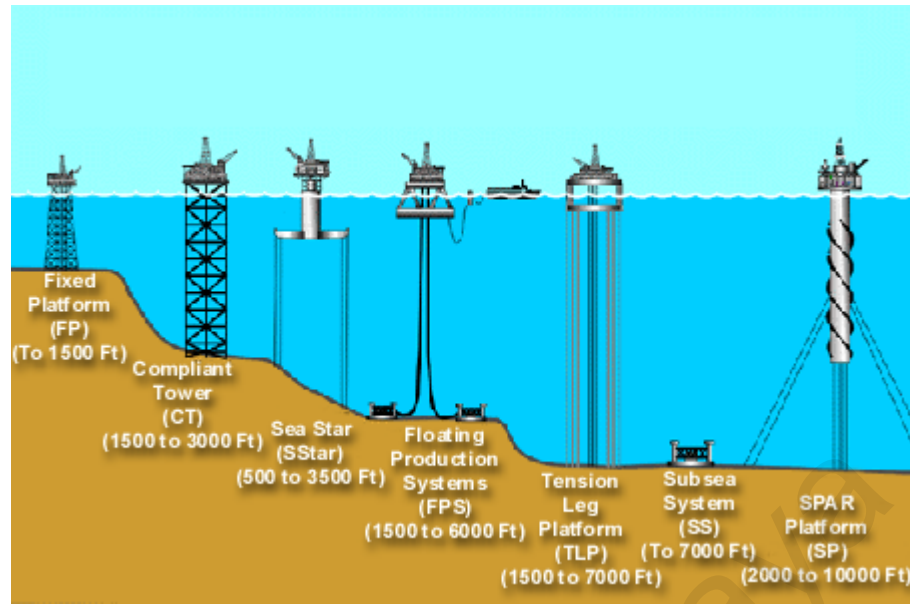
Figure 1.2: Types of offshore platform (Skaug, 1998)

1.2 Problem statement

Many offshore structures, such as spar hulls, risers and pipelines, are of circular cylindrical shape. As such, the flow around circular cylinders has been extensively investigated in the offshore and marine hydrodynamic fields. Experimental testing is hindered by several limitations, such as lengthy processing, hazardous to the environment, expensive apparatus, and highly skilled labour requirement. Computational fluid dynamics (CFD) simulations is an excellent alternative to overcome the inherent limitations of the experimental approach. Despite the rapid advancements in the computational field, CFD analysis has several drawbacks, such as complex flow behaviour, unrealistic computational cost for 3D problems, selection of appropriate turbulent model, use of optimum mesh, and different assumptions. To address the limitations of CFD, the computational skills must be improved through proper simplification techniques, the appropriate utilization of comparatively less expensive turbulent models and the use of optimum mesh technique, all of which would increase the reliability, accuracy and confidence of the numerical simulation tools. The complex nature of the flow around a cylinder makes it an excellent case for assessing

the ability of computational packages and for extending the study to real environmental flow conditions. Flow around fixed cylinder at Reynolds number=3900 has been widely study both numerically and experimentally but still number of parameters , like size of spanwise domain, temporal discretization, mesh density near flow-field and in spanwise direction, need to be investigated in detail. The flow through fixed cylinders provides the basic dynamic flow, vortex formation and shedding, which are also important factors in the flow through oscillating cylinders. Previously, the VIV phenomenon at high Reynolds number has been investigated using detached eddy simulation (DES) and Large eddy simulation model (LES) which are computationally expensive and cannot be extended to upper critical and trans-critical Reynold range.

1.3 Research Objectives

This study mainly focused on evaluating the capability of different turbulent models and mesh resolutions to extract the results for flow around circular cylinders at different Reynolds number. The main objectives of this study were:

(1) To investigate the effects of spanwise-length, mesh resolution in the span-wise direction and near-field grid on the flow around fixed cylinders by using a large eddy simulation model.

(2) To analyse the effects of averaging time and non-dimensional timestep on the computing recirculation length, the angle of separation, the hydrodynamic coefficients and other statistical quantities in the flow around fixed cylinder cases.

(3) To analyse the accuracy and capability of the RANS SST k-ω turbulent model to predict the flow dynamics around a fixed cylinder at $Re=10^4$ and extend the study to a cylinder that is free to oscillate in the transverse direction and has a low mass-damping ratio.

(4) To compare the performance of the Reynolds averaged Navier-Stokes equation (RANS) SST k-ω and Realizable k-ε (RKE) turbulent model in assessing the VIV of an elastically mounted rigid circular cylinder that is free to oscillate in the cross-flow direction at Re=10^4 and has a low mass ratio. The hydrodynamic coefficients and the vortex shape were analysed as well.

(5) To numerically investigate VIV of an elastically mounted rigid cylinder, possessing very low mass-damping ratio, for the range of reduced velocity Ur= 2 to 16, and Reynolds number Re = 1700 to 14000, by using a RANS SST-kω model. The results were validated against the available experimental and numerical results.

1.4 Scope of the Study

This study investigated the flow around circular cylinders by using computational fluid dynamics. This study investigated the dynamic flow characteristics around cylindrical structures with minimal computational costs in the subcritical regime. The numerical study evaluated the capability of different turbulent models as well as the effects the non-dimensional time-step, the averaging vortex shedding time, the spanwise mesh resolution, the near-field grid and the spanwise domain on the flow characteristics and hydrodynamic forces of the structure. Finally, this study analysed the structural vibration caused by vortex shedding when the cylinder oscillated in the cross-flow direction.

1.5 Significance of Research

The study of the flow around fixed cylinder provides basis for analysing the VIV problems in which the cylinder is free to oscillate. The flow around a fixed cylinder at Re=3900 come under the lower subcritical flow regime, which is highly sensitive in terms of flow separation, boundary layer nature, recirculation length, wake characteristics, and other hydrodynamic coefficients. This study identified the main

parameters influencing the accuracy of the results and the convergence of the numerical method. The findings suggested that the computational cost for analysing the flow around cylinders in the subcritical regime could be reduced significantly. The result produced by the Reynolds averaged Navier-Stokes equation (RANS) SST k-ω verified the effectiveness of the computationally less expensive 2D model and facilitated more complex analyses at high Re values.

1.6 Thesis structure

Chapter 1 presents research background, problem statement, scope of the work, research objectives and significance of the study.

Chapter 2 reviews the previous experimental and numerical studies in the literature. The researchers' views about the effects of different parameters on the flow around cylinders are also discussed.

Chapter 3 describes about the computational fluid dynamics analysis procedure and the methodology. The basic governing equations, spatial discretization and temporal discretization are explained in detail.

In Chapter 4, a flow around a stationary cylinder was carried out at Re=3900 by using large eddy simulation code. In addition, this chapter provides a detailed review of every step and analysis is performed on the basis of the recommendation of the previous studies. The effects of spanwise length and mesh resolution in the spanwise direction and near-field grid were examined. In the second section, the effects of non-dimensional timestep and averaging time were analysed. The discrepancies in previous results with present findings were discussed.

Chapter 5 presents the CFD analysis of a fixed cylinder at Re=10^4 and a cylinder that is free to oscillate in the transverse direction by using the Reynolds-averaged Navier-

Stokes (RANS) shear–stress-transport SST k-ω model. For the oscillating cylinder, simulations were performed for elastically mounted rigid cylinders with a low mass-damping ratio. The numerical results for the 2D and 3D RANS models were compared with the experimental results and the 3D expensive model results available in the literature. The mode of vortex, dimensionless amplitude ratio and other hydrodynamic coefficients were discussed in detail. In the second section of the chapter, VIV was investigated using the realizable k-ε (RKE) model. The results obtained by the realizable k-ε (RKE) model were compared with those by the SST k-ω model. In the final section of the chapter, VIV was investigated for a range of Re values from 1700 to 14000 at a very low mass damping ratio by using the 2D RANS SST k-ω model, and the results were validated against the experimental results available in the literature.

Chapter 6 presents the conclusions and outcomes of the case studies. Recommendations for future studies were also provided.

CHAPTER 2: LITERATURE REVIEW

2.1 Introduction

VIV is an important phenomenon associated with the flow around a cylinder. This phenomenon is linked with the complexity of the viscous flow around a cylinder and the dynamic interaction with the structure. A scenario in which the frequency of the vortex shedding in the wake is equal or approximate to the natural frequency of the bluff body would result in a lock-in phenomenon. In the lock-in range, the severity of the VIV problems becomes significant because of the high amplitude of the oscillation of the cylinder. Moreover, given that the lift coefficient has a greater amplitude than that of the drag coefficient, VIV is more severe in the cross-flow direction. Therefore, most of the previous studies on VIV was limited to a fixed amplitude and a single degree of freedom. As such, these studies were limited to the effects of the frequency and amplitude by producing the sinusoidal motion to analyse the wake states and forces on the cylinder. This chapter presents a detailed review of previous experimental and numerical studies in the literature. The researchers' observations on the effects of different non-dimensional parameters on the flow around cylinders are discussed in detail.

2.2 Vortex shedding and flow regimes

As fluid particles strike the front surface of a cylinder, the pressure in the fluid particle is increased from free stream pressure to stagnation pressure. The boundary layer developed on both sides of the cylinder and the high pressure of the fluid particles attempt to induce the flow around the cylinder. At the widest section of the cylinder, the boundary layer detaches from the surface of the cylinder, resulting in two shear layers which bound on the wake on each side. These shear layers lead to a rolling behaviour because of the pressure difference between the innermost (which is in contact with cylinder) and outermost (near free flow) layers. In turn, this rolling behaviour leads to

swirling vortices (Perry, Chong, & Lim, 1982; Williamson & Roshko, 1988) which produce regular and periodic patterns of the vortex known as Vortex Street or Karman Vortex Street. This phenomenon is also known as vortex shedding. The interaction of these vortices with the cylinder is the primary source of the VIV (explained in section 2.2.3 Vortex induced vibration).

The flow behaviours around a circular cylinder is complex in nature and mainly depends on the inlet boundary condition, geometry shape and viscosity of the fluid. All of these important parameters are described by the dimensionless parameter known as Re (Re=U*D_o/υ, where U is the inlet velocity, D_o is the characteristic length and υ is the kinematic viscosity). According to potential flow theory, the streamlines and pressure distribution for the ideal fluid flow around a cylinder can be defined as shown in Figure 2.1. Fluid velocity remains constant in the upstream and downstream stagnation points. The pressure distribution for both the ideal fluid (potential flow theory) and the experimental results are shown in Figure 2.1a. As shown, the pressure distribution for the ideal fluid was symmetric, which leads to a zero drag. The symmetrical pressure distribution around the cylinder is due to the absence of the effect of the viscous layer. By contrast, in the experimental results (Achenbach, 1968), the distribution is asymmetrical because of the presence of viscous flow. The zero drag phenomenon is also known as d'Alembert's paradox.

| (a) Ideal streamlines flow | (b) Pressure distribution around cylinder |
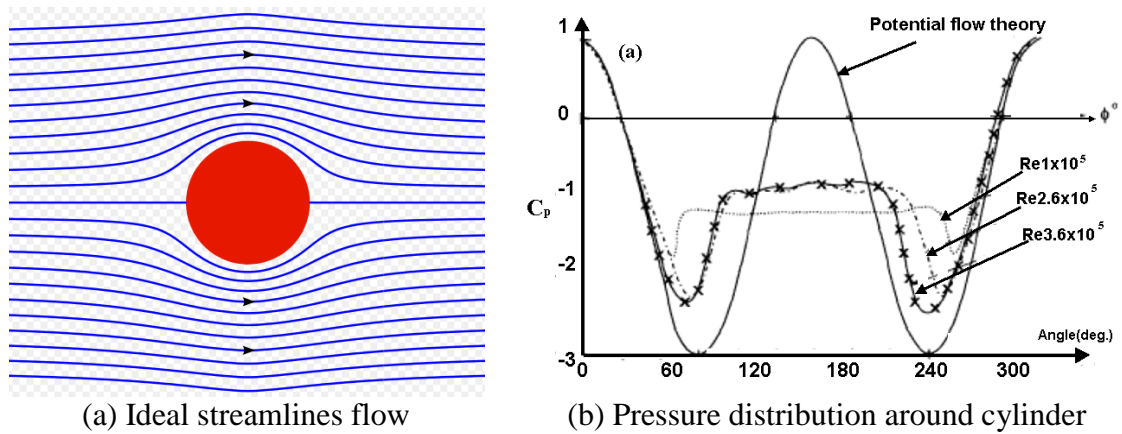
Figure 2.1: Ideal streamline and pressure distrubution around bluff body or cylinder (Achenbach, 1968)

Fluid flow passing through the bluff bodies is divided into two categories: the boundary layer (near the surface of the body) and the outer region (outside region of BL). The inner layer is further categorized into three layers: viscous sub-layer, buffer layer region and fully turbulent region or low-lag region (Figure 2.2). In the viscous sub-layer, the molecular viscosity plays a key role in momentum and mass transfer, whereas turbulence plays a dominant role in the outer layer (fully turbulent layer). In the buffer layer or blending region, which is located between the viscous sub-layer and the fully turbulent layer, the effects of both molecular viscosity and turbulence is significant.
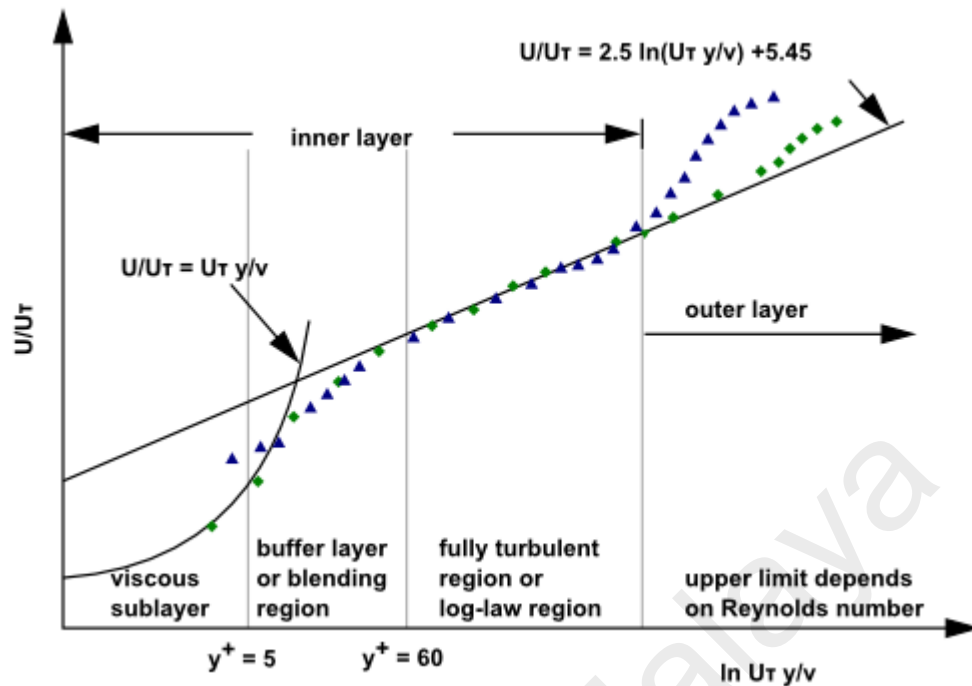
Figure 2.2: Near-wall regions (ANSYS Inc. ANSYS Elements manual)

In view of adverse pressure gradient around the cylinder, the characteristics of the viscous flow around the body are complex in nature, and the flow separation at the downstream of the cylinder depends on the Re. The flow around bluff bodies (e.g. subsea pipes) are subject to boundary layer separation, which is accompanied by the formation of eddies in the wake behind the cylinder. The nature of the wake and the boundary layer (i.e. whether laminar, partially turbulent or fully turbulent) depend on the regime of the Re.

Figure 2.3 shows the flow regimes for the fluid flow around a circular cylinder, as summarized by Sumer and Fredsøe (1997). Figure 2.4 shows a schematic explaining the definition of the boundary layer, the wake region and the angle of separation in the case of a flow across a cylinder. Based on the cylinder diameter, at very small Re (Re<5), the fluid follows the cylinder curvature, and no separation would occur. This flow is laminar, which is also known as 'creeping flow'. The separation begins at Re>5 from

the back of the cylinder, as shown in Figure 2.3b. As the Re increased, the flow changed from laminar to turbulent, and a pair of vortices formed in the wake. In the Re range of 5<Re<40, a flow separation is initiated from the back of the cylinder, and a fixed pair of symmetric vortices is formed in the wake of the cylinder. The length of the vortex formation varied with the Re (Batchelor, 1970). In the Re range of 40<Re<200, the vortex street remains laminar, and 2D analysis can be applied to study the wake characteristics behind the cylinder. According to Williamson (1989), the shedding in this regime is 2D, implying that the wake characteristics in the spanwise direction need not be studied. In the Re range of 200<Re<300, the wake transition from laminar to turbulence behaviour, although the boundary layer over the surface of the cylinder remains laminar in this regime.

	Flow characteristic	Reynolds number	Flow regime
(a)		$Re < 5$	Creeping flow
(b)		$5 < Re < 40$	
(c)		$40 < Re < 200$	
(d)		$200 < Re < 300$	
(e)		$300 < Re < 3 \times 10^5$	Sub-critical
(f)		$3 \times 10^5 < Re < 3.5 \times 10^5$	critical (lower-transition)
(g)		$3.5 \times 10^5 < Re < 1.6 \times 10^5$	Super Critical
(h)		$1.6 \times 10^5 < Re < 4 \times 10^6$	Upper Critical
(i)		$Re < 4 \times 10^6$	Transcritical

Figure 2.3: Regimes of fluid flow around smooth circular cylinder (Sumer & Fredsøe, 1997)
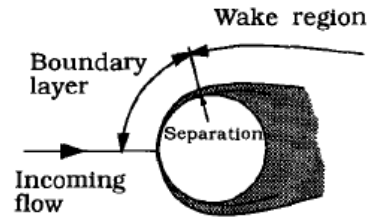
Figure 2.4: Boundary layer, wake region and separation definition (Sumer & Fredsøe, 1997)

The Re regime of $300 < Re < 3 \times 10^5$ is known as the subcritical flow regime. According to Bloor (1964), the wake is completely turbulent and varies in the span-wise direction at Re>300. A 3D analysis is necessary to capture the wake turbulence characteristics. The vortex shedding in this regime is strong, and the boundary layers detach at 80° at the nose of the cylinder. With further increase in Re, the transition to turbulence is initiated in the boundary layer at the point where flow separation occurs. The transition to turbulence increases with increasing Re and shifts upstream towards the stagnation point. In the Re range of $3 \times 10^5 < Re < 3.5 \times 10^5$, which is also known as the critical flow regime, the boundary layer towards one side of the cylinder become turbulent, whereas the other side remain laminar. In the range of $3.5 \times 10^5 < Re < 1.5 \times 10^6$, which is also known as the supercritical flow regime, the cylinder boundary layer becomes turbulent on both sides of the cylinder, and the separation point moves to 140°. At $Re=1.5 \times 10^6$, the boundary layer becomes fully turbulent on one side and partly turbulent and partly laminar on the other side. The Re band of $1.5 \times 10^6 < Re < 4.5 \times 10^6$ is also known as the upper transition flow regime. At $Re > 4.5 \times 10^6$, the boundary layer becomes completely turbulent everywhere. This regime is called the trans-critical regime.

2.2.1 Vortex formation and shedding process

As mentioned in a previous section, a pair of vortices formed at Re>40 because of the adverse pressure gradient around the cylinder curvature. These pairs of vortices are very unstable when exposed to small disturbances. As such, one vortex grows stronger than the other. Figure 2.5 shows the development details during the vortex shedding, as explained by Sumer and Fredsøe (1997). These two vortices have opposite rotation directions, but the inner sides of the vortices have the same velocity vector direction. As shown in Figure 2.5a, vector A (clockwise direction) grow sufficiently strong to draw vector B (anti-clockwise direction) into the wake. The supply of vorticity from the boundary layer of vortex A to vortex A is cut off by vortex B, and vortex A is shed in the wake. In the next step [Figure 2.5c], vortex B becomes sufficiently strong to draw vortex C into the wake, and vortex C then cut off the supply of vorticity to vortex B, resulting in the shedding of vortex B in the downstream. The vortex shedding continues alternately in the same manner on both sides of the cylinder, resulting in the formation of a Vortex Street in the wake.

The preceding discussion suggested that the interaction between the two shear layers is mainly responsible for the vortex shedding. If the interaction between the shear layers is terminated by any means, such as making the cylinder surface rough or keeping the splitter plate at the downstream portion of the cylinder, vortex shedding would be prevented. In addition, if the cylinder is kept close to a wall, then the shear layer close to the wall-side will become weaker than that formed on the counter side of the cylinder, thereby weakening the vortex shedding as well.

.
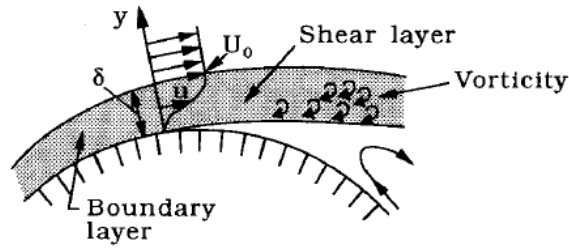
Detailed picture of
flow near separation

(a)
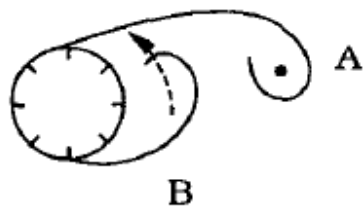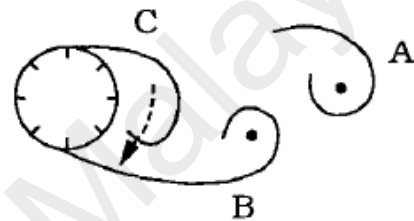
(b)   (c)

Figure 2.5: Vortex shedding mechanism (Sumer & Fredsøe, 1997)

2.2.2 Type of vortex shedding mode

The classifications of the different vortex modes presented herein were defined previously in literature (Jauvtis & Williamson, 2004; Williamson & Roshko, 1988).

- 2S mode: Each half cycle result in a single vortex shedding into the wake

- 2P mode: Each half cycle result in a pair of vortex shedding into the wake

- P+S mode: One pair and one single vortex shedding into the wake occur during each half cycle.

- $2P_o$ mode: This mode differed from 2P mode in a way that the secondary vortex in each pair is much weaker than the primary vortex.

- 2P+2S: This mode also has vortex pairs on each side of the cylinder but a single vortex appeared after each pair of vortex.

- 2T mode: Three vortices formed during each half cycle.

16

- 2C mode: Under this mode, a pair of vortices has the same direction of rotation.

Mode	Sketch
2S	
2P	
P+S	
2P$_O$	
2P+2S	
2T	
2C	

Figure 2.6: Mode of vortex shedding according to Jauvtis and Williamson (2004) and Khalak and Williamson (1999)

2.2.3 Vortex induced vibration

When fluid passes through a bluff structure, the separation of the fluid from the bluff body results in an unsteady wake, which causes the vortices to detach alternately from the top and bottom sides of the bluff body and produces periodic forces on the structure. In some cases, when the vortex shedding frequency approximates the natural frequency of the structure, these forces could produce a strong vibratory motion, which is known

as the VIV phenomenon. In VIV, a structure experiences the force in the streamwise (drag) and cross-flow directions (lift).

$$F_D = \frac{1}{2} C_D \rho D U^2 \qquad (2.1)$$

$$F_L = \frac{1}{2} C_{LD} \rho D U^2 \qquad (2.2)$$

where C_D and C_L are the drag and lift coefficients, ρ is the density, U is the velocity and D is the diameter of cylinder. These components of force occurred in periodic variation. The cross-flow vibration oscillates at the vortex shedding frequency while the in-line vibration oscillates at twice the shedding frequency.

The behaviour and severity of VIV depend on a number of important factors, including:

- Reynold number
- Mass ratio
- Damping ratio
- Reduced velocity

2.3 Dimensionless parameter

This section summarizes the number of non-dimensional terms used for the flow around both fixed and oscillating cylinders. These parameters are significant in analysing the flow around a fixed cylinder and the VIV phenomenon.

2.3.1 Reynolds number (Re)

The ratio of the inertial force to the viscous force within the fluid is known as the Re, which is given by;

$$Re = \frac{UD}{\upsilon} \qquad (2.3)$$

where U, D and υ represent the inlet velocity, characteristic length and kinematic viscosity, respectively. The nature of the flow depends on the Reynold regime (explained in section 2.2). For a low Re regime, viscous forces are dominant and characterized by smooth and constant fluid motion (laminar flow). By Contrast, for a high Re, inertial forces are dominant, and the flow is highly turbulent (turbulent flow).

2.3.2 Reduced velocity

Reduced velocity (U_r), which is mean velocity normalized by diameter of cylinder and natural frequency of structure, is an important parameter when the structure begins oscillation due to the VIV phenomenon. This parameter is defined by

$$U_r = \frac{U}{Df_n} \tag{2.4}$$

Where U, D and f_n are velocity of fluid, diameter of cylinder and natural frequency of structure, respectively. Maximum cylinder amplitude response observed within range of reduced velocity Ur=5-7.

2.3.3 Strouhal number

The vortex-shedding frequency of a fixed cylinder is defined by a non-dimensional quantity known as the Strouhal number (St).

$$St = \frac{f_v D}{U} \tag{2.5}$$

where f_v , D and U represent vortex-shedding frequency, diameter of a cylinder and current velocity of the fluid. In the current study, Fast Fourier Transform (FFT) algorithm has been utilized to determine the Strouhal number.

Figure 2.7 shows the variation in Strouhal number at different Re ranges. The Strouhal number is nearly constant (i.e. St=0.2) in the subcritical range. The Strouhal

number suddenly increased in the transition and supercritical regimes. According to Sumer and Fredsøe (1997), the sudden increase in Strouhal number is due to the turbulent nature of the boundary layer on both sides of the cylinder, resulting in a delay in the boundary layer separation. In view of such delay, the vortices (in the wake region) become closer to each other and interact more quickly, resulting in higher Strouhal number values.
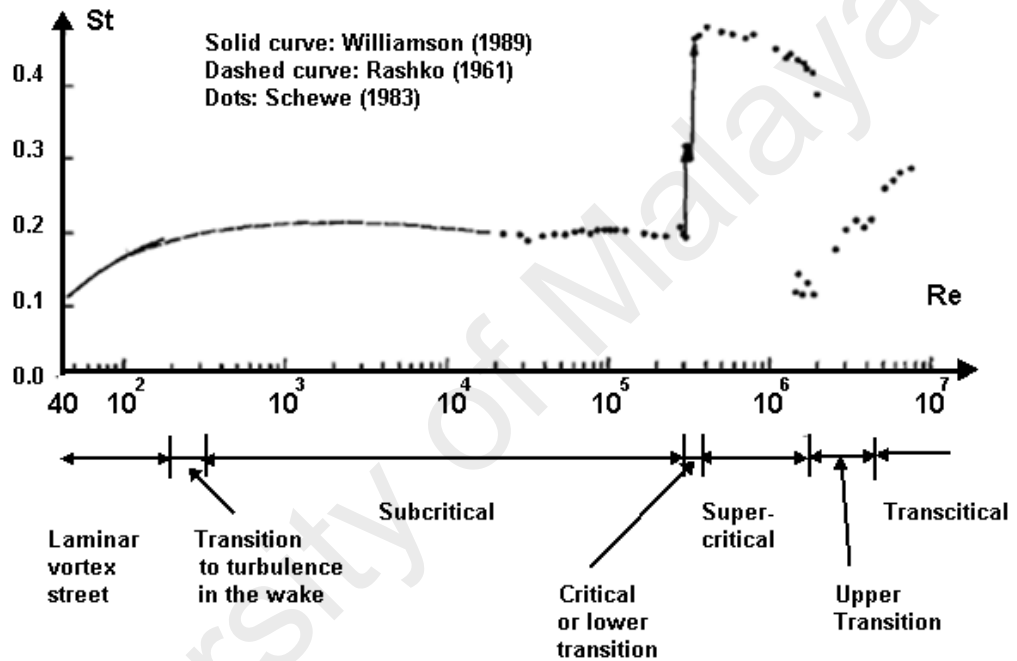
Figure 2.7: Strouhal number at different Reynold number regime (Sumer & Fredsøe, 1997)

2.3.4 Damping ratio

Damping ratio is defined as ratio of actual damping to the critical damping value and is given by:

$$\zeta = \frac{c}{2m\omega_n} \tag{2.6}$$

Where c, m and ω_n are damping coefficient constant, mass of cylinder and natural frequency, respectively.

2.3.5 Mass ratio

The mass ratio, which is defined as the ratio of the mass of the vibrating cylinder (m_{osc}) to the mass of the fluid displaced *(m_f)*, is given by

$$m^* = \frac{m_{osc}}{m_f} \tag{2.7}$$

And $m_f = \frac{1}{4}\rho\pi D^2 L$

where ρ, D and L is the density of fluid, the diameter of the cylinder and the submerged length of the cylinder, respectively.

The mass ratio significantly affects the VIV. During oscillation, a higher mass ratio (m^*=100-1000) corresponds to a lower amplitude response (Feng, 1968), and lower mass ratio corresponds to a higher amplitude response of the cylinder (Khalak & Williamson, 1999) as shown in Figure 2.8. A high mass ratio resulted in only two branches, namely, initial and lower branches, whereas a low mass ratio resulted in three branches, namely, initial, upper and lower branches (Figure 2.8).
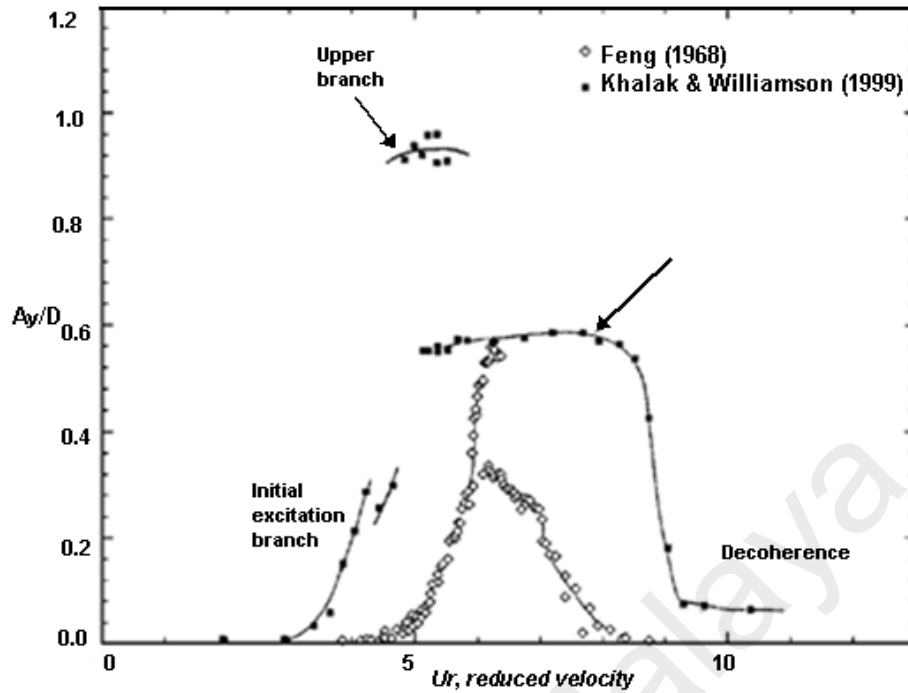
Figure 2.8: Cylinder amplitude response for low mass ratio (Khalak & Williamson, 1999) and high mass ratio (Feng, 1968)

2.3.6 Roughness ratio

The smoothness of the surface is defined by the roughness ratio,

$$\frac{k}{d} \tag{2.8}$$

where k is the characteristic surface roughness of the body, and 'd' is diameter of structure. The roughness of the structure affects the boundary layer separation and the occurrence of VIV. Achenbach and Heinecke (1981) experimentally showed in the trans-critical range that smooth surface cylinders have a high frequency wake and Strouhal number (St=0.5), whereas rough surface cylinders have an organized periodic wake with a low Strouhal number (0.25). In the trans-critical regime, VIV generally occurs at St=0.2 rather than at higher values (St=0.25) [Figure 2.9].
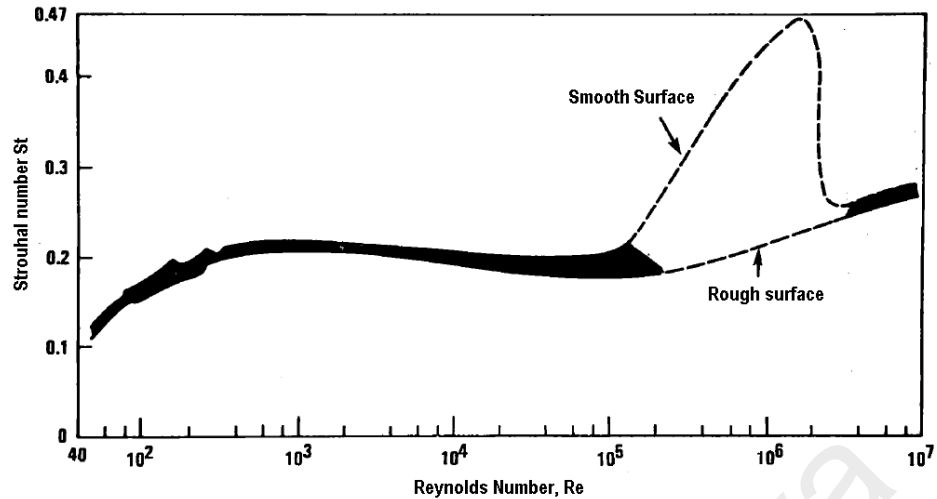
Figure 2.9: Relationship between Strouhal number and Reynolds number for smooth and rough surface cylinder (Achenbach & Heinecke, 1981)

2.3.7 Y+ Value

The flow around a cylinder results in an adverse pressure gradient. As such, the near wall region must be investigated. A Y+ value less than or equal to unity must be maintained so that the near wall region would be resolved adequately. The Y+ values can be calculated as follows:

$$y^+ = \frac{\rho u_t y_p}{\mu} \tag{2.9}$$

where y_p is the distance between the cylinder wall and the nearest node on the cylinder wall, ρ is the density of the fluid, μ is the viscosity of the fluid and u_t is the friction velocity.

2.4 Lock-in

The lock-in region is defined as the range of the reduced velocity at which the natural frequency of the cylinder is equal or approximate to the vortex shedding frequency (i.e. $f_n/f_v=1.0$), resulting in a resonance phenomenon, as shown in Figure 2.10. A lock-in phenomenon is found in the range of Ur=5-7. In the lock-in

region, the strength of the vortices is increased (Griffin & Ramberg, 1975), as well as the drag on the cylinder . When the cylinder vibration reached near the vortex shedding, an abrupt change to 180° is observed in the phase shift between the cylinder oscillation and the vortex shedding (Ongoren & Rockwell, 1988; Stansby, 1976).
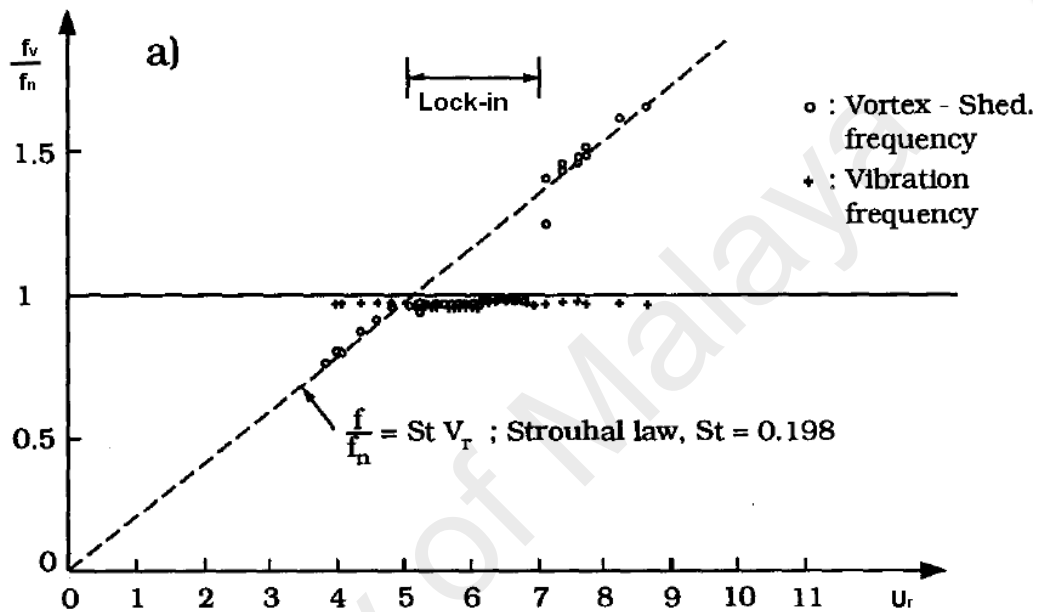
Figure 2.10: Frequency ratio versus reduced velocity (Feng, 1968), taken from Sumer and Fredsøe (1997)

2.5 Body shape

The behaviour of the flow passing through the structures highly depended on the shape of the structure. The shapes of the cylinder are categorized into two types: streamline and non-streamline shapes (which are also knows as bluff bodies). The flow around bluff bodies is of significant research interest because of its complex flow. In bluff bodies, the fluid separated from the structure after flowing over a substantial part of its surface. The location of the separation point determined the behaviour and characteristics of the wake region (i.e. whether laminar, partially turbulent or fully turbulent). Examples of bluff bodies included circular cylinder, pipe, eclipse, and so on.

2.6 Flow around fixed cylinder

Flow around fixed cylinders provides a basis for studying the VIV occurring in cylinders that are free to oscillate in the cross-flow direction. After the catastrophic failure of the Tacoma Narrow Bridge, aero elastic instabilities drew the attention of researchers. The research areas included galloping, vortex shedding and the divergence of circular cylinder, which were investigated using experimental, numerical and analytical methods. From the 1960s up to the 1990s, the flow around a fixed cylinder is investigated numerically at a low Re (Braza, Chassaing, & Minh, 1986; Dennis, 1973; Fornberg, 1985; Nieuwstadt & Keller, 1973; Takami & Keller, 1969). After the 1990s, the advancements of computational technology enabled researchers to utilize numerical approaches at a relatively high Re with different techniques, such as discrete volume method, Lattice-Boltzmann, and finite element method (He & Doolen, 1997; Henderson, 1995; Meneghini & Bearman, 1995; Mittal, Kumar, & Raghuvanshi, 1997).

With the exponential advancement in computer technology in the past decade, the trend towards computational analysis has markedly increased. The reliability and accuracy of computational analysis depend on temporal, spatial and equation discretization. The complex nature of the flow around a cylinder makes it an excellent case for assessing the ability of computational packages and extending the study to real environmental flow conditions. In addition, the flow around a cylinder is an ideal test case for testing CFD codes, as well as a good starting point for analysing more complex flows. In view of this unpredictable and complex physics, the flow around circular cylinders is sensitive in terms of flow separation, boundary layer, wake region characteristics, drag coefficient and Strouhal number.

According to Bloor (1964), the wake varies in the span-wise direction at Re>300, and a 3D analysis is necessary to capture the wake turbulence characteristics. The flow

around cylinders has been extensively studied by researchers for several decades ((Jauvtis & Williamson, 2004; Kiu, Stappenbelt, & Thiagarajan, 2011; Lu, Dalton, & Zhang, 1997; Morkovin, 1964; Niemann & Hölscher, 1990; Norberg, 1987; Williamson, 1996; Williamson & Govardhan, 2008; Wu, Ge, & Hong, 2012)). The following sections present the literature review of the experimental and numerical studies on the flow around fixed cylinders.

2.6.1 Experimental work

Previous experimental works on the flow around cylinder were conducted by Dryden and Hill (1930), Achenbach (1968), Roshko (1961), Linke (1931), Thom (1929), Schewe (1983), Bearman and Zdravkovich (1978), Cantwell and Coles (1983), Norberg (1987) and Norberg (1994). Townsend (1949), Bouard and Coutanceau (1980) and Yamada et al. (1980) beyond the ten diameter behind the cylinder. Lourenco and Shih (1993) considered up to 10 dimeters behind the cylinder. Lourenco and Shih (1993) performed an experimental study using particle image velocimetry (PIV) technique to investigate the velocity profile in the wake region up to three diameters behind the cylinder. Ong and Wallace (1996) investigated the velocity profile from $3D_o$ up to $10D_o$ in the wake region behind the cylinder by using a hot-wire probe to measure and validate the accuracy of the X-array data. The inaccuracy is experimentally analysed using single sensor hot-wire probes. The authors also validated the use of X-array data with four-sensor hot-wire probes.   Dong et al (2006) performed PIV experimental measurements and direct numerical simulations (DNS) to analyse the effect of Re on the wake statistics and shear instability at Re=3900 and 10000. A shorter recirculation length is observed at a higher Re. The authors observed significant variations in the flow statistics with changing Re. Williamson (1989) studied the relationship between the Strouhal and Reynold numbers as well as the oblique vortex shedding. The author concluded that these fundamental characteristics are directly influenced because the end

surface conditions and discontinuities in the St–Re curve are due to the transition from one mode to another oblique shedding mode. Further investigation showed that the vortex wake is affected by the end conditions of the cylinders of even 100D in length. Norberg (1987) focused on the combined effect of the low-intensity free stream turbulence and the Re on the Strouhal number and the root mean square pressure coefficient. The authors observed that the insensitivity varied with the turbulence intensity for Re<1000. At a high Re, altering the turbulence intensity significantly affected the results, particularly the pressure forces. In another experimental study, Norberg (1994) focused on the effect of aspect ratio on the Strouhal number and the mean base suction coefficient measured at the mid-span position. The investigation is conducted in the Re range 50 to 40000. The author concluded that the aspect ratio size (L/D_o) ranged from 60 to 70 for the solution independent of this parameter. Townsend (1949) extended the wake study beyond 10D to study the wake characteristics in a fully developed region. Yamada et al. (1980) experimentally studied the mean velocities, Reynolds shear stress, velocity diffusion and dissipation far away from the cylinder (i.e. $x/D = 30.5$ to 475 region). Lin et al. (1995) used particle image velocimetry in the range of Re=1000–10,000. They investigated the shear layer structure and the vortex formation length by using instantaneous, phase, and time averaged velocity as well as the vorticity field. Noca et al (1998) investigated the effect of the aspect ratio on the vortex formation length by using PIV. Parnaudeau (2008) numerically and experimentally studied the flow over cylinder at Re=3900 by using hot-wire anemometry and PIV technique. They investigated the wake region statistic up to 10 diameters behind the cylinder. Numerical simulation was performed using high-order scheme and immersed boundary method to investigate the turbulence statistics and power spectra in the wake region.

2.6.2 Numerical work

As discussed, rather than the selected CFD method, the simplification and assumptions made with respect to physical or turbulence modelling are the sensitive parameters affecting the accuracy of the numerical simulations. The available computing power is the main factor considered in choosing the numerical method for solving the fluid flow problem. Gordon Moore quantified the rate of significant improvement in computational power in 1965. At present, the available computational power remains insufficient for computing more complex simulations, and several techniques have been developed for CFD to efficiently resolve the complex fluid flow problem. The rate of improvement in computational technologies is significant but is still not improving as predicted by Moore (Figure 2.11).

Three numerical models are primarily used to solve the turbulent properties of the flow around cylinders. These models are direct numerical simulation (DNS), Reynolds-averaged Numerical simulation (RANS) model, and large eddy simulation (LES) model. Each of these models differs in terms of solving the Navier-Stokes equation and presenting the effects of the flow. DNS is the only numerical method in which all spatial and temporal scales of turbulence are resolved in case of flow around a cylinder.
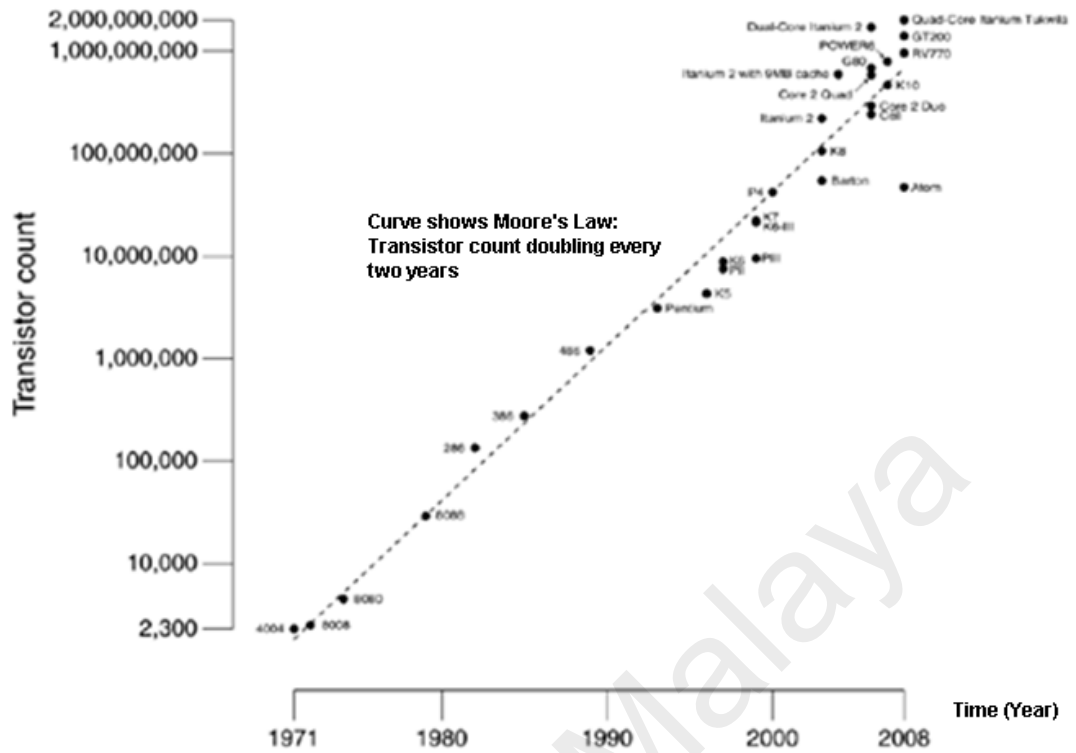
Figure 2.11: Increase in computational power with time (Starr, 2012)

2.6.2.1 Flow around cylinder using DNS Model:

Computational cost is the major obstacle in using DNS method even for low Re and a simple geometry. Blackburn et al (2001)   performed $2D_o$ and $3D_o$ numerical analyses using DNS at Re=1250 and compared the result with the experimental results. In addition, the authors discussed the restrictions and limitations of using DNS for high Re values. Dong and Karniadakis (2005) extended the use of DNS for flows around stationary and oscillating cylinders at Re=10^4. The simulation was performed by using an efficient multi-layer type parallel algorithm within the spectral element framework to determine the computational cost.

Ma et al (2000) investigated the mean flow characteristics and energy spectra up to $10D_o$ by using the DNS and LES models over the Re range of 500–5000. The wake region, which is close to the cylinder, is sensitive to a slight disturbance and the aspect

ratio of the cylinder. By contrast, at the far wake region (after $1D_o$), the flow depended on the vortex shedding dynamics. Dong et al. (2006) performed experimental and numerical simulations using PIV and DNS, respectively, to investigate the wake region behind the cylinder at Re=3900 and 10 000. The main objective of this study was to investigate the instability in the shear layer, which is altered significantly by changes in the Re. Wissink and Rodi (2008) and Wissink and Rodi (2008) performed a series of simulations with DNS at Re=3300 and compared the results with the experimental results obtained at Re=3900. They observed the roll-up of the separating shear layer, which transitioned to turbulence. In addition, the authors observed a reduction of performance as the number of processors increased by a factor of five. The simulation computed two laminar shear layers in the downstream cylinder, which resulted in separate boundary layers on the upper and lower surfaces of the cylinder. The roll-up behaviour is observed at the lower side of the cylinder, causing the transition from laminar to turbulence. The alternating rolling-up behaviour in the upper and lower shear layers resulted in a von Karman Vortex Street. Nevertheless, DNS, which can provide accurate and reliable results, is highly expensive even at a low Re.

Deng et al. (2014) demonstrated that the URANS model failed to predict the transitional flow characteristics. The authors observed that the failure of the k-ε model is due to the unrealistic estimation of the eddy viscosity in the stagnation region. The boundary layer and the separation region are not accurately predicted. Rajani et al. (2012) comprehensively studied the limitation of URANS in computing drag forces, mean pressure coefficients and skin friction coefficients at a moderate to a high Re. The authors used 2D URANS equations to test the capabilities in predicting the Strouhal number and hydrodynamic coefficients over the Re range of 10^4–10^7. The turbulent model results are reasonable up to Re=10^5 and produced good flow patterns. The angle of separation is over-predicted at the critical Re. DNS, which can provide accurate and

reliable results, is highly expensive even at a low Re. Computational cost is the main obstacle in applying DNS for moderate and high Reynolds numbers. In view of the deficiency of the URANS approach and the high computational cost of DNS, the flow around a cylinder in a subcritical regime is mostly investigated by using LES without a model, a fixed coefficient Smagorinsky model, or a dynamic model.

2.6.2.2 Flow around cylinder using LES Model

The flow around cylinder in the subcritical regime (Re=300 to 200k) is of particular interest because of its complex flow in terms of the transition to turbulent flow in the shear layers, the non-fixed separation angle and variation in the size of the recirculation length. The availability of large-scale experimental and numerical data for the flow around cylinders at Re=3900 makes it an excellent benchmark case for assessing the capability of computational tools and process. The flow around cylinders at Re=3900 appeared at the lower subcritical regime, at which the flow is laminar at the boundary layer and the transition in thin shear layers occurred in the wake behind the cylinder. Thus, a better strategy would be to test the turbulent model capability, mesh resolution, and computational tool at Re=3900, and then compare the result with the available results. Beaudan and Moin (1994) were the first to numerically test the flow around cylinders at Re=3900 by using large eddy simulation without a model, with a fixed-coefficient Smagorinsky model, and with a dynamic model. The authors used sixth order centred difference schemes to discretize viscous terms and fifth order upwind scheme for convective terms to solve the filtered Navier-Stokes equations. The authors observed significant differences in the results, particularly in the recirculation zone (i.e. up to 4D). He concluded that the dynamic (Germano, Piomelli, Moin, & Cabot, 1990) SGS model is better than the fixed coefficient SGS model in predicting the Reynold stresses in the wake region. Away from the recirculation zone, the authors observed no

significant difference in mean velocties, spanwise or shear Reynolds shear stress in all cases. In addition, the grid resolution significantly affected the solution of the flow around the cylinder. The results are compared with the experimental work of Lourenco and Shih (1993), and discrepancies are observed in the computations of the recirculation length.

The effects of structured and unstructured grids were studied by Fröhlich et al. (1998) at Re=3900 and 140000 by using LES with a specialized code. The author found that the unstructured LES code is operational, and that the costs for both structured and unstructured codes are the same because a lower number of grid points are used in the unstructured code. Breuer (1998a) investigated the numerical and modelling aspects of turbulent flow passing through a circular cylinder (Re=3900) by using LES. Two different subgrid models, namely, Smagorinsky and dynamic models, are used in the analysis. The author concluded that the dynamic model combined with central differencing produced more accurate results. Moreover, Breuer emphasized the role of span-wise resolution in using LES for the flow problem. Ma et al. (2000) investigated the wake dynamic up to 10D behind the cylinder at Re=500–5000 by using LES and DNS. The authors observed an uncertainty in the vortex formation length, which varies with the changing spanwise length. In addition, a U-shaped mean velocity profile is observed when the spanwise length of the working domain is πD_o whereas a V-shaped mean velocity profile is observed when the spanwise length is $2\pi D_o$. In contrast to the finding of Ma et al. (2000), Beaudan and Moin (1994) found that the spanwise length does not significantly influence the vortex formation length and shape of the mean velocity profile. Mittal and Moin (1997) used 2nd order central difference scheme for spatial discretization in the case study of the flow around a cylinder at Re=3900. The author investigated the numerical diffusion impact on the flow field in the range of 7D to 10D behind the cylinder wake. Their results indicated that the 2nd order central

difference scheme produces comparable results to those computed using higher-order upwind scheme, which is computationally expensive. The comparison is made with 30% smaller grid spacing in the case of the 2nd order central difference scheme. The drawback of the 2nd order central difference scheme is its sensitivity towards the grid and boundary condition of the outflow, suggesting that these variables should be defined clearly. In contrast to Lourenco and Shih (1993), the U-shape mean velocity profile is also validated by Kravchenko and Moin (2000). Tremblay, Manhart, and Friedrich (2002) performed LES using Cartesian grid technique and investigated the influence of subgrid-scale model and grid resolution. This study failed to accurately predict the recirculation length and the mean velocity profiles. Franke and Frank (2002) carried out a flow around a cylinder at Re=3900 with LES using cell-centred finite volume code. The authors concluded that short-term time averaging results in smaller values of recirculation length and an unconverged solution of the mean flow field. The authors also investigated the modelled SGS stresses and the computed Reynold stresses.

Afgan, Kahil, Benhamadouche, and Sagaut (2011) used dynamic Smagorinsky LES to numerically study the flow around cylinder at Re=3900 for a single and two side-by-side cylinders. The authors investigated the impact of grid-refinement, the size of the spanwise direction, the convection scheme, and the sub-grid scale model on the sensitivity of the simulation. One of the conclusions of the study is that the spanwise length exerted no impact beyond the 4D length. Furthermore, the recirculation length calculation is influenced by the use of a sub-grid scale model. Blockage ratios of 5% (for single cylinders) and 9.3% are used in this study, which are assumed acceptable as suggested by Norberg (1994).

Kravchenko and Moin (2000) mainly focused on grid resolution on the shear layer transition. The authors observed that an insufficient grid resolution may result in an

early transition in the shear layers, leading to inaccurate results. They found that a higher-order numerical method based on B-splines produces better results than those by finite difference simulations in the wake region behind the cylinder. Zhang et.al (2015) discussed the difference between finite and infinite circular cylinders on the flow mechanics. The authors concluded that a finite cylinder with a free end significantly affects the wake region. Wissink and Rodi (2008) performed series of simulations with DNS at Re=3300 and compared the results with those experimentally obtained at Re=3900. Lysenko, Ertesvåg, and Rian (2012) used the OPENFOAM tool to study the flow along a cylinder by using LES with a dynamic k-equation SGS model. Lysenko, Ertesvåg, and Rian (2014) also studied the flow around a cylinder at Re=20000 by using LES with a blended central-difference scheme. Jordan (2002) investigated the shear layer instability of the flow around a fixed cylinder at Re=8000 by using LES code. Analyses were performed using upwind finite difference scheme and SGS model. The calculations agreed well with the experimental results of Norberg (2003) except for the lower value of the lift coefficient.

2.6.2.3 Non-dimensional timestep and averaging time-statistic impact on results

As discussed earlier, in the flow around a cylinder case, the geometry of a cylinder is simple in shape but the flow behaviour is complex and unpredictable in terms of recirculation length, separation angle and statistics in the wake region. Recirculation length was found to be the most sensitive parameter in assessing the quality and convergence of the results. In addition to other parameters, non-dimensional time step and time-average statistics significantly affected the length of recirculation, separation angle and other statistical quantities.

Breuer (1998a) studied different numerical and modelling aspects for the flow past a cylinder at 3900 Reynolds number (Re) using the LES code. The author recorded most

of the statistical data for 100 D/U time units or 22 vortex shedding cycles, but also emphasised the importance of recording data for a long period of time. Breuer (1998a) computed the recirculation length value ranging from 1.0 to 1.1 with a Smagorinsky model and the high value of recirculation length ranging from 1.1 to 1.4 with a dynamic model having the same number of vortex shedding cycle data. The author also concluded that the near-wall and subgrid-scale (SGS) models play significant roles in the modelling side. The results of Rodi et al.(1997) and Breuer (1998a) showed that Strouhal number is not a very sensitive parameter and the accurate calculation of Strouhal number does not necessarily ensure good quality results. Breuer (1998a) likewise concluded that central schemes of second- or fourth-order accuracy lead to better results, whereas the upwind scheme cannot be recommended. Fröhlich et al. (1998) performed an LES study using structured and unstructured tetrahedral grids with a central differencing scheme to solve incompressible equations at Re=3900 and Re=140,000. The study reported a short recirculation length computed after 20 vortex shedding cycles using a finite element code with unstructured grid. Beaudan and Moin (1994) simulated the flow past a cylinder without a model, with a fixed-coefficient Smagorinsky model and a dynamic model and observed significant differences in the results, particularly in the recirculation zone (i.e. up to 4D). They concluded that the dynamic SGS model performs better in predicting the mean velocities and Reynold stresses than the calculation without a model. The authors observed no significant difference in mean velocities, spanwise or shear Reynolds shear stress in all the cases away from the recirculation zone. In addition, it was observed that grid resolution has significant effects on the solution of the flow around cylinder. Zdravkovich (1997) mentioned that the recirculation length will be shortened with the increase of Re in the sub-critical regime. Franke and Frank (2002) performed a series of LES at Re=3900 with cell-centred volume code. The study concluded that short-time averaging data

(with 10–21 vortex shedding cycles) result in short recirculation length. Increase in time averaging up to 42 averaging cycles results in high values of recirculation length and base pressure. However, the authors observed that the study is not enough to reach a statistically converged solution. Kravchenko and Moin (2000) studied the flow around a cylinder at Re=3900 using LES with a high-order accurate numerical model based on B-splines. They concluded that poor mesh resolution in the shear layer results in short recirculation length and vice versa.

Shao and Zhang (2006) compared the performance of Reynolds-averaged Navier–Stokes (RANS) and LES at Re=5800 (same sub-critical regime). Second-order upwind scheme (UDS) and bounded central differencing schemes were applied for the momentum equations. For pressure–velocity coupling, SIMPLE algorithm was employed. Shao and Zhang (2006) took time-average statistics for flow and turbulence quantities over 15 vortex shedding cycles. Young and Ooi (2007) performed a numerical simulation for the flow around a cylinder at Re=3900 using LES with the Smagorinsky SGS model. To ensure that the flow is free from initial conditions and fully developed, the simulation was executed for 60 non-dimensional time steps before the time statistical data were recorded. The results were recorded for 30 vortex shedding cycles. Parnaudeau et al. (2008) performed a flow over a circular cylinder using LES with high-order scheme. Power spectra and turbulence statistics up to 10D were investigated in the numerical study. The authors concluded that accuracy in predicting the recirculation length is the deciding factor on the agreement between numerical and experimental results. To diminish the effect of initial conditions, the authors ran the simulation for 30 vortex shedding cycles before recording the time statistic data. Uncertainty in the value of the recirculation length computed over different time statistics, i.e. for 12 and 52 shedding cycles, was observed. Moreover, the results for 52 vortex shedding cycles were less satisfactory compared with those of the 12 shedding

cycles. The reason behind the less than satisfactory results for high vortex shedding cycles should be investigated. Mani et al (2009) computed the flow over a cylinder at Re=3900 using LES code. The time advancement scheme used was second-order implicit near the cylinder surface and third-order Runge–Kutta in the far region. The simulations were carried out for 60 vortex shedding cycles. Rajani et al. (2016) performed a flow around a circular cylinder using LES with Smagorinsky and dynamic SGS models. Rajani et al. (2016) obtained time-average flow quantities over 20 vortex shedding cycles but observed no changes because of the doubled time sample size. Zhang et al. (2015) investigated the difference in the mechanisms of flow past finite and infinite cylinders at Re=3900 using LES code. They observed a reduction in the values of the mean drag coefficient and lift fluctuation of finite circular cylinder. The free-shear layer shedding was also stable in the finite cylinder case. The impact of time-average statistic needs to be addressed because of the wide range of variations observed in the results taken at different time averages.

A number of researchers (Bin, LUO, PENG, & WU, 2013; M. C. Ong, Utnes, Holmedal, Myrhaug, & Pettersen, 2009; Qun, Chen, & Zheng, 2016; Tao, 2015; Wood, De Nayer, Schmidt, & Breuer, 2016) recently studied the flow around a cylinder and tested a LES model. They proved that the model is a reliable choice for assessing different parameters of flow around a cylinder.

2.7 Flow around cylinder free to oscillate in cross flow direction (VIV phenomenon)

In this section, previous research relating to flow around a cylinder, which is free to oscillate in the cross-flow direction, is discussed in detail. The dynamics of the cylinder is completely different from those of the fixed cylinder because of the interaction between the solid structure and the flowing fluid. Vortex-induced vibration (VIV)

phenomenon, which is associated with a cylinder that is free to oscillate, is inherently a self-exciting, self-regulating and highly nonlinear behaviour. This phenomenon accelerates the cross-flow excitation of the structures (may be resonance behaviour), which ultimately results in large amplitude and vortex shedding frequency lock-in with natural frequency. Despite the wide range of applications of VIV phenomenon, the physical mechanism responsible for it was identified only in the mid-20th century. Feng (1968) performed an experimental study to measure the fluid forces and amplitude of a cylinder, which is free to move in the cross-flow direction. Sainsbury and King (1971) and Wootton et al. (1972) investigated the problem caused by VIV in a large offshore oil platform at Immingham, England.

Large number of fundamental research have been performed to investigate the VIV phenomenon because of its wide range of applications (Bearman, 2011; Blackburn et al., 2001; Gabbai & Benaroya, 2005; Jauvtis & Williamson, 2004; Khalak & Williamson, 1999; Sarpkaya, 1979, 2004; Sumer & Fredsøe, 2006; Sumner, 2010). These studies include free vibration and forced vibration of cylinder with single and multiple degrees of freedom. In both approaches, a number of parameters (Re, mass-damping ratio, type of oscillation, vortex shape and frequency ratio) are involved in affecting the behaviour of the VIV phenomenon, as explained in Section 2.3. As discussed earlier, when the vortex shedding frequency is equal to or close to the natural frequency of the cylinder, large resonant amplitude that is considered the 'lock-in' region is obtained. In the case of long slender structures, like hull, risers and mooring lines, the problems linked with VIV become more complex due to the association of sheared flow. This phenomenon is complicated due to the fact that resonant responses occur at different axial locations and different modes. The VIV phenomenon was investigated by Vandiver (1983) and Vandiver et al. (1996)   , who concluded that fluctuation in flow is the factor behind mode switching. Lie et al. (1997) observed that

VIV frequency remains constant and that a sudden shift occurs in the second to third lock-in modes. A temporary mode transition was observed by Chaplin et al. (2005) in uniform flow. In these cases, the spectrum of the response showed a peak at shedding frequency with broad bandwidth Kim et al. (1986)   . Recently, a comprehensive review on the behaviour of a long slender structure facing VIV was presented by Wu et al. (2012).

Numerical investigation on the VIV phenomenon for design structure is an important step, but a direct simulation at high Re for complex geometry is still not possible mainly because of the high computational cost. Proper simplification and assumptions in the modelling of VIV problems may produce results that can assist in the real design. In the case of flow around an elastically mounted rigid cylinder, two types of responses are observed, as explained by Khalak and Williamson (1997b) i.e. small amplitude with two branches and large amplitude with three branches (Figure 2.8). According to the authors, a high amplitude is observed for the low mass damping ratio, with the three branches termed as the 'initial', 'lower' and 'upper' branches. A small amplitude with two branches is observed at high mass damping ratio, with the two branches termed as the 'initial' and 'lower' branches. A low amplitude with two branches was observed in Feng (1968), in which air was used as the working fluid. In the study of Khalak and Williamson (1997b), water with extremely low damping ratio (low mass damping ratio) was used as the working fluid, and a high amplitude equal to 1D of the cylinder was observed in the experimental study. Moreover, a wide response range was observed with low mass damping ratio. This behaviour was also noted by Griffin and Ramberg (1975) in small mass system.

Wake behind an oscillating structure is investigated by a number of researchers in the literature, but most of the early research is limited to a small amplitude with two

branch modes.   Griffin et al. (1973) and Griffin (1972) computed the phase angle, lift coefficient, energy transfer and mean velocity fluctuation behind a cylinder. Smoke visualisation approach was used by Brika and Laneville (1993) to observe the wake structure of a small amplitude with initial and low branches.   Govardhan and Williamson (2000) and Khalak and Williamson (1999) investigated the flow structure in the wake of high-amplitude and small-amplitude cases. The authors also measured the fluid forces on cylinder, non-dimensional amplitude and other coefficients for the range of reduced velocity, that is, Ur=2–14. Two single vortex shedding cycles were observed at the initial branch and two pairs of vortex shedding cycles at the upper and lower branches. The 2D RANS code was utilised by Placzek et al (2009) to study VIV at a low mass ratio and low Re=100. The mode of vortex shedding was efficiently captured by the 2D RANS code at Re=100. Zhao et al. (2014) analysed the VIV phenomenon with a range of Re=150 to 1000 using 3D Navier–Stokes (NS) equations. The authors concluded that 2D NS equations are inappropriate for analysing VIV behaviour in a turbulent regime, whereas the 2D RANS equation performs well in this aspect. In addition, the authors concluded that the three-dimensionality of the flow is significant in the upper branch and is weakest in the initial branch of the VIV response. Islam et al. (2016) numerically studied the factors responsible for reduction in the vortex shedding and corresponding drag forces at Re=80 to 200 for flow around a square cylinder. Islam et al. (2012) used the incompressible Boltzmann method to analyse the impact of aspect ratio of rectangular cylinder on vortex mode, fluid forces and vortex shedding frequency at Re=100 to 250. Behara and Sotiropoulos (2016) investigated the dynamic and wake modes of a sphere under VIV at Re=300 to 100 at a low mass ratio. The study was conducted for reduced velocity (U_r) ranging from 0 to 13. The authors concluded that the wake modes and trajectories of the sphere strongly depend on Re. Liangjie et al. (2014) investigated VIV at different Re values with the same shear flow parameter and

discovered that the multimodal phenomenon is significant at high Re. The dominant vibration mode was observed at the maximum order mode of natural frequency. Dong et al. (2006) and Dong and Karniadakis (2005) studied the flow for oscillating and fixed cylinders at Re=10^4 by using the 3D direct numerical simulation (DNS) code. The author utilised multi-level parallel algorithm to accomplish the simulation using a Compaq Alpha cluster with up to 1536 processors. Hydrodynamic coefficients, Strouhal number and other flow quantities were very well captured. Various researchers have analysed VIV for a circular cylinder at low Re, i.e. Re < 10^3 (Benitz et al., 2016; D'Alessandro, Montelpare, & Ricci, 2016; Laroussi, Djebbi, & Moussa, 2014; Mimeau, Cottet, & Mortazavi, 2016; Singh & Chatterjee, 2014; Singha, Nagarajan, & Sinhamahapatra, 2016; Tu et al., 2015; Zhao, Cheng, Zhang, & Hu, 2016).

The study of Tutar and Holdø (2000) was based on an LES with 2D and 3D models at Re=24000. The comparison of the result of a pressure coefficient around a cylinder with that in the experimental work shows a notable difference. Dong et al. (2006) and Dong and Karniadakis (2005) studied the flow for oscillating and fixed cylinders at Re=24000 by using 3D DNS code. An experimental investigation of VIV for an elastically mounted cylinder performed by Khalak and Williamson (1996) for low mass ratio in the range of Re=1700 to 12,000 was numerically validated by Pan et al. (2007), Li et al. (2014) and Guilmineau and Queutey (2004). Despite the agreement in predicting vortex shedding mode and transition between different modes, the numerical studies still lag behind in computing the maximum amplitude. All these numerical simulations were performed on a 2D model using different RANS codes. In the last decade, considerable research has been done to completely understand the behaviour of flow past cylinder at high Re. A number of 3D numerical studies have been performed for flow around a cylinder (either fixed or free to oscillate) using different models, including DNS, LES and DES models (Colomés, Badia, & Principe, 2016; Hoffman,

Jansson, Jansson, & De Abreu, 2015; Khashehchi, Abdi, & Hooman, 2015; Kondo & Yamada, 1995; Y. Li, Chan, Mei, & Zhu, 2015; Mannini, Šoda, & Schewe, 2010; Pang, Skote, & Lim, 2016; Sohankar, 2006; Stringer, Zang, & Hillis, 2014; Trias, Gorobets, & Oliva, 2015). However, at high Re, VIV phenomenon for the flow past a cylinder is still unexplored and needs to be investigated.

2.8 Summary

Flow around cylinder is highly complex problem due to unpredictable flow behaviour is terms of recirculation length, angle of separation and flow dynamics in the wake region. Available studies revealed that URANS model is unable to provide details insight in flow around cylinder problem whereas DNS model is computationally expensive. LES model, in which advantages of both URANS and DNS model are combined, is better to predict the flow behaviour around fixed cylinder. Although the flow around cylinder at Re=3900 has been explored by numerous researchers, discrepancies still exists in the results, particularly in calculating the angle of separation, recirculation length, and statistics in the wake region behind the cylinder. The effect of spanwise length, spanwise grid, and near-field grid resolution on the wake region needs to be addressed. Moreover, the previous studies unable to present clear picture of impact of time interval averaging in obtaining fully converged mean flow field.

In case of VIV problem, previous studies are carried out using computationally expensive model. Furthermore, most of the studies are unable to capture three mode of vortex and maximum amplitude of cylinder, which are point of interest in many VIV problems. Also, most of the literature study is limited to low Reynolds number and fixed oscillation. The capability and accuracy of the RANS model, which is comparatively less expensive, in assessing the VIV of elastically mounted rigid cylinder at high Reynolds number need to be addressed. In addition, VIV of elastically mounted

rigid cylinder having very low mass-damping ratio need to be investigated using RANS

model and validated against the famous Khalak and Williamson (1996) experimental

results.

CHAPTER 3: COMPUTATIONAL FLUID DYNAMICS USING FLUENT

This chapter presents the computational fluid dynamics (CFD) background and the numerical techniques used to solve the problems related to fluid flow, heat transfer and chemical reaction etc. CFD covers a wide range of applications, ranging from electronic engineering, power plants and process industries, to building analysis, marine engineering, offshore structure analysis and ship design. The current study is related to flow around a cylinder, which is of practical application in marine risers, tall buildings and offshore structures. Unlike experimental testing, CFD simulations provide a more detailed insight into a problem. Moreover, it is possible to perform the CFD analysis of the case studies which is normally difficult to be executed experimentally due to hazards condition, high laboratory requirements, very lengthy process etc. CFD simulations present an excellent alternative solution to overcome the inherent limitation in the experimental approach. The CFD field is connected to the application of mathematical, numerical and computational techniques to fluid flow simulation. The main goal of CFD simulations is to validate the results obtained from experiments and avoid (at least partially) time-consuming, expensive and impractical experiments.

This chapter is divided into two sections. Section 1 summarises the governing equations used to describe the fluid flow and methodology adopted to solve the equations. It also explains the background and limitation of CFD techniques. Section 2 discusses different turbulence models which are applicable in the case of flow around a cylinder.

3.1 Background

Flow around a cylinder is one of the highly researched areas in fluid dynamics. Although the geometry of a cylinder is very simple, its flow has many unpredictable and complex features. The study on flow around a cylinder and VIV analysis has been

performed either by empirical tools, numerical simulations or experiments. Empirical tools depend on either experimental data for prediction and analysis of VIV phenomenon or on numerical simulation techniques in which viscous NS equations are numerically solved to compute hydrodynamic forces. With the advancement in computer technologies, the trend toward numerical simulation increased exponentially in the last decade, and additional research on VIV study shifted to CFD techniques. Although CFD analysis still has several limitations, like complex flow dynamics, high computational cost for 3D real problems, selection of proper turbulent model and different assumptions, currently, due to the continuous advancement in computational capabilities, the proper simplification of 3D problems to 2D problems and availability of comparatively less expensive turbulent tools have increased the reliability, accuracy and confidence of numerical simulation tools. Despite these advancements, CFD analysis still lags in modelling real-world complex scenarios and needs proper guidance and data from experimental testing. Reviews by Breuer (1998a), Sarpkaya (2004) and Bearman (2011) explained in detail the constraint and restriction while using numerical simulations, particularly at high Re values. LES, DNS and RANS are numerical techniques primarily used to solve turbulent properties of the flow around a cylinder. The hybrid of RANS and LES was also used previously by a number of researchers. DNS and LES are found to be good methodologies for assessing the deep insight of wake–boundary layer interaction, but they are computationally expensive and require high computing power. At high Re, the use of the DNS technique is impractical due to unrealistic high computational power demand.

3.2 Fluid flow equations

Claude Navier and George Stokes derived basic principle equations, commonly known as NS equations, for fluid flow in the 18th century. NS equations are mainly

derived from principle equations (continuity, momentum and energy equation) of fluid dynamics.

3.2.1 Continuity equation

Continuity equation is based on one of the fundamental principles known as 'law of conservation of mass'. In fluid flow, these governing equations are based on the fact that a change of mass in control volume is equal to the total mass entering the control volume minus the total mass leaving the control volume.

3.2.2 Momentum equation

According to Newton's second law of motion, momentum is defined in terms of pressure and viscous stresses acting on a fluid particle. According to this definition, the rate of change of momentum is based on the total force caused by surface stresses and body force in the resultant direction.

3.2.3 Energy equation

Energy equation is based on 1st law of thermodynamics which state that rate of change of energy of a fluid particle is equal to sum of rate of heat addition plus work done on that particle. These equations define the transport of heat energy and its effect.

3.2.4 Navier-Stokes (NS) equations

NS equations combine these fundamental principles in a set of partial differential equations (PDEs), which are solved to predict the pressure and velocity throughout the flow. Details on the derivation of NS equations are available in the literature (H. Versteeg & Malalasekera, 1995). Fluid flow, which is assumed to be incompressible, can be described as:

Momentum equations:

$$\frac{\partial u_i}{\partial t} + u_j \frac{\partial u_i}{\partial x_j} = -\frac{1}{\rho} \frac{\partial p}{\partial x_i} + v \frac{\partial^2 \overline{u}_i}{\partial x_j \partial x_j} \qquad (3.1)$$

Continuity equation:

$$\frac{\partial u_i}{\partial x_i} = 0 \qquad (3.2)$$

where u and υ are velocity in the in-line direction and kinematic viscosity of fluid, respectively, while *p* and ρ are the pressure and fluid density, respectively.

3.3 Methodology

The general work flow of the numerical analysis is comprised of geometry modelling, mesh generation, physical description of problem and result analysis Figure 3.1. This work flow can be divided numerically into three sections: pre-processing, solver and post-processing.
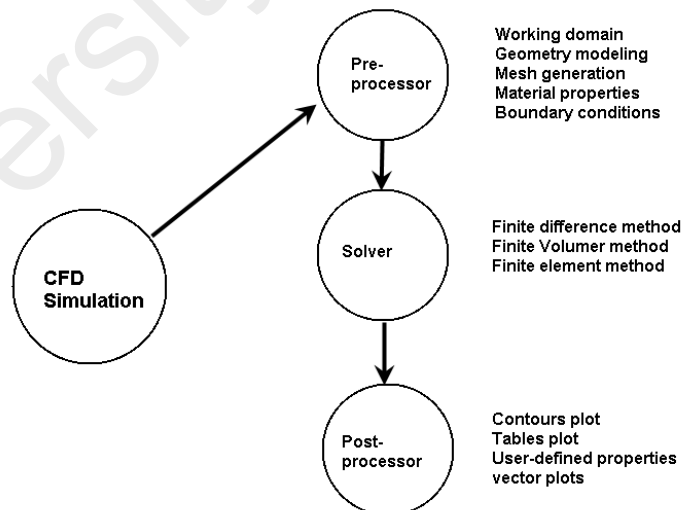
Figure 3.1: CFD methodology

3.3.1 Preprocessor

The task of pre-processing is to define the problem properly in a manner that is appropriate for a solver. The working environment surrounding the area of interest is known as the computational domain, which is divided into a finite number of elements referred to as mesh. After meshing the computational domain, boundary conditions or constraints and fluid properties are defined in the pre-processing section.

3.3.2 Solver

In this section, governing equations are solved with the pre-processing setup. The simulation is carried out iteratively to solve the flow parameters. The accuracy of the solution depends on the convergence of simulations.

3.3.3 Post-processing

This section visualises the results from the solver. In the ANSYS workbench, results can be analysed in the form of contour plots, vector plot or table. ANSYS 16.2 post-processing provides a detailed insight into the flow patterns, prediction and trending of flow behaviour.

3.4 Accuracy of numerical process and type of errors

Numerous types of errors are associated with CFD method which includes numerical errors, modelling errors, uncertainty in using application, users errors etc. Difference between exact and numerical equation is known as numerical errors. Numerical errors are further discretized into solution errors, spatial discretization error, temporal discretization error, round off error and solution error estimation. Numerical errors can be reduced by increasing the spatial grid density and reducing the timestep size. The empirical models used to describe the flow phenomenon results in modeling error. For turbulent flows, the requirement for using empirical model originates from the high computational cost in solving the exact equations with DNS method. These empirical

models work as a bridge between the real flow and statistically averaged equations. Insufficient expertise in use of CFD tool also result in user error.

Figure 3.2 schematically shows the numerical simulation process and errors associated with each step (Breuer, 1998a). Firstly, the physical model needs to be described and the mathematical model identified for the behaviour of the physical model. An error associated with the selection of a mathematical model is known as a 'modelling error', which is the difference between the actual physical model and the exact solution obtained from the mathematical model. Secondly, the complex physical models have no exact analytical solution, and thus the equations need to be discretised. The error associated with the discretisation of basic equations is known as 'discretisation error', which is the difference between the exact solution of the mathematical model and the discretised equations. In CFD analysis, discretisation errors can be handled by sufficiently choosing a fine resolution and proper discretisation method. The third type of error is known as 'convergence error', which is the difference between the iterative and exact solutions of discretised equations.
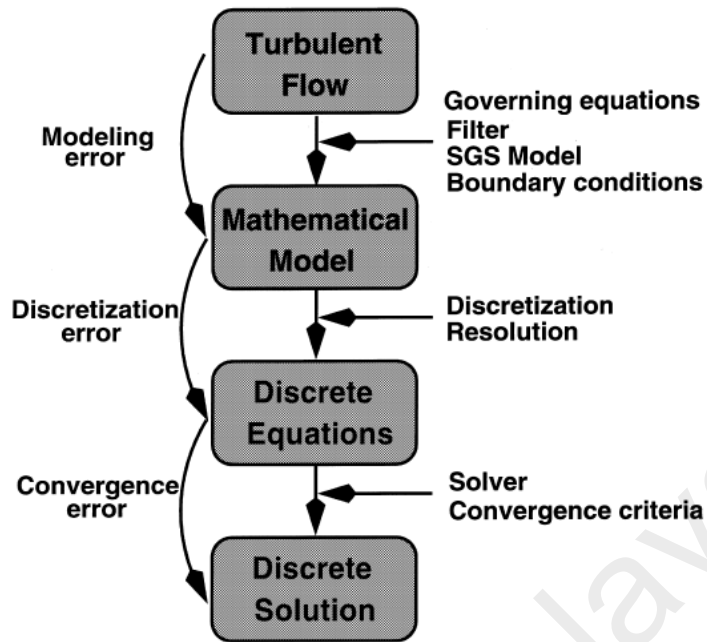
Figure 3.2: Numerical simulation procedure and type of errors (Breuer, 1998a)

3.5 Discretization

In the discretisation process, the continuous fluid flow is divided into discrete numerical data in such a manner that it can be understood and solved by the simulation tool.
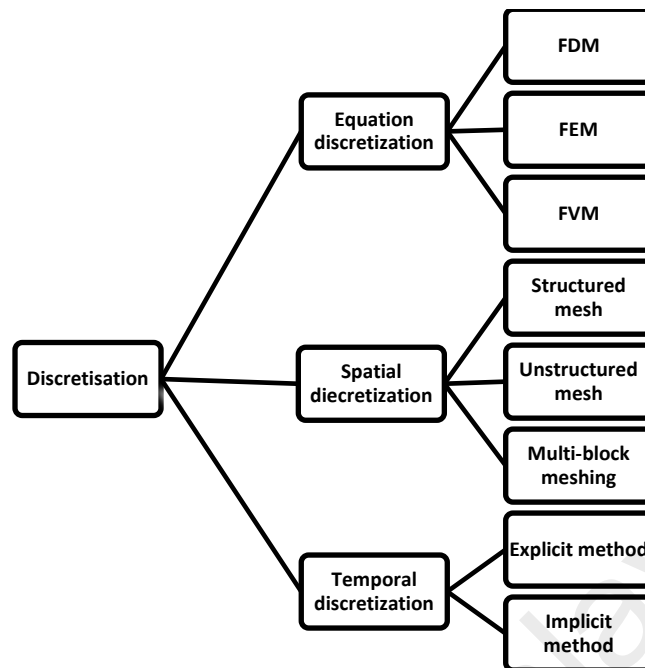
Figure 3.3: Discretization

To perform numerical simulations for flow around a structure, the complete domain around the structure should be discretised and divided into a number of points at which required variables (e.g. velocity, pressure, density) are computed. The governing PDEs are numerically solved by converting them into an algebraic expression. These approximate algebraic expressions are solved at discrete points near the domain of interests using finite element, finite difference or finite volume methods (FVMs). These methods use neighbouring points to calculate derivatives, and so there is the concept of a cluster of points in the flow field or domain under consideration, called as a mesh or grid. The process of representing the continuous domain into discretised points is called 'grid or mesh representation'. In general, the discretisation process can be divided into three categories: equation discretisation, spatial discretisation and temporal discretisation Figure 3.3.

3.5.1 Equation discretization

The conversion of PDE of fluid flow problems into a numerical analogue of the equation is called equation discretisation. The process of numerical discretisation is carried out using different techniques. Three major equation discretisation methods, namely, finite difference method (FDM), finite element method (FEM) and FVM, are discussed in the following section.

3.5.1.1 Finite difference method (FDM)

FDM is the simplest method that works perfectly for a simple geometry of structured and unstructured meshes. This method is based on the Taylor expansion (Stroud, 1990) concept for solving second-order PDEs. However, most CFD codes use FVM or FEM in the case of flow past bluff bodies.

3.5.1.2 Finite element method (FEM)

FEM is a good technique for arbitrary shapes in which the working domain is divided into finite elements. It mostly deals with unstructured mesh and is mostly used for structural analysis problems. Although FEM is very stable, it requires more memory compared with FVM.

3.5.1.3 Finite volume method (FVM)

FVM is the best numerical discretisation approach used in CFD problems. It can work with structured and unstructured grids with complex geometry. In FVM, the working domain is split into a finite number of sub-domains called control volume, and conservation equations are applied to each control volume.

3.5.2 Spatial discretization

Mesh or grid generation comes under spatial discretisation section. Mesh is defined as discrete points or locations in which variables are solved and computed. A grid divides the working domain into a number of finite domains. Three types of grids are mainly characterised based on their points of connectivity: structured, unstructured and multi-blocking meshes. Structured mesh has regular connectivity, and each discrete point has the same number of neighbour nodes. In the case of irregular mesh, the connectivity is irregular and the matrix needs to be defined for each cell. Structured mesh is acceptable in a simple fluid flow problem but results in a complex flow case. Unstructured mesh is recommended for use in the case of complex geometry. Since the arrangement of nodes is not in sequence due to which unstructured mesh is computationally expensive. In addition, greater numbers of elements are required for refinement, which also lead to high cost. Multi-blocking approach is a combination of structured and unstructured meshes. In multi-blocking, the domain is usually divided into numbers of small blocks, with each block meshed separately with conditions that ensure symmetry, smoothness and continuity are maintained between block interfaces to avoid numerical instability. Multi-block meshing is complex to generate but has the advantages of both structured and unstructured types of meshing. Moreover, the mesh can be easily refined or coursed accordingly due to high controlling parameters. It is strongly recommended for the types of problems where sharp edges, complex flow pattern and turbulent wake occur.

In the present case, a multi-block approach is adopted and the domain is finely meshed around the circular cylinder and near the wake portion behind the cylinder. Overall, the grid is symmetric and smooth and is divided into several zones to avoid numerical instability due to the mesh problem. Boundary layer thickness is taken as per the guidelines of Sumer and Fredsøe (1997) i.e. $O(d\sqrt{Re})$. In the case of the LES model,

a y+ value equal to or less than unity is the main requirement for accurate and high-quality results. In the current study, ICEM CFD tool is used to create the multi-grid mesh.

3.5.3 Temporal discretization

Temporal discretisation, also known as time discretisation, in which time has continuous flow, is divided into small time step Δt. Unlike spatial discretisation, temporal discretisation requires the integration of every term over a time step Δt. Two methods are used for time-dependent transient analysis: implicit and explicit methods.

In the explicit method (also referred as 'global time stepping'), the current time step value t^n is used to calculate the time t^{n+1} (Stoesser, 2001). A small time step is required for stability and convergence in the solution. In the implicit method, values at time $n+1$ are computed using the unknown values at time $n+1$. Implicit method can also work with a large time step and will be unconditionally stable, but stability does not guarantee accuracy in results. Although explicit method is computationally expensive, it results in greater accuracy compared with the implicit method.

3.6 Turbulence model

Turbulence is defined by several characteristics, including irregularity of flow, diffusivity and mixing of turbulence, length scale of turbulence, dissipation and vortical fluctuations. Attaining a definitive pattern of turbulent flow is not possible due to the nature of irregularity. Instead of an exact flow pattern, an average or approximated map is obtained using different statistical determination methods. Diffusion of the turbulence is another key characteristic that results in mixing and increases the rate of momentum, mass and heat transfer (Termekes & Lumley, 1972). In addition, boundary–layer separation is mainly influenced by the diffusion of turbulence.

Turbulence consists of eddies with a broad range of sizes. Interaction among eddies occurs in a nonlinear manner, which results in a change in orientation and shape. This process of shape change, also referred to as straining, results in the transfer of energy from large to small eddies. Owing to this transfer, large-size eddies are the most energetic and are defined in terms of shape, size and speed by flow configuration. By contrast, small-size eddies are influenced by the amount of energy entering and by viscosity. Viscosity primarily defines the scale at which energy is dissipated. Re, which is the ratio of inertial forces to viscous force, gives scholars an idea about the size of the smallest scale with respect to large-size eddies. The transfer of energy, amount of energy with respect to the size of eddies and amount of energy dissipated were first quantified by Kolmogorov (1941) and explained by Pope (2001).

As explained in section 2.6.2, three techniques, namely, DNS, LES and RANS, are primarily used to solve the mathematical model. These models are discussed in the following sections. Figure 3.4 presents the length-scale illustration resolved using the DNS, LES and RAN methods. The LES and RANS models used in the current study are explained in more detail.
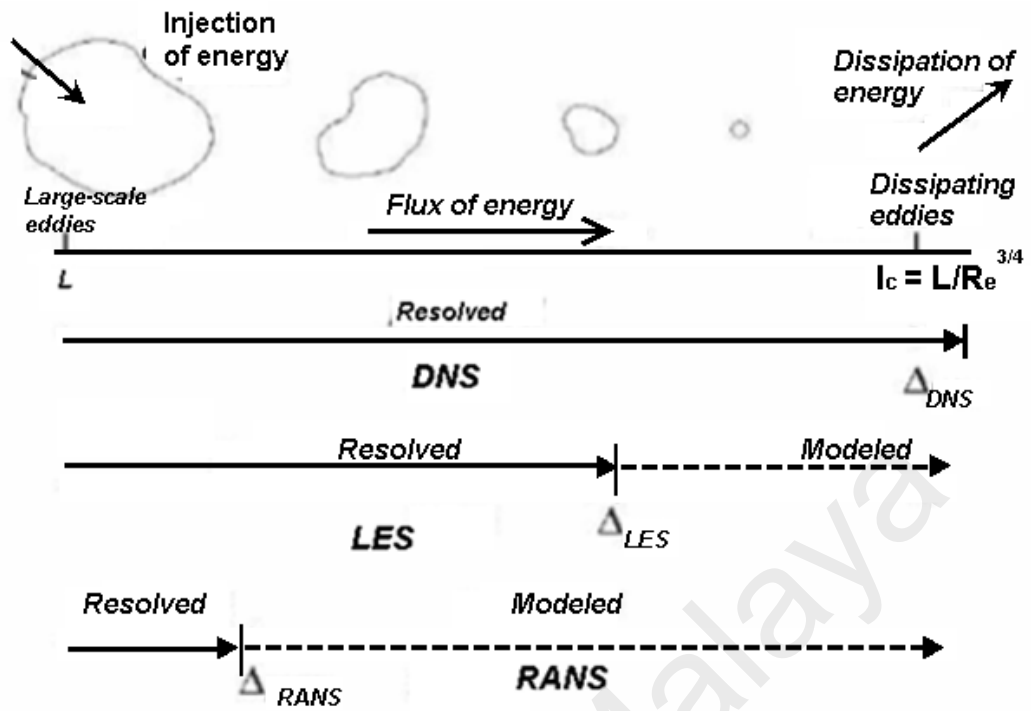
Figure 3.4: Length scales illustration using DNS, LES and RANS method

3.6.1 DNS

DNS is the simplest way to solve NS equations without taking any approximation or turbulence model in CFD calculations or simulation. DNS resolves the whole range of temporal and spatial discretisations, from the smallest dissipative scales and Kolmogorov micro-scales up to the integral scale L associated with the dissipation of energy in flow. Its great strength is its capability to provide detailed and complete information, unaffected by approximations, at all locations and at all times within the simulation period. This ability of DNS comes with a high computational cost, which limits the use of this model in general-purpose analysis and particularly at high Re. Blazek (2015) concluded that spatial resolution and computational time cost for the DNS method are proportional to $Re^{9/4}$ and Re^{3}, respectively. This conclusion is in agreement with that of Fröhlich and Rodi (2002) who found the required resolution for DNS.

DNS is widely used by researchers at low Re owing to its high accuracy and detailed insight results. F. Tremblay (2001) investigated flow around a cylinder at Re=3900 and found very accurate results compared with those from experimental data. The author also attempted to use DNS method for high Re=10000 and concluded that it will require 80 days if 32 parallel processing systems are used in the simulation. Spalart (2000) suggested that if computer technologies develop by a factor of 5 in five years, then it will take another 60 years for such technologies to be capable of simulating flow around a complete car, airplane or turbine using the DNS method.

3.6.2 LES

LES is space filtering method and it directly computes the large scale turbulence structures. The large scale turbulence is responsible for transfer of energy and momentum. The LES model has the capability to model high Reynolds number flow and resolving the 3D bluff body flow comparatively in a less costly manner. In this space filtering method, large scale turbulence is directly simulated and subgrid-scale turbulence is modelled. The difference between the large and small scales is distinguished by using filter a function Δ. In order to simulate the flow, incompressible Navier-Stokes equations need to be solved. The continuity and the momentum equation, after disregarding the commutation errors, can be written in filtered form as follow:

$$\frac{\partial \overline{u}_i}{\partial x_i} = 0 \tag{3.3}$$

$$\frac{\partial \overline{u}_i}{\partial t} + \frac{\partial (\overline{u_i}\,\overline{u_j})}{\partial x_j} = -\frac{1}{\rho}\left(\frac{\partial \overline{p}}{\partial x_i}\right) + \upsilon\left(\frac{\partial^2 \overline{u_i}}{\partial x_j\,\partial x_j}\right) - \frac{\partial \tau_{ij}}{\partial x_j} \tag{3.4}$$

where ρ, p and τ_{ij} are the density of the fluid, pressure and non-resolvable SGS, respectively. u_i represents the velocity component and over-bar shows the space filtered quantities.

$$\tau_{ij} = \overline{u_i u_j} - \bar{u}_i \bar{u}_j \tag{3.5}$$

where term τ_{ij} is known as subgrid scale (SGS) stress term. In ANSYS Fluent, SGS stresses are model by employing the famous Boussinesq hypothesis (Hinze, 1970). The most common model, used in large eddy simulations, is Smagorinsky model(Smagorinsky, 1963). In this model, the effects of turbulence are represented by eddy viscosity based on Boussinesq hypothesis.

$$\tau_{ij} - \frac{1}{3}\tau_{kk} = -2.\,v_{SGS}.\overline{S_{ij}} = v_{SGS}.\left|\frac{\partial \overline{u_i}}{\partial x_j} + \frac{\partial \overline{u_j}}{\partial x_i}\right| \tag{3.6}$$

$$v_{SGS} = (C_s\Delta)^2|\bar{S}| \tag{3.7}$$

where v_{SGS} is the SGS eddy viscosity, $\bar{S}$ is the strain rate tensor, and C_s is the Smagorinsky constant. In Smagorinsky model (ANSYS Inc. ANSYS Elements manual), C_s is taken as 0.2 values for homogenous isotropic turbulence flow but Lilly (1992) and Germano et al. (1991) developed a methodology in which value of C_s is calculated dynamically based on the given information. The complete mathematical explanation about the dynamic SGS model is available in Ferziger and Peric (2012).

In the current study, large eddy simulation model is adopted with Smagorinksy-lilly SGS model with dynamic stress enabled. SIMPLE (Semi-Implicit Method for Pressure-Linked Equations) pressure based solver is assigned to the simulation. A second-order temporal discretization scheme was used to get a stable solution. The bounded central differencing scheme was employed for spatial discretization in the momentum equations, whereas transient formulation was performed using bounded second-order implicit. According to (ANSYS Inc. ANSYS Elements manual), bounded second order implicit is consider better in term of stability and accuracy compare to second order implicit scheme. LES simulation need to be run long enough to become independent of

initial condition and enable to determine the statistics of the flow field. In current study, all the case studies were started with steady-state flow using k-ω model, and after the simulation has converged, the instantaneous field of the steady-state RANS simulation is used as an initial field for LES run. This procedure is suggested in (ANSYS Inc. ANSYS Elements manual) to reduce the simulation time. The sampling of data was taken after the simulation ran for 30 vortex shedding cycle to ensure the flow reached a statistically steady transient behavior.

3.6.3 Reynolds Averaged Navier-Stokes Simulation (RANS)

RANS equations are time-averaged equations for fluid flow derived by Osborne Reynolds. In equations of motion, turbulent flow is described by decomposing instantaneous flow quantity into mean ($\overline{U}$) and fluctuating component ($\acute{u}$). Reynolds decomposition method is adopted in the decomposition of flow variable.

$$U = \overline{U} + \acute{u} \tag{3.8}$$

$$\overline{U} = \frac{1}{T} \int_t^{i+T} u(t) dt \tag{3.9}$$

$$\acute{u} \equiv u - \overline{u} \tag{3.10}$$

In the decomposed part, T has to be large enough to obtain fully averaged values of u. The method adopted for taking the average, whether spatial or time averaging, also depends on the nature of the flow. Time averaging method is adopted for flow problems, which are steady in nature, whereas for 2D flow problems, spatial averaging method is utilised. Time averaging method is useful because flow mostly reaches a statistical steady state when ran for a long time. However, for the effectiveness of averaging, the time duration for the flow problem needs to be considerably larger than the largest timescale. Reynolds operators, which are incorporated in this method, have

set properties useful in deriving RANS equations. Assuming the flow is incompressible, the unsteady RANS equation can be written as:

$$\frac{\partial u_i}{\partial x_i} = 0 \tag{3.11}$$

$$\frac{\partial}{\partial t}(\rho u_i) + \frac{\partial}{\partial x_j}(\rho u_i u_j) = -\frac{\partial \rho}{\partial x_i} + \frac{\partial}{\partial x_j}(2\mu S_{ij} - \rho\overline{u_i' u_j'}) \tag{3.12}$$

where ρ and u_i are time-average values of pressure and velocity, respectively; μ and S_{ij} represents molecular viscosity and mean stress tensor, respectively. An additional term ($-\rho\overline{u_i' u_j'}$), known as Reynold stress tensor, describes the effect of turbulence on mean flow field due to the fluctuation part (Boussinesq, 1877).

$$-\rho\overline{u_i' u_j'} = u_i\left(\frac{\partial u_i}{\partial x_j} + \frac{\partial u_j}{\partial x_i}\right) - \frac{2}{3}\left(\rho k + u_i\frac{\partial u_i}{\partial x_i}\right)\delta_{ij} \tag{3.13}$$

where eddy viscosity μ_i, which is a scalar property, is usually computed from a transport variable; δ_{ij} is the kronecker delta; and turbulent kinetic energy k can be presented as:

$$k = \frac{\overline{\mu_i' \mu_i'}}{2} = \frac{1}{2}\left(\overline{u'^2} + \overline{v'^2}\right) \tag{3.14}$$

The Reynolds stresses are computed or approximated using different turbulence models, which are available in the literature, to close the set of equations. This estimation is executed by taking different assumptions. Each model has different limitation and drawbacks. The models include empirical and semi-empirical models, for example, k-ω model and k-ε model, and a renormalisation group model, among others. In the case of the RNG and k-ε model, isotropic eddy viscosity assumptions are taken into account, which limits the model utilisation, particularly for the problem with strong adverse pressure gradient, separation and swirl phenomenon. Eddy viscosity model is

an example of such turbulence model. Reynolds stress model (RSM) (Launder, Reece, & Rodi, 1975) tackles the limitation of the eddy viscosity model by utilising the anisotropic behaviour of turbulence. In RSM, Reynolds stresses are expressed in terms of known mean flow quantities and dynamics of turbulence are taken into account. The model is proven to be computationally expensive. Two equation models which are computationally less expensive than RSM incorporate the influence of transport turbulence quantities. In addition to energy transport, the second equation incorporates the calculation of empirical length scale. Overall, the picture shows that RANS technique describes the overview of mean quantities of flow but is unable to provide detailed insight into the effects of fluctuation terms in turbulence. k-ω model and k-ε model are the two commonly used equation models.

In case of vortex-induced vibration study, the unsteady segregated algorithm is adopted in the calculation. Pressure–velocity coupled equations are solved with the SIMPLE algorithm [(ANSYS Inc. ANSYS Elements manual)], and the implicit 1st-order scheme is utilized for unsteady terms. The 2nd-order scheme is used for k-ω transport equations and for convection terms in the momentum equations. The upwind scheme, which is of the first order, is applied to the diffusion terms.

Guilmineau and Queutey (2004) indicated that the dimensionless transverse displacement of a circular cylinder under VIV can be presented as:

$$\frac{d^2Y}{d\tau^2} + \frac{4\pi\zeta}{U_r}\frac{dY}{d\tau} + \frac{4\pi^2}{U_r^2}Y = \frac{2C_y}{\pi m^*} \tag{3.15}$$

where $Y = y/D$ represents the displacement in the transverse direction normalized by the cylinder diameter; U_r, ζ, m^*, and C_y are the reduced velocity, structural damping ratio, mass ratio, and life coefficient, respectively.

At the lock-in region, the vortex-shedding frequency approaches the cylinder oscillating frequency and the following equations prevail.

$$y = A\sin(w_{ex}t) \tag{3.16}$$

$$C_y = C_L\sin(w_{ex}t + \emptyset) \tag{3.17}$$

$$C_{Lv} = C_L\sin\emptyset \tag{3.18}$$

$$C_{La} = -C_L\cos\emptyset \tag{3.19}$$

where w_{ex} is the oscillating cylinder frequency and C_L, C_{La}, and C_{Lv} are the amplitude of the lift coefficient and its corresponding components of acceleration and velocity, respectively. Parkinson (1989) indicated that the amplitude ratio ($A^* = A_y/D$) and frequency ratio ($f^* = f_{ex}/f_n$) can be defined as:

$$A^* = \frac{1}{4}\frac{C_{Lv}}{\pi^3 m^*\zeta}\frac{f_n}{f_{ex}}\left(\frac{U}{f_n D}\right)^2 \tag{3.20}$$

$$f^* = \left[1 + \frac{1}{2}\frac{C_{La}}{\pi^3 m^* A^*}\left(\frac{U}{f_n D}\right)^2\right]^{\frac{1}{2}} \tag{3.21}$$

Eqt (10) and Eqt (11) are derived from the linearization with energy balance between the cylinder and the fluids.

3.6.3.1 *k-ε* model

The *k-ε* model proposed by (Launder & Spalding), is widely used in heat transfer and fluid flow field because of its robustness, low computational cost and considerable accuracy (H. K. Versteeg & Malalasekera, 2007). In this semi-empirical model, turbulent length and time are determined using separate transport equations. The model is based on transport equations for turbulent kinetic energy and its dissipation rate. Flow

is assumed to be fully turbulent, and an effect of molecular viscosity is neglected in the derivation of k-ε model.

k and $\boldsymbol{\varepsilon}$ are obtained from following equations:

$$\frac{\partial(\rho k)}{\partial t} + U_t \frac{\partial(\rho U_j k)}{\partial x_j} = \frac{\partial}{\partial x_j}\left(\frac{\mu_t}{\sigma_\varepsilon}\frac{\partial k}{\partial x_j}\right) + \mu_t \frac{\partial U_i}{\partial x_j}\left(\frac{\partial U_i}{\partial x_j} + \frac{\partial U_j}{\partial x_i}\right)\frac{\partial U_i}{\partial x_j} - \rho\epsilon$$

(3.22)

$$\frac{\partial(\rho\varepsilon)}{\partial t} + U_t \frac{\partial(\rho U_j\epsilon)}{\partial x_j} = \frac{\partial}{\partial x_j}\left(\frac{\mu_t}{\sigma_\varepsilon}\frac{\partial\varepsilon}{\partial x_j}\right) + C_{\varepsilon 1}\frac{\varepsilon}{k}\mu_t \frac{\partial U_i}{\partial x_j}\left(\frac{\partial U_i}{\partial x_j} + \frac{\partial U_j}{\partial x_i}\right) - \rho C_{\varepsilon 2}\frac{\varepsilon^2}{k}$$

(3.23)

Value of eddy viscosity is calculated by merging k and $\boldsymbol{\varepsilon}$:

$$\mu_t = \rho C_\mu \frac{k^2}{\epsilon}$$

(3.24)

where C_μ represents the empirical constant. The other model constants are computed from experiments for basic turbulent flow case (Shimada & Ishihara, 2002). Despite its robust formulation, reliability and low computational cost, the model is unable to solve flow with adverse pressure gradient, separation and swirl flow. The performance of the model is enhanced by introducing the modification in the model due to the known deficiencies of the k-e standard model. RNG k-ε model (Yakhot & Orszag, 1986) and realisable k-ε model are examples of the modified model, which are better in performance than the standard k-e model. In the RNG k-ε model, modification in ε equation results in an additional term, which enhances the performance for rapidly strained flows. The effect of swirl is likewise added in the model. Furthermore, through improvements in calculating Prandtl number and viscosity, the RNG k-ε model is proven to be more reliable and reasonably accurate in performance than the standard k-ε model. By contrast, the realisable k-ε model provides an alternative formulation for

turbulent viscosity. A modified transport equation for the dissipation rate (ε) is derived from an exact equation for the transport of the mean-square vorticity fluctuation. The realisable k-ε model is proven to be better than the standard k-ε and RNG k-ε models.

3.6.3.2 k-ω model

The standard k-ω two-equation model is based on the model proposed by Wilcox (1998), which provides an alternative option to cope with the limitation and restriction of the k-ε model. In the k-ω two-equation model, significant modification is included for low Re effects, compressibility and shear flow spreading. It is an empirical model similar in structure to the k-e model but based on the model transport equations for turbulence kinetic energy (k) and its dissipation rate (ω), which can be written as:

$$\frac{\partial(\rho k)}{\partial t} + U_i \frac{\partial(\rho U_j k)}{\partial x_j} = \frac{\partial}{\partial x_j}\left(\frac{\mu_t}{\sigma_\varepsilon}\frac{\partial k}{\partial x_j}\right) + \mu_t \frac{\partial U_i}{\partial x_j}\left(\frac{\partial U_i}{\partial x_j} + \frac{\partial U_j}{\partial x_i}\right)\frac{\partial U_i}{\partial x_j} - \rho k\omega \qquad (3.25)$$

$$\frac{\partial(\rho\omega)}{\partial t} + \frac{\partial(\rho U_j\omega)}{\partial x_j} = \frac{\partial}{\partial x_j}\left(\frac{\mu_t}{\sigma_\varepsilon}\frac{\partial\omega}{\partial x_j}\right) + \alpha\frac{\partial U_i}{\partial x_j}\left(\frac{\partial U_i}{\partial x_j} + \frac{\partial U_j}{\partial x_i}\right) - \beta\rho\omega^2 \qquad (3.26)$$

The dissipation rate *(ω)* performs better in solving near-wall flow compared with the ε variable of the k-ε model. In the k-ε model, fine mesh near the wall deteriorates the results, whereas in the k-ω model, fine mesh is required to resolve the flow accurately. In the k-ε model, an empirical formula is utilised to solve the near-wall flow, which also results in reducing computational cost but is unable to compute the complex flow accurately. The k-ω model directly resolved the near-wall flow with the integration of the ω equation without damping functions. Wilcox (1998) compared the efficiency of both models in computing the re-attachment length and found that the k-ε model underestimates the size of reattachment length. Morgans et al. (1999) observed the over-prediction of spreading and rate around free shear layer with the k-ω model. Table 3.1 presents the comparison between performance and capability of the k-ω and k-ε models.

Clearly, the k-ω model performs well in the near-wall region, whereas the k-ε model is better in the shear layer. To combine the advantages of the k-ε and k-ω models, Menter (1994) introduced the shear stress transport (SST) k-ω model. In this model, k-ω is utilised in the near-wall surface, whereas k-ε is employed in the near-boundary layer edge. The combination of both models results in the improved prediction of flow separation(ANSYS Inc. ANSYS Elements manual).

Table 3.1: Comparison between k- ω and k- ε model (Liaw, 2005)

	k- ω model	k- ε model
Viscous sub-layer	Simple and accurate	Complex with Less-accuracy
Fully turbulent region	Accurate	Over predicted length scale
Outer-layer	Imprecise near free shear layers	Properly defined

3.7 Mesh generation

The process of dividing the continuous domain into discretised points is known as meshing or grid generation. Variables are computed and solved at discrete points or locations. According to (Ferziger, Peric, & Leonard, 1997), grid type comes in three forms, namely, structured mesh, unstructured mesh and hybrid mesh. In the case of structured mesh, every discrete point includes the same number of neighbours except on the boundaries. This type of meshing shows good convergence and high resolution but is only effective in simple geometry cases. In the case of 'unstructured' mesh, the connectivity is irregular, and each cell possesses its own connectivity matrix. This type of mesh can be used for complex and irregular geometries. The combination of structured and unstructured mesh is known as 'hybrid meshing'. In hybrid meshing, the working domain is divided into number of subdomain and structured meshes are created at regular geometries, whereas, unstructured mesh is generated at complex location. In

the current study, an unstructured mesh is generated using the ICEM CFD tool. The general requirements for the grid are explained in the following sections.

3.7.1 General requirements of a grid

- The computational grid must discretise the domain and the surrounding boundary.

- The distribution of grid points must be adequate to represent the geometry of the region properly.

- Abundant grid points should be generated at the region where sharp gradients of flow variables are expected, such as shock wave at high speeds or region of flow separation.

- The grid should be clustered in a region where flow properties vary sharply, and few points should be used in a region with uniform flow properties to ensure satisfactory results with a given number of points.

- There should be smooth variation of the grid sizes in the adjacent elements to minimize error.

- Grid lines should not overlap to avoid a negative volume.

- The shape of the grid should be as regular as possible to obtain accurate results, especially near wall surfaces.

3.7.2 Required features of a grid generator

According to these requirements, the required features of a grid generator are as follows:

- can insert points in any input line segment to increase the grid density in any specific region;

- implements mapping that guarantees one-to-one correspondence of the physical and computational domain; moreover, the grid lines of the same family should not cross each other;

- flexible for the required generation of grids from the leading edge or trailing edge direction with variable domain size; for the cambered airfoil, the trailing edge grid is preferred in O-type mesh;

- smooth in the grid distribution;

- can generate orthogonality or near orthogonality for the grid lines, especially near the boundary;

- with grid clustering options available in near-wall regions or areas where sharp gradients of flow are expected;

- offers time-conserving grid generation; and

- flexible in terms of the variation of different parameters, such as the inlet distance from the leading edge of the airfoil or the distance from the trailing edge of the airfoil and the domain exit.

In the current study, the ANSYS ICEM-CFD tool is used in mesh generation for flow around a fixed cylinder case at the Reynolds number of $Re = 3900$. This tool is well known and powerful in modeling geometry, generating and repairing meshes for complex geometry. The ICEM-CFD tool can be used to create structured, unstructured and hybrid meshes for sophisticated CFD and structural analysis.

3.8 Solver

ANSYS Fluent offers two numerical methods, namely, pressure-based solver and density-based solver. In both solvers, a momentum equation is utilised to determine the velocity field. In the case of the density-based solver, the density field is obtained from the continuity equation, whereas the pressure field is determined from the state

equation. In the case of the pressure-based solver, a pressure correction equation is derived by manipulating continuity and momentum equations, which are used to determine the pressure field. In the current study, the flow is assumed to be incompressible in nature; thus, the pressure-based solver is used.

ANSYS Fluent offers two types of pressure-based solver algorithms, namely, segregated algorithm and coupled algorithm. The steps involved in pressure-based solution methods are shown in Figure 3.5. Firstly, fluid properties are updated on the basis of the current solution. After the update of the fluid properties, the solution variables are solved sequentially in the segregated or decoupled algorithm and solved simultaneously in the coupled algorithm. In the segregated algorithm, the updated velocity field and mass flux are used to solve pressure correction. In the case of the coupled algorithm, these steps are replaced with a single step for solving the equations of a coupled system. The remaining steps in both solution methods are the same.
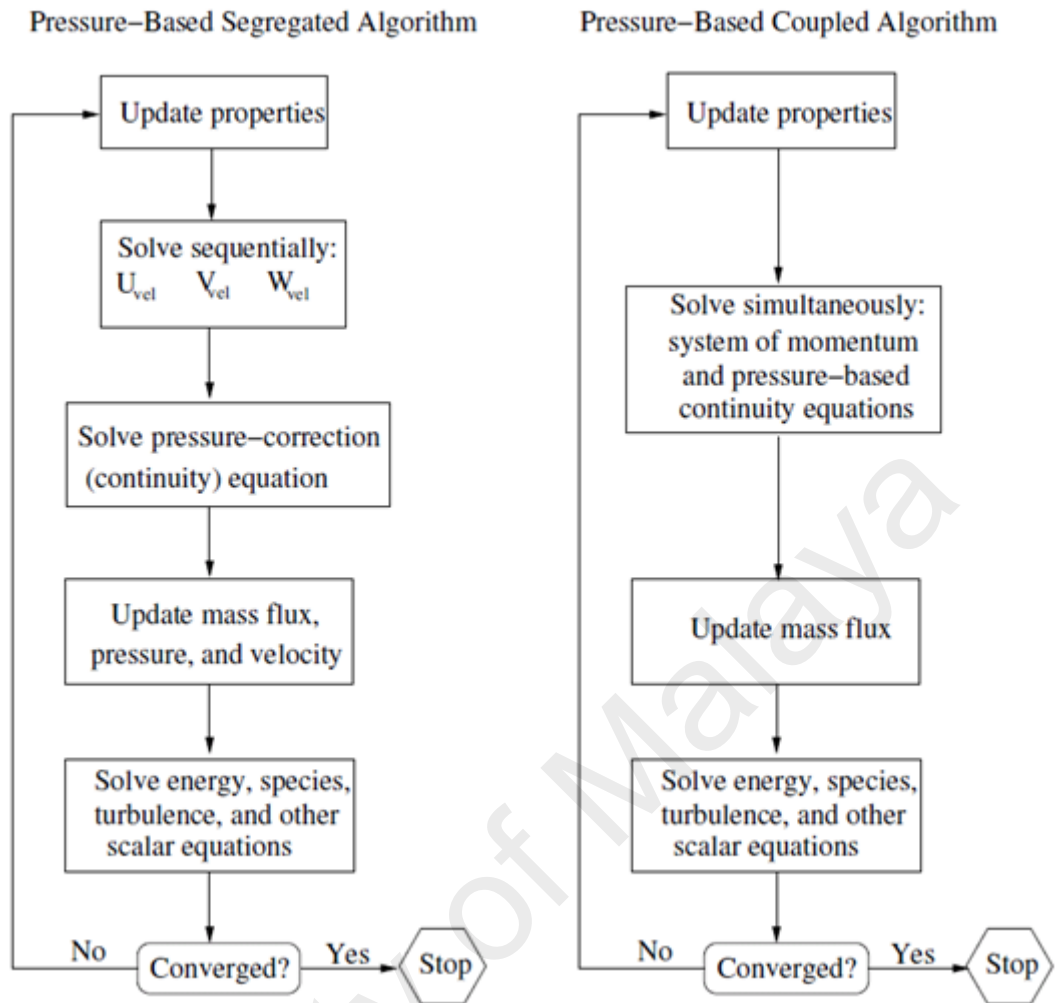
Figure 3.5: Pressure based solution steps (ANSYS Inc. ANSYS Elements manual)

In the coupled solution method, momentum and continuity equations are solved in a coupled manner, resulting in the improvement of the convergence rate. However, the memory requirement increases relative to that of the segregated algorithm. In the case of the segregated algorithm, governing equations are solved sequentially; thus, a single equation is stored; by contrast, all the momentum and pressure-based continuity equations are required to be stored in the coupled algorithm, thereby resulting in high memory cost.

In the density-based solver, all the governing equations are solved simultaneously. Additional scalars are solved thereafter in a segregated manner. Governing equations

which are nonlinear in nature require a number of iterations to generate a converged solution. The steps involved in the density-based solution method are depicted in Figure 3.6. In this method, the nonlinear governing equations are first linearized using either implicit or explicit coupled formulation in each computational cell. The transport equation for additional scalers is solved by segregating themes from the coupled set. In short, all variables are simultaneously solved in all cells in the coupled implicit method whereas whereas all variables are solved for one cell at a time in the density-based coupled approach(ANSYS Inc. ANSYS Elements manual).
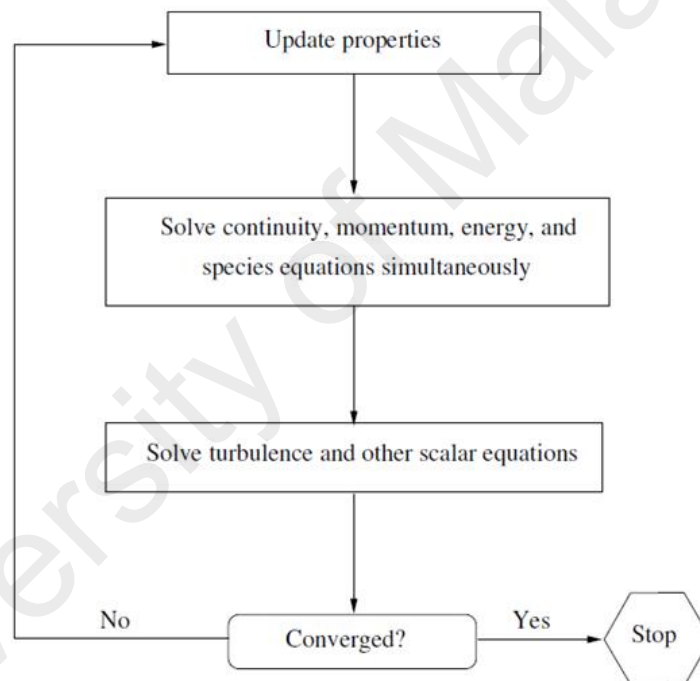
Figure 3.6: Stepwise Density based solution method (ANSYS Inc. ANSYS Elements manual)

3.8.1 Pressure-Velocity coupling equation

ANSYS Fluent provides several solution algorithms to solve pressure–velocity coupling equations. These solution algorithms include semi-implicit method for pressure linked equations (SIMPLE), SIMPLE-consistent (SIMPLEC), pressure-implicit with splitting of operators (PISO) and coupled and non-iterative time

advancement (NITA) frictional step method (FSM). SIMPLE, SIMPLEC, PISO and NITA are segregated pressure-based solvers based on a predictor–corrector approach(ANSYS Inc. ANSYS Elements manual).

3.8.1.1 SIMPLE Algorithm

SIMPLE is a segregated algorithm that is widely used for fluid flow and heat transfer problems. In this algorithm, a pressure field (p*) is estimated to resolve discretised momentum equations and the resulting velocity components u* and v*. In addition, the difference between the supposed pressure and correct pressure is defined as the correction pressure. In summary, this algorithm yields the correct velocity field (u and v), and continuity is satisfied.

3.8.1.2 SIMPLER Algorithm

The SIMPLER algorithm is an updated and revised version of SIMPLE, with the letter 'R' representing 'revised'. In this algorithm, the velocity correction of the SIMPLE algorithm is utilised to determine the velocity field.

3.8.1.3 SIMPLEC Algorithm

The SIMPLEC algorithm is a variant of the SIMPLE algorithm that offers the use of high under-relaxation terms. This algorithm achieves a comparatively quick convergence in simple problems because of pressure correction under a relaxation factor (can be set to 1.0), which speeds up the convergence rate. A high under-relaxation factor results in instability for high mesh skewness. In such a case, the SIMPLE algorithm performs comparatively well. In short, the SIMPLEC algorithm exhibits superior performance in solving problems limited to pressure–velocity

coupling. SIMPLEC also performs better than the SIMPLE algorithm in obtaining convergence for simple problems.

3.8.1.4 PISO

PISO, which belongs to the SIMPLE algorithm family, is based on the high degree of approximate relationship between the corrections for pressure and velocity. In the case of the SIMPLE and SIMPLEC algorithms, repeated calculations are required to ensure that the new velocities and corresponding fluxes satisfy the momentum balance. In the case of the PISO algorithm, it involves two additional corrections, namely, neighbour and skewness corrections, which enhance the efficiency of the algorithm. PISO is highly recommended for transient flow calculation. It also works efficiently with large time steps. In the case of LES code, in which a small time step is required, the usage of the PISO algorithm exponentially increases the computational cost. Therefore, PISO is not recommended for LES models. The PISO algorithm has the capability to maintain the stability of calculations when large time steps and an under-relaxation factor of 1.0 are used. In the case of a highly distorted mesh, the skewness correction factor is highly recommended, and the sum of the under-relaxation factors (for momentum and pressure) must be set to 1.0.

3.8.2 Frictional-step method

The FSM belongs to the NITA scheme. In this method, the momentum equations are decoupled from the continuity method using the approximate factorisation mathematical technique. After decoupling, the resulting solution algorithm is similar to the non-coupling solution algorithm. The FSM is computationally less expensive than the PISO algorithm..

3.8.3 Coupled Algorithm

In addition to the segregated algorithm, the pressure-based solver allows the solving of the flow problem using the coupled algorithm which offers some additional advantages. For steady-state problems, the coupled scheme showed better performance in terms of robustness and efficiency compared with the segregated scheme. This algorithm is also ideal when the quality of the mesh is poor or a large time step is used. However, the coupled algorithm is not compatible with NITA and fixed velocity option.

3.9 Summary

This chapter presented an overview of the CFD analysis and the various aspects affecting the numerical procedure. Although a number of turbulent models are available in the ANSYS Fluent database, only the relevant models are discussed in detail to provide information related to the studies in subsequent chapters.

For the flow around a fixed cylinder at a Reynolds number $Re = 3900$, a large eddy simulation model is adopted with the Smagorinsky–Lilly subgrid scale model with the dynamic stress enabled. Although the model is more computationally expensive than the Reynolds-averaged Navier–Stokes (RANS) model, it captures comprehensive details on the dynamic characteristics of flow. For flow around an oscillating cylinder, the RANS model equipped with SST-kω equation and a realisable k-ε (RKE) is tested.

In the case of meshing, the ICEM-CFD tool is used to investigate the variations in the meshing parameters of flow around a fixed cylinder at $Re = 3900$. For the vortex-induced vibration (VIV) study, the ANSYS built-in meshing module is used. In both cases, a y+ value of less than unity is maintained throughout the study.

CHAPTER 4: FLOW AROUND STATIONARY CYLINDER AT REYNOLDS NUMBER=3900

In this chapter, flow around cylinder has been carried out at Reynolds number (Re=3900) with large eddy simulation (LES) method using ICEM-CFD and Fluent tool for meshing and analysis, respectively. Although this issue has been explored by numerous researchers, a discrepancy still exists in the results, particularly in calculating the angle of separation, recirculation length, and statistics in the wake region behind the cylinder. In addition, the effect of spanwise domain, spanwise grid and near-field grid resolution on the wake region needs to be addressed. This study reviews previous work and performs analyses according to literature recommendations. In first section of this chapter, the effect of spanwise length (4D, 8D, and 16D), mesh resolution in the spanwise direction (1, 10, 20, 40, 60, 80 and 160 elements), and near-field grid on calculating recirculation length, angle of separation, and wake characteristics is investigated. Hydrodynamic values and pressure distribution around the cylinder are analyzed. The wake behind the cylinder is investigated within 10 diameters. This study concluded that compared to spanwise length, mesh resolution in the spanwise direction and near-field grid are more important factors for good-quality results.

In second section of the chapter, the impact of time interval averaging in obtaining fully converged mean flow field has been addressed. Turbulence statistics are sampled for 25, 50, 75, and 100 vortex shedding cycles with CFL value ranging from 0.01 to 57. Drag coefficient and Strouhal number are observed to be less sensitive whereas recirculation length appeared to be highly dependent on the average time statistics and non-dimensional time step. Similarly, the mean stream-wise and cross-flow velocity observed to be sensitive, to the average time statistics and non-dimensional time step, in the wake region near to the cylinder.

4.1 Flow around cylinder at Reynolds number=3900: Effect of Span-wise length and mesh resolution

4.1.1 Computational Domain, mesh and boundary conditions

The size of the computational domain is an essential parameter that affects the results of the flow around a cylinder both in the steady and unsteady state. The basic rule for selecting the size of domain is that it should be large enough to avoid the effect of the boundary wall in the flow around the cylinder.

Table 4.1: Summary of computational domain and mesh used in previous studies

	$L_X \times L_Y$	L_Z	Type of Mesh	$N_T \times 10^6$
Parnaudeau et al. (2008)	$20D \times 20D$	πD	Hybrid	45.8
Wissink and Rodi (2008)	$25D \times 20D$	4D-8D	O-grid	62
Breuer (1998a)	30D	πD	O-type	1.74
Tremblay et al. (2002)	$20D \times 20D$	πD	Hybrid	7.7
Lysenko et al. (2012)	50D	πD	O-type	5.76
Franke and Frank (2002)	$30D \times 20D$	πD	O-type	1.18
Prsic et al. (2014)	$32D \times 16D$	4D	Hybrid	13.5
Shao and Zhang (2006)	$40D \times 16D$	πD	O-type	0.6
Mani et al. (2009)	35D	πD	O-type	5.5
Fang and Han (2011)	$24D \times 8D$	10D	Hybrid	1.7
Meyer et al. (2010)	$30D \times 20D$	4D	Hybrid	6
Dong et al. (2006)	$40D \times 18D$	πD-1.5 πD	-	
Fang and Han (2011)	$27D \times 9D$	2.3D	Hybrid	1.44
Heggernes (2005)	$32D \times 16D$	3.288D	Hybrid	1.04
Wornom et al. (2011)	$35D \times 40D$	πD	Hybrid	1.8
Afgan et al. (2011)	$25D \times 20D$	4D	Hybrid	13

Parnaudeau et al. (2008) and Norberg (1994) concluded that aspect ratio is an important factor that influences the main flow parameters. The domain size for stream-wise (X) and cross-flow direction (Y) varies from 15D to 70D in previous studies. Table 4.1 presents the overview of domain size and mesh details of the previous studies available in literature. Most of the previous studies were conducted using rectangular and circular domain. In case of rectangular domain, the domain is divided into number of regions having structured or hybrid meshed whereas, whereas O-grid meshes were mostly used in the circular domain. Irrespective of the mesh type, grid points are clustered around the cylinder and in the wake region to resolve the boundary layer and wake region. In addition, the common feature of all meshes is to ensure the y+ value according to requirement. Rectangular domain is used in most of the studies where the size of the streamwise domain (L_X) ranges from 20D to 40D, whereas in the cross-flow direction (L_Y), the domain length ranges from 80D to 20D[Table 4.1]. In most of these cases, the mesh is divided into number of region and O-grid is surrounded around cylinder while the far region is meshed in structured shape. In case of span-wise direction(L_Z), most of the studies selected πD as depth of domain where D= diameter of cylinder, except Fang and Han (2011), and Wissink and Rodi (2008) who extended the spanwise length up to 10D. However, Wissink and Rodi (2008) varied the spanwsie size from 4D to 8D and concluded that it slightly affected the time statistics results in the cylinder wake. Afgan et al. (2011) also found that the spanwise extrusion beyond the four diameters has a less than 1% influence on the solution. Furthermore, in numerical analysis, periodic boundary conditions are assigned to the top and bottom wall which reduces the impact of aspect ratio on the results.

In this study, the domain size of 40D × 20D × 4D (streamwise × crossflow-wise × spanwise) is used [Figure 4.1]. Spanwise length of 8D and 16D is also tested. On the

basis of previous studies, where the smaller domain is selected, the current domain size is assumed to be large enough to avoid disturbance because of boundary conditions.
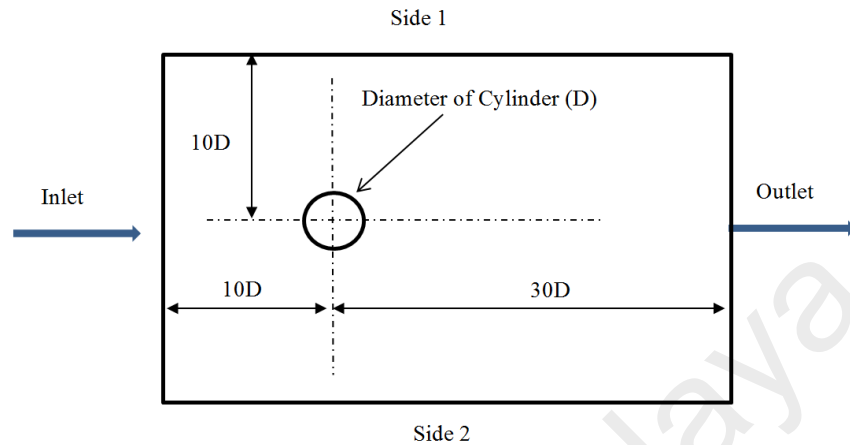
Figure 4.1: Computational domain and boundary conditions

Uniform velocity of 0.6m/s is applied at the upstream inlet of the domain, which correspond to Reynolds number of Re=3900 (when Diameter=0.1m, density=1.04kg/m^3 and viscosity $=1.6e^{-5}$ kg/m-s). No-slip effects are assigned on the cylinder wall surface where velocity increases from zero at cylinder surface to free-stream velocity away from the surface. Outlet is placed 30D downstream with an average static reference pressure of 0Pa. Side 1 and 2, which are considered to have symmetry boundaries, are 10D from above and below the centre of the cylinder, respectively, while periodic boundaries are allocated in the spanwise direction.

In this study, the mesh pattern is generated using the ICEM CFD as shown in Figure 4.2. In this multi-block O-H meshing method, the domain is divided into number of regions. Flow around cylinder at Re=3900 falls in the lower subcritical regime, where flow is characterized by laminar separation region in which the separated shear layers undergoes transition in the wake of cylinder, producing turbulent eddies periodically. Regions around the cylinder and in the wake need to be meshed adequately to ensure the boundary layer resolution. To ensure that the y+ value is less than unity,

the first node is placed at a distance of 0.002D in all the case studies. According to boundary layer analysis (Sumer & Fredsøe, 1997), the boundary layer thickness is calculated as 0.0168D on the cylinder surface, which is covered by approximately 54 around the cylinders and is sufficient to resolve the boundary layer in LES computation. Different grid variations are created by changing the number of elements in the spanwise, circumferential, and radial directions of the cylinder. Overall, the grid is made symmetric, graded, smooth, and divided into several zones to avoid numerical instabilities attributed to poor mesh quality. The non-dimensional time step Δt^+ (=$U\Delta t/D$) is maintained at 0.05, where U is the inlet velocity and Δt is the time step used in the case studies.

(a) Domain mesh   (b) magnified mesh around cylinder
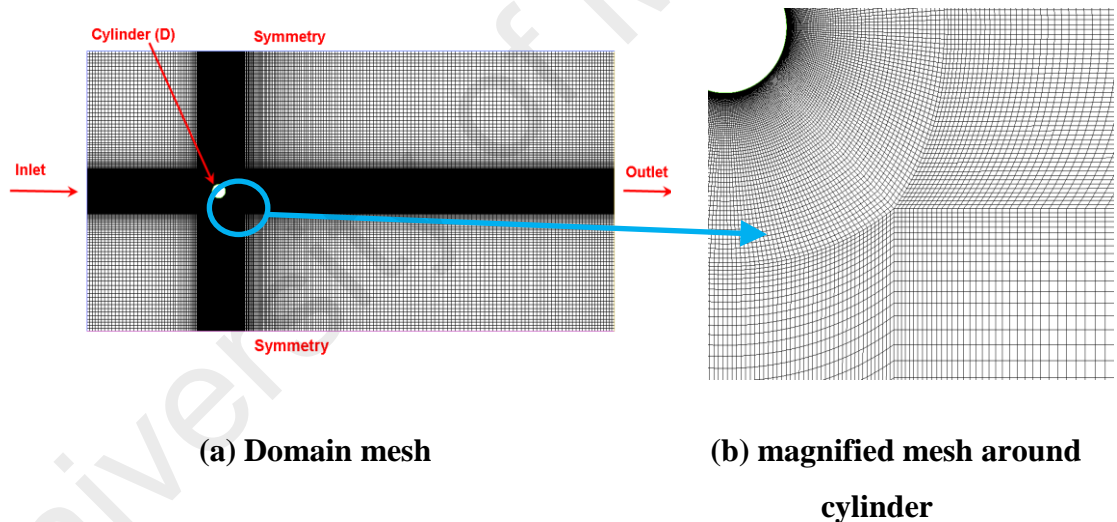
Figure 4.2: Top view of numerical mesh

4.1.2 Numerical Model

The LES model has the capability to model high Reynolds number flow and resolving the 3D bluff body flow comparatively in a less costly manner. In this space filtering method, large scale turbulence is directly simulated and subgrid-scale turbulence is modelled. The difference between the large and small scales is distinguished by using filter a function Δ. In order to simulate the flow, incompressible

Navier-Stokes equations need to be solved. The continuity and the momentum equation, after disregarding the commutation errors, can be written in filtered form as follow:

$$\frac{\partial \overline{u}_i}{\partial x_i} = 0 \tag{4.1}$$

$$\frac{\partial \overline{u}_i}{\partial t} + \frac{\partial (\overline{u}_i\, \overline{u}_j)}{\partial x_j} = -\frac{1}{\rho}\left(\frac{\partial \overline{p}}{\partial x_i}\right) + \upsilon\left(\frac{\partial^2 \overline{u}_i}{\partial x_j\, \partial x_j}\right) - \frac{\partial \tau_{ij}}{\partial x_j} \tag{4.2}$$

where ρ, p and τ_{ij} are the density of the fluid, pressure and non-resolvable SGS, respectively. u_i represents the velocity component and over-bar shows the space filtered quantities.

$$\tau_{ij} = \overline{u_i u_j} - \overline{u}_i \overline{u}_j \tag{4.3}$$

where term τ_{ij} is known as subgrid scale (SGS) stress term. In ANSYS Fluent, SGS stresses are model by employing the famous Boussinesq hypothesis (Hinze, 1970). The most common model, used in large eddy simulations, is Smagorinsky model(Smagorinsky, 1963). In this model, the effects of turbulence are represented by eddy viscosity based on Boussinesq hypothesis.

$$\tau_{ij} - \frac{1}{3}\tau_{kk} = -2.\,\nu_{SGS}.\,\overline{S_{ij}} = \nu_{SGS}.\left|\frac{\partial \overline{u}_i}{\partial x_j} + \frac{\partial \overline{u}_j}{\partial x_i}\right| \tag{4.4}$$

$$\nu_{SGS} = (C_s\Delta)^2|\overline{S}| \tag{4.5}$$

where ν_{SGS} is the SGS eddy viscosity, $\overline{S}$ is the strain rate tensor, and C_s is the Smagorinsky constant. In Smagorinsky model (ANSYS Inc. ANSYS Elements manual), C_s is taken as 0.2 values for homogenous isotropic turbulence flow but Lilly (1992) and Germano et al. (1991) developed a methodology in which value of C_s is calculated

dynamically based on the given information. The complete mathematical explanation about the dynamic SGS model is available in Ferziger and Peric (2012).

In the current study, large eddy simulation model is adopted with Smagorinksy-lilly SGS model with dynamic stress enabled. SIMPLE pressure based solver is assigned to the simulation. A second-order temporal discretization scheme was used to get a stable solution. The bounded central differencing scheme was employed for spatial discretization in the momentum equations, whereas transient formulation was performed using bounded second-order implicit. According to (ANSYS Inc. ANSYS Elements manual), bounded second order implicit is consider better in term of stability and accuracy compare to second order implicit scheme. LES simulation need to be run long enough to become independent of initial condition and enable to determine the statistics of the flow field. In current study, all the case studies were started with steady-state flow using k-ω model, and after the simulation has converged, the instantaneous field of the steady-state RANS simulation is used as an initial field for LES run. This procedure is suggested in (ANSYS Inc. ANSYS Elements manual) to reduce the simulation time. The sampling of data was taken after the simulation ran for 30 vortex shedding cycle to ensure the flow reached a statistically steady transient behavior.

Figure 4.3: Sketch of the centerline and vertical profile behind the cylinder
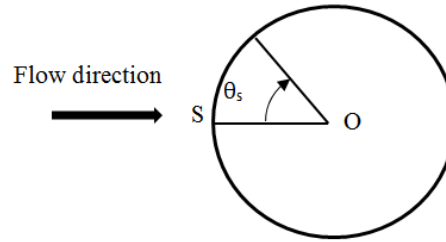
Figure 4.4: Sketch defining the separation angle measurement

4.1.3 Results and discussion

Table 4.2 shows case studies that use a spanwise length of 4D with different mesh densities (M_Z = length in spanwise direction L_Z divided by number of elements in spanwise direction N_Z) ranging from 4 to 0.05 with the elements increasing from 1 to 8, respectively. Case A, which has 1element in spanwise direction (M_Z=4), will act as 2D case study, unable to capture the turbulence behavior accurately; over-predicted the value of drag coefficient and under-predicted the value of Strouhal number. Also, a delay in the angle of separation was observed. Angle of separation (θs) is computed, as per definition in Figure 4.4, from stagnation point S to the separation point (in the clockwise direction) on wall of the cylinder, where O is the origin. In numerical simulations, the angle of separation is obtained by finding the location on cylinder surface where mean wall shear stress or skin friction coefficient is minimum. Theoretically, this point is defined as location where boundary layer separates from cylinder surface due to adverse pressure gradient. With the increase in the number of elements in the spanwise direction (N_Z), i.e., at a higher mesh density (M_Z), the solution converges with the drag coefficient, Strouhal number, and angle of separation. Case D is observed to be optimum mesh in the spanwise direction as further increase in mesh density (Case E) has very minor effect on values of drag coefficient, Strouhal number and angle of separation. From Table 4.2, it is also observed that flow around cylinder at

Reynold number Re=3900 is not a two-dimensional study and that spanwise resolution have significant influence on the results.

Table 4.2: Comparison of results with grid variation in spanwise direction

	N_Z	$M_Z = L_Z / N_Z$	$N_C * N_R$	$N_T \times 10^6$	C_d	St	θ_s	L_r/D
Case A	1	4	240*60	0.05	1.59	0.169	99.913	0.34
Case B	10	0.4	240*60	0.507	1.29	0.197	92.288	1.097
Case C	20	0.2	240*60	1.016	1.09	0.182	87.7	1.31
Case D	**40**	**0.1**	**240*60**	**2.031**	**0.98**	**0.218**	**86.188**	**1.68**
Case E	80	0.05	240*60	4.063	0.97	0.209	86.188	1.74

Additional case studies have been performed with variations in spanwise length (L_Z), spanwise mesh density (M_Z) and near field grid ($N_C * N_R$) around cylinder, where N_C is the number of elements on the circumference of cylinder and N_R is the number of elements in radial direction [Table 4.3]. Near field grid is O-shaped prism made around the cylinder surface. The size of near field grid is approximately 3times the diameter of cylinder where the centre of the cylinder is the origin. Table 4.3 show the details of additional case studies performed. In all case studies, y+ value less than unity is maintained for stable simulation. From Case D to Case I, spanwise length (L_Z) of 4D is used with a mesh density that ranges from 0.1 to 0.067. Results obtained in these cases are well converged except for the Case H where number of elements on cylinder surface (N_C) is reduced from 320 to 200. Reduction in number of division on cylinder surface results in over-prediction of Cd, shorter recirculation length and delay in separation. Moreover, an increase in N_C and N_R from 240 to 320 and 60 to 80, respectively, has a negligible effect on the results. According to Ma et al. (2000), and Wissink and Rodi (2008), spanwise domain and resolution is major contributor to predict the accuracy in recirculation length. Breuer (1998a) and (Kravchenko & Moin, 2000) concluded that the domain size in the spanwise direction is less dependent on the results if the mesh

density remains constant. To investigate the impact of spanwise length on solution, additional case studies (J to O) are performed with spanwise length (L_Z) of 8D and 16D having N_C and Nr of 240 and 60, respectively.

From Case J to Case L, spanwise length (L_Z) of 8D is used with mesh density (M_Z) varying from 0.2 to 0.1. Convergence in results is obtained at Case L having M_Z of 0.1, L_Z of 8D, N_T of 4.063×10^6. Angle of separation and recirculation length of of 86.18 and 1.70, respectively, is computed in Case L, which agrees well with the results of Case D with the same mesh density but smaller L_Z. The mesh densities of 0.2 and 0.133 are used in Cases J and K, resulting in a shorter recirculation length and delay in separation.

From Cases M to O, the spanwise length (L_Z) of 16D is used with mesh density (M_Z) varying from 0.4 to 0.1. Mesh densities of 0.4 and 0.2 are used in Cases M and N, thereby resulting in a shorter recirculation length and delay in angle of separation. With the same mesh density (M_Z) of 0.2, almost similar results were obtained by Case N with L_Z of 16D, N_T of 4.063×10^6, Case J with L_Z of 8D, N_T of 2.031×10^6, and Case C with L_Z of 4D, N_T of 1.06×10^6. Similarly, the results of Case O with L_Z of 16D, N_T of 8.12×10^6, Case L with L_Z of 8D, N_T of 4.063×10^6 and Case D with L_Z of 4D, N_T of 2.031×10^6, are similar in nature when the mesh density is fixed at 0.1. Irrespective of the spanwise length and total number of elements, the results converge at a mesh density of 0.1, and an increase in mesh density will only increase the computational cost. Furthermore, the results of Cases D, J, and O agree with the experimental results [Table 4.4]. Thus, instead of spanwise length, the mesh density in the spanwise direction and the near-field grid should be the subject of focus.

Regarding the uncertainty in calculating the recirculation length, Parnaudeau et al. (2008) observed uncertainty of 10% when data were collected with averaging time of

52 vortex shedding cycle. Wissink and Rodi (2008), Wissink and Rodi (2008), Meyer et al. (2010) and Mani et al. (2009) results were based on the collected data of about 60 vortex shedding cycles. Lysenko et al. (2012) considered 150 vortex shedding cycles sufficient for fully established wake whereas Franke and Frank (2002) collected the data on the basis of 200 vortex shedding cycle but was unable to compute converge value of recirculation length. In current study, the data is taken over average of 50 vortex shedding cycles and the converge value of recirculation length is observed due to the methodology adopted [as explained in 4.1.2]

Table 4.3: Comparison of results with grid variation in near field and spanwise direction

	$N_T \times 10^6$	L_Z	N_Z	$M_Z = L_Z / N_Z$	$N_C * N_R$	C_d	St	θ_s	L_r/D
Case D	2.031	4D	40	0.1	240*60	0.98	0.218	86.188	1.68
Case F	2.220	4D	40	0.1	240*80	0.97	0.208	86.188	1.71
Case G	3.064	4D	40	0.1	320*80	0.97	0.207	86.014	1.79
Case H	2.728	4D	60	0.067	200*60	1.11	0.21	89.08	1.18
Case I	3.330	4D	60	0.067	240*80	0.97	0.21	86.18	1.71
Case J	2.031	8D	40	0.2	240*60	1.1689	0.195	87.71	1.17
Case K	3.0472	8D	60	0.133	240*60	1.00	0.206	86.18	1.57
Case L	4.063	8D	80	0.1	240*60	0.986	0.205	86.18	1.70
Case M	2.031	16D	40	0.4	240*60	1.28	0.187	90.76	0.75
Case N	4.063	16D	80	0.2	240*60	1.04	0.195	87.71	1.35
Case O	8.12	16D	160	0.1	240*60	0.982	0.21	86.18	1.73

Table 4.4 shows the value of drag coefficient, Strouhal number and recirculation length of present studies (Case D, Case L and Case O) in addition to experimental studies and numerical studies. Value of Cd and St agreed well with the other studies, except the Liaw (2005) who used SST model near the cylinder wall, which resulted in lower Cd.

Comparison shows that current study results well agreed with the other numerical and experimental studies. Uncertainty in value of recirculation length is depicted in the experimental (ranges from 1.19 to 1.56) as well as in numerical studies (ranges from 1.02 to 1.64). The results for the L_Z of 4D, 8D, and 16D show that spanwise length has a negligible effect on calculating the recirculation length. Also the current results are more close to experimental results (Parnaudeau et al., 2008) and numerical results ((Dong et al., 2006), (Lysenko et al., 2012), (Franke & Frank, 2002), (Ouvrard, Koobus, Dervieux, & Salvetti, 2010) and (Afgan et al., 2011)). Regarding angle of separation, most of the other numerical studies result in delay in separation. Current study very well capture the separation point which is close to the experimental study of Lourenco and Shih (1993).

Table 4.4: Comparison between experimental and numerical result at Re = 3900

|	C_d	St	L_r/D	θ_s
Experiment (Norberg, 1987)	0.98±0.005	0.215±0.005	1.33±0.2	-
Experiment (Lourenco and Shih (1993)	0.99	0.22	1.19	86
Experiment (Ong & Wallace, 1996),	0.98±0.05	0.21		
Experiment (Parnaudeau et al., 2008)		0.21	1.56	
DNS (Dong et al., 2006)	-	0.203	1.47	-
LES (Tremblay et al., 2002)	1.15	0.215	1.02	86.5
LES (Mani et al., 2009)	0.99	0.21	-	86.3
LES (Lysenko et al., 2012)	0.97	0.209	1.67	89
LES (Kravchenko & Moin, 2000)	1.04	0.210	1.35	88.0
LES Beaudan and Moin (1994)	0.92-1.00	0.203-0.209	1.36-1.74	85.8
LES (Liaw, 2005)	0.88	0.250	1.04	91
LES (Franke & Frank, 2002)	0.99	0.209	1.64	88.2
LES (Droge, 2007)	1.01	0.210	1.26	87.7
LES (Wornom et al., 2011)	0.99	0.21	1.45	89
LES (Ouvrard et al., 2010)	0.94	0.22	1.56	
LES (Park, Lee, Lee, & Choi, 2006)	0.99	0.212	1.37	-
LES (Afgan et al., 2011)	1.02	0.207	1.49	86
Present-Case D	**0.98**	**0.218**	**1.68**	**86.18**
Present-Case L	**0.986**	**0.205**	**1.70**	**86.18**
Present-Case O	**0.982**	**0.21**	**1.73**	**86.18**
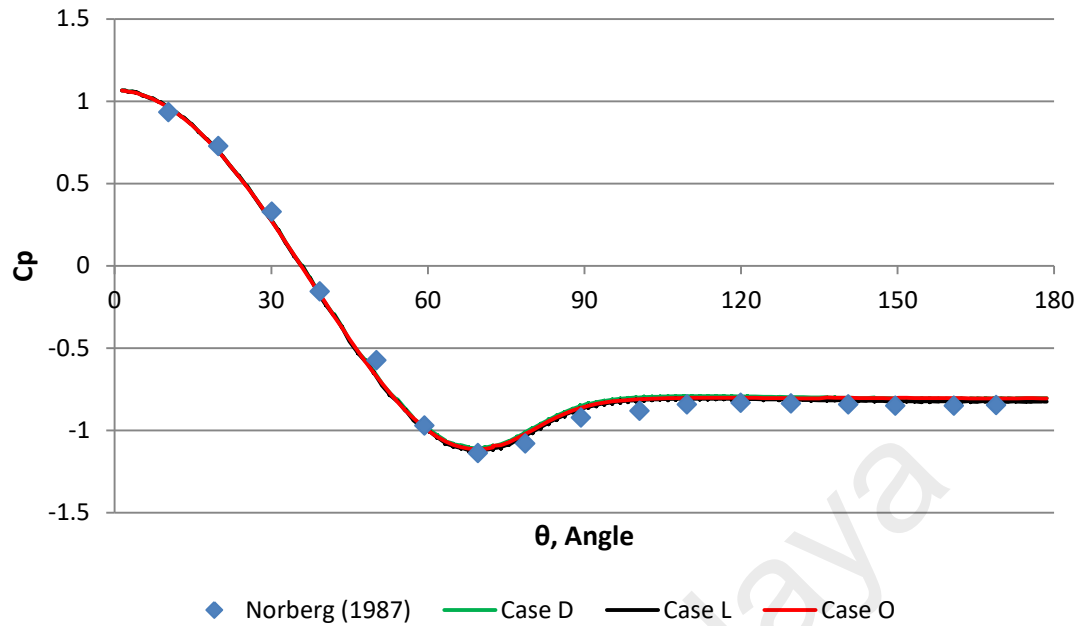
Figure 4.5: Pressure Coefficient on cylinder surface

Figure 4.5 shows the pressure distribution around the cylinder surface together with the experimental results of Norberg (1987)[Re=4020]. Current study shows that the results are in good agreement with the experimental results

Figure 4.6 shows the mean stream-wise velocity profiles in the wake of cylinder. The mean velocity is computed at centre-line up to 10-diameter behind the cylinder as sketched in Figure 4.3. It is observed from the results that DES show a bit smaller recirculation length compare to the experimental results. Moreover, a slight difference is observed between the experimental result and the results of the present study, but this difference may be due to the PIV method used by Lourenco and Shih (1993), where external disturbance will result in early transition of the separating shear layer (Kravchenko & Moin, 2000). Overall, the present case study show good agreement with previous experiments and the recirculation length of LES case study is in good accuracy with the experimental results performed by Lourenco and Shih (1993).
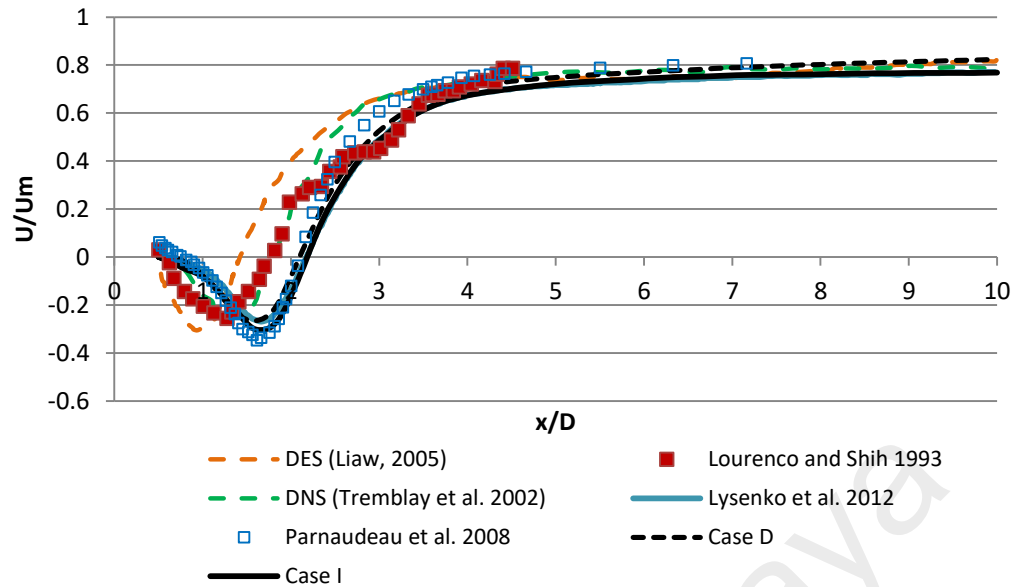
Figure 4.6: Mean streamwise velocity in wake behind the cylinder upto 10D

Figure 4.7 shows the mean stream-wise velocity component in comparison with the previous studies in the wake region (at x/D=1, x/D=3 and x/D=5). The range of data is from y/D = -3 to y/D=3. The mean stream-wise velocity is normalized by dividing with the inlet velocity. The profile picture of the results show that the numerical study is in very better comparison with the experimental results. Although there is very small difference in peak at x/d=1 but that difference may be due to experimental method used by Lourenco and Shih (1993) in which some external disturbance may result in early transition and separating shear layers. "U" shape profile is observed at x/d=1 which is showing the accuracy of current results. Kravchenko and Moin (2000) discussed in detail about the shape of profile. According to the author the "V" shape profile is observed in the cases where the grid resolution is coarse enough in spanwise direction as shown in Case A and Case B (Figure 4.7). Furthermore, the profile of coarse cases (Case A and Case B) at x/D=1 are in more good agreement with experimental result of Lourenco and Shih (1993) which also prove the earlier observation relating to the external disturbance in experimental study.
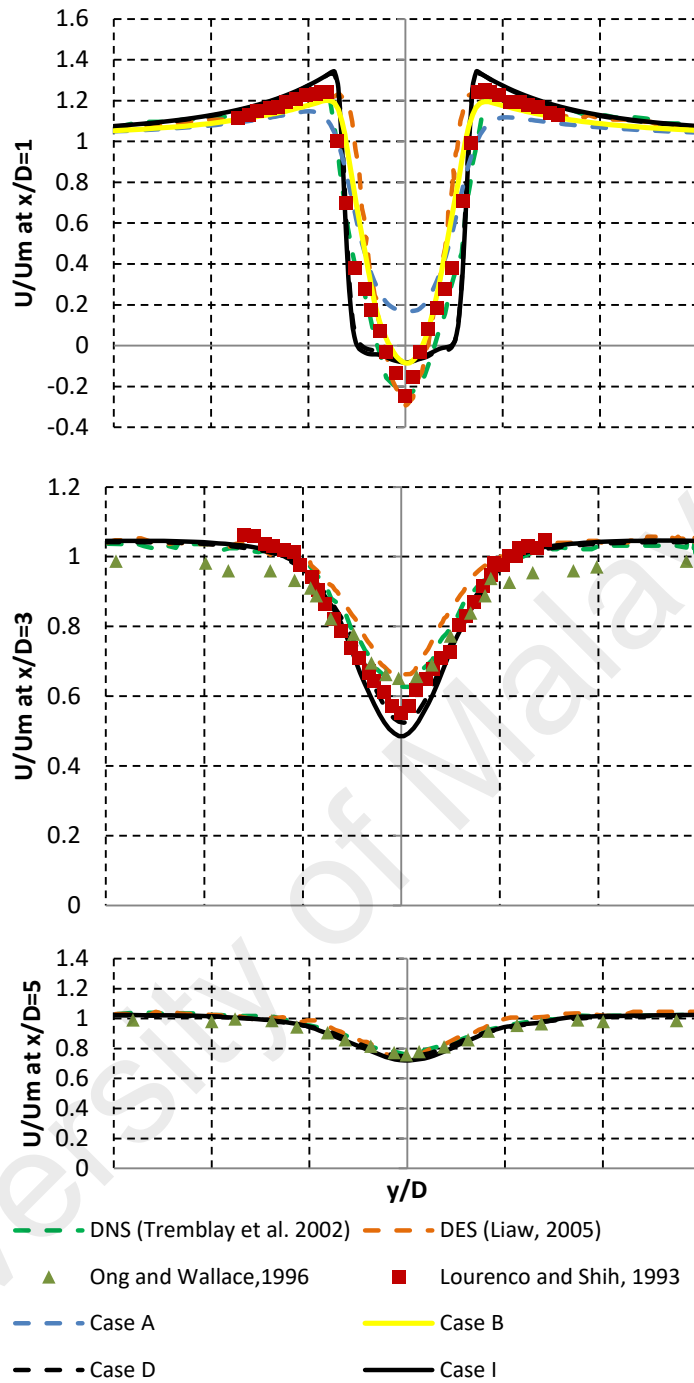
Figure 4.7: Mean stream-wise velocity component of the flow around a circular: Comparison between present study and experimental studies from literature
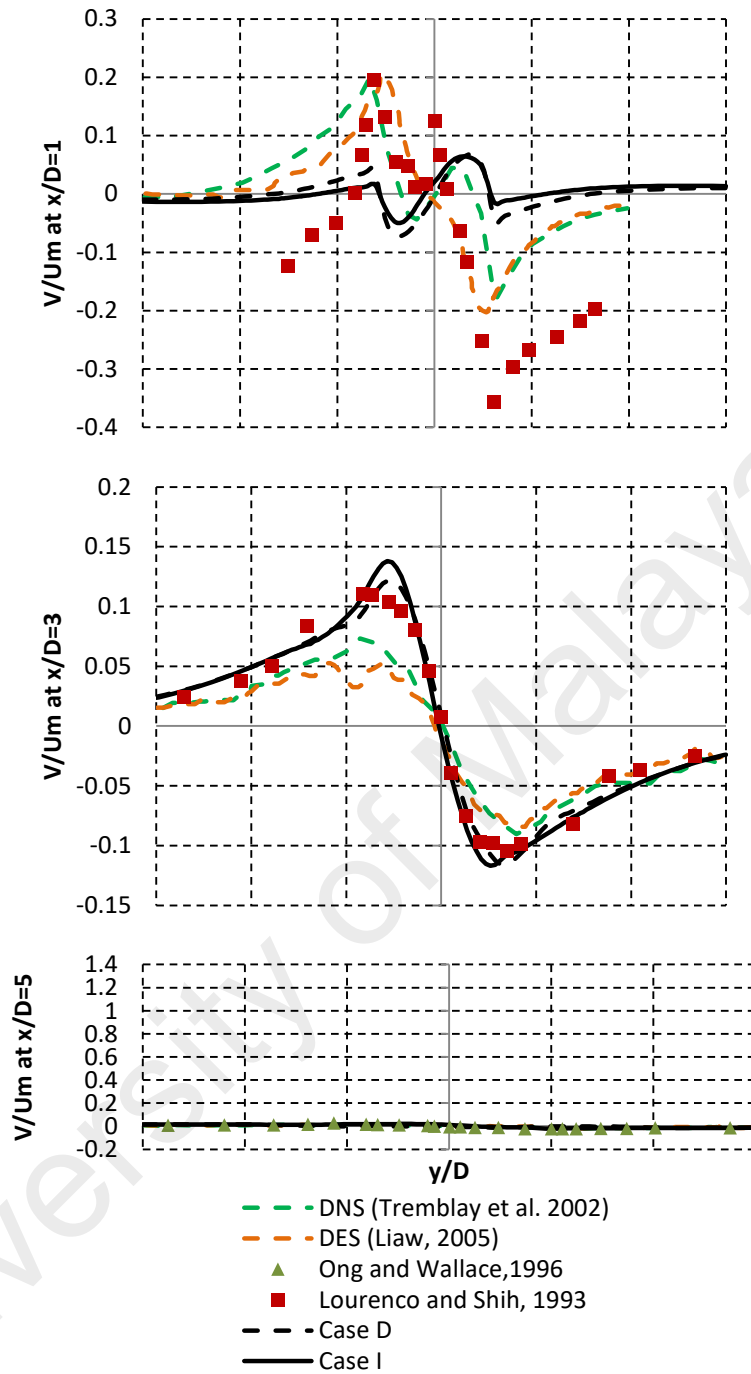
Figure 4.8: Mean cross-flow velocity component in the wake region behind the cylinder: Comparison between experimental and present study

Figure 4.9: Mean Reynold shear stress: Comparison between Experimental studies and present

Figure 4.8 and Figure 4.9 present the mean cross-flow velocity component and mean Reynold shear stress, respectively, in the wake region at x/D=1, x/D=3 and x/D=5. In the wake region close to cylinder i.e. at x/D=1 there is discrepancy in comparison

between the experimental results by Lourenco and Shih (1993) and current study, but the profile of the mean cross-flow v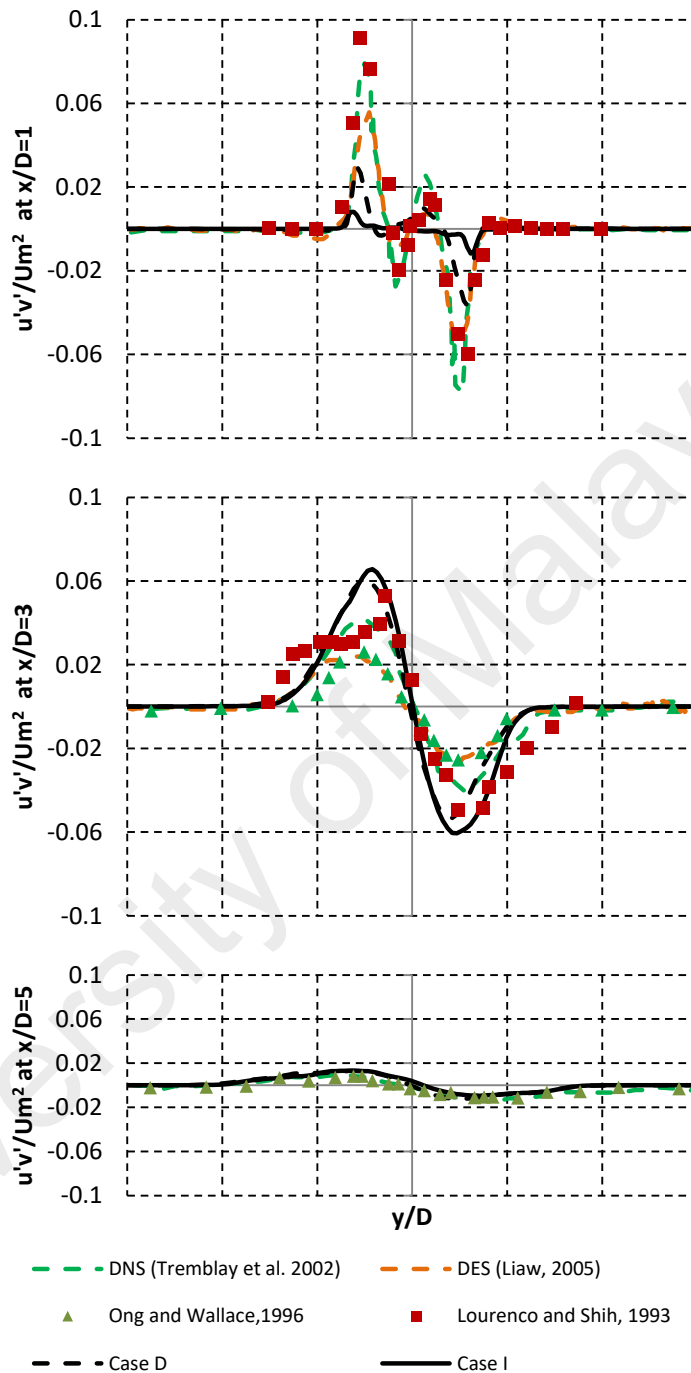elocity component of simulations by Tremblay et al. (2002)(DNS study) and Liaw (2005) is in good agreement with the current LES study. Away from the cylinder, the results are well captured by the present LES study. Norberg (1994) and Szepessy and Bearman (1992) studied the wake flow near cylinder with different geometry parameters and concluded that span-wise end condition have very significant effect the onset shear layers instability. In case of simulations, the periodic boundary conditions is applied in the span-wise faces due to which aspect-ratio dependency on result near the cylinder wake is not applicable but grid independency study is very essential near the wake to get the accurate results.

4.1.4 Summary

Flow around a cylinder was simulated using LES model at Reynold number 3900. Drag coefficient, Strouhal number, angle of separation and recirculation length are very well captured compared to the other simulations and experimental studies. Spanwise resolution and near-field grids significantly affect the calculation of the recirculation length, angle of separation, and statistic in the wake region behind the cylinder. This study also found that coarse mesh in the spanwise direction results in an over-predicted drag value, a delay in the angle of separation, an underestimated Strouhal number, and a short recirculation length. Furthermore, after gaining the stability it is suggested to take the results of 50vortes shedding cycles which will ensure the fixed recirculation length. In addition, a coarse mesh resolution in the spanwise direction resulted in a V-shaped profile for the mean stream velocity at x/D = 1. The results of this study are consistent with the experimental results, and a better profile than the other simulation results was predicted. Experimental results showed that aspect ratio significantly affects the results in the wake close to the cylinder, whereas simulations results are highly dependent on the mesh density in span-wise direction.

4.2 Flow around circular cylinder at Reynolds number =3900: Impact of averaging time on the accuracy of statistical quantities

The objective of this section is to investigate the impact of averaging time on computing recirculation length, angle of separation, hydrodynamic coefficients and other statistical quantities at Reynolds number 3900. The domain size, boundary condition and mesh type used is same as explained in section 4.1.1. In this case, cylinder circumference is divided in 320 elements while the growth rate of 1.05 is assigned in radial direction. In order to ensure, smoothness and continuity, the growth rate is kept constant in far region as well. In spanwise direction, the length is divided in 60 elements. Like previous section, y+ criteria less than unity is maintained by keeping first node at 0.0015D in all case studies. 66nodes are assigned to boundary layer thickness to ensure proper resolution of boundary layer. All the case studies are performed using Large Eddy simulation code with Smagorinsky–Lilly subgrid-scale (SGS) model. The dynamic SGS option activated due to its better performance as depicted in reference (Kravchenko & Moin, 2000). Similarly like procedure followed in section 4.1, the simulation is initiated with steady-state flow using k-ω model until the flow field become stable and converged. After getting stability, the instantaneous velocity field of steady-state simulation is used as an initial condition for LES simulation. The LES code is run for 30 vortex shedding cycles before the time averaging started.

Keeping y^{+} value less than unity, the simulations are performed with range of Courant–Friedrichs–Lewy condition (CFL) from 1 to 57 and results are recorded for vortex shedding 25, 50, 75 and 100.

4.2.1 Results and discussion

To obtain a solution independent from the initial condition, simulations are executed for 25 vortex shedding cycles before calculation for the time-average statistics is started. The simulations are performed with non-dimensional time step $T_1=\Delta t_1.U/D=0.0008$, $T_2=\Delta t_2.U/D=0.001$ $T_3=\Delta t_3.U/D=0.01$ and $T_4=\Delta t_4.U/D=0.05$. The results are recorded after 25, 50, 75 and 100 vortex shedding cycles. To show the difference between the results obtained at different non-dimensional time steps, the results are plotted after 25 vortex shedding cycles. The results obtained after 50, 75 and 100 vortex shedding cycles are presented in Table 4.5.

Figure 4.10 shows the comparison between mean pressure coefficient plot around the cylinder surface obtained from the experimental study of Norberg and the present numerical case studies for the time-average statistics of 25 vortex shedding cycles with non-dimensional time step $T_1=\Delta t_1.U/D=0.0008$, $T_2=\Delta t_2.U/D=0.001$, $T_3=\Delta t_3.U/D=0.01$ and $T_4=\Delta t_4.U/D=0.05$. A wide range of variation in flow separation region ($60°–90°$) is observed between the T_4 case study and the experimental study of Norberg. The difference between the plots of experimental and case studies with small time step, i.e. $T_1=\Delta t_1.U/D=0.0008$ and $T_2=\Delta t_2.U/D=0.001$, is marginal. Figure 4.10 clearly depicts that diverse pressure gradient at the flow separation region can only be well captured with a non-dimensional time step value fulfilling the CFL criteria of CFL≤1.
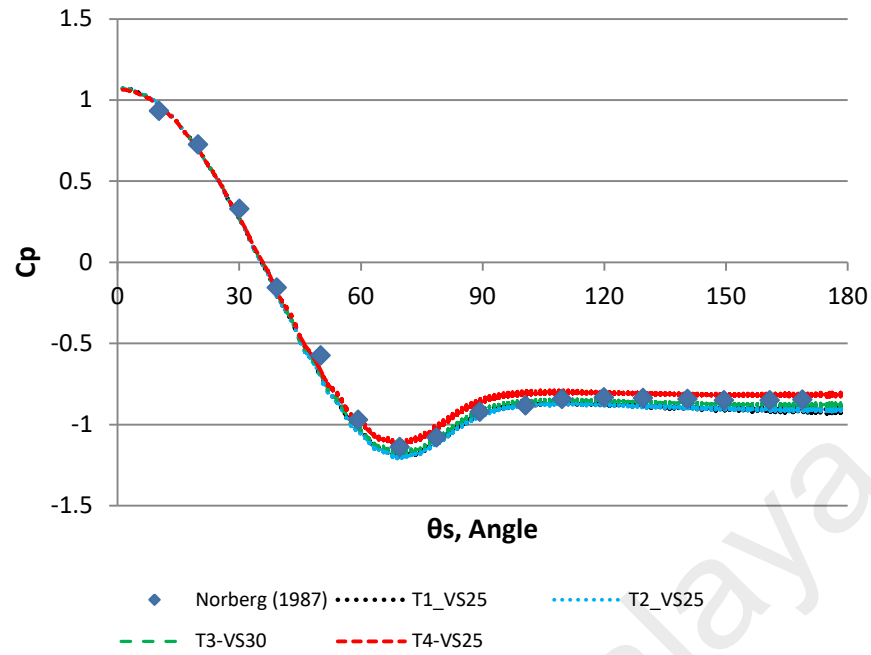
Figure 4.10: Mean Pressure coefficient around cylinder: Experimental Vs present study

Table 4.5 presents the comparison of results of the previous large eddy simulation (LES) studies and those of the current work. In this study, the results are taken after 25, 50, 75 and 100 vortex shedding cycles. In most of the previous studies, results were taken at a time average of less than 50 vortex shedding cycles, except in Parnaudeau et al. (2008) where the average statistical results were obtained after 250 vortex shedding cycles. The Strouhal number is observed to be least sensitive to the time-average statistic and the non-dimensional time step. In both the previous LES studies and the current cases, the Strouhal number is within the 0.19–0.21 range. Similarly, the drag coefficient is comparatively less sensitive to the number of time-average statistics, and a Cd value of 0.96–1.1 is computed in all the previous LES studies. The exception is Fröhlich et al. (1998) where an unstructured tetrahedron mesh deteriorated the results. In the current study, a slight variation is observed in computing the values of Cd in the case studies of T_1, T_2 and T_3. In the case of T_4, high values of non-dimensional time step underestimate the value of Cd and the increase in time-average statistic, slightly

improving the results. The separation angle is a point on the cylinder circumference, where wall shear stress or skin friction coefficient is at its minimum. A wide range of variation is observed in previous LES results ranging from 85° to 89°. In the current study, angle of separation is observed to be less sensitive to the average number of time statistics and a value of 87.15 is computed in the T_1, T_2 and T_3 case studies. In the case of T_4, which does not fulfil the CFL requirement of CFL≤1, the numerical simulations underestimated the separation angle. The authors observed that the separation angle highly depends on the number of elements at the circumference of the cylinder. In this study, the grid utilized has higher resolution in the circumferential direction compared with that in previous studies [(Franke & Frank, 2002) (Beaudan and Moin (1994) (Kravchenko & Moin, 2000), (Breuer, 1998b) (Rajani et al., 2016) and (Fröhlich et al., 1998)], to ensure better results.

In the case of recirculation length, a wide range of uncertainty is observed in previous studies, and the length ranges from 0.80 [due to use of an unstructured tetrahedron grid by Fröhlich et al. (1998)] to 1.68. In addition to other computational parameters, recirculation length is highly dependent on the number of time-average statistic and non-dimensional time step. In the case of T_1 and T_2, a recirculation length of 1.28 is computed after 25 vortex shedding cycles, which increase to 1.44 and 1.38, respectively, after 50 vortex shedding cycles. In the cases of T_1 and T_2, the converged value of recirculation length is computed after 75 vortex shedding cycles. It is worth to mention that the cases of T_1 and T_2 fulfill the criteria of CFL≤1. In the case of T_3, where the maximum value of Co number is 11 and the Co number is less than 1 for most of the computational domain, Lr=1.28 is obtained after 25 vortex shedding cycles, which increased to Lr=1.51 after 75 vortex shedding cycles.. The Lr values observed to be higher in the case of T_3 in comparison with those in T_1 and T_2. In case of T_4, where CFL

Table 4.5: Comparison of results

		Number of vortex shedding cycles	C_d	Lr/D	Angle of separation	St
Rajani et al. (2016)		20	1.05	1.211	87.5	0.214
Shao and Zhang (2006)		15	1.03	1.21	-	0.218
Kravchenko and Moin (2000)		7	1.04	1.35	88	0.210
R. Mittal and P. Moin (1997)		12	1.00	1.40	86.9	-
Beaudan and Moin (1994)		30	1.00	1.36	85.8	0.203
		30	0.96	1.56	85.3	0.216
Parnaudeau et al. (2008)		250		1.56	-	
Fröhlich et al. (1998)	Unstructured	20	1.45	0.80	-	0.216
	Structured	86	1.08	1.09		0.216
Mani et al. (2009)		60	0.99	-	86.3	0.206
Young and Ooi (2007)	Lz=32	30	1.04	1.4	-	0.212
	Lz=48	30	1.03	1.35	-	0.212
Breuer (1998b)	Quick-Smg	22	0.969	1.686	86.7	
	CDS-4, Smg	22	1.071	1.214	87.6	
	CDS-2, Dyn	22	1.016	1.372	87.4	
(Franke & Frank, 2002) LES		10	1.005	1.34	89.0	0.209
		31	0.994	1.51	88.5	0.209
		42	0.978	1.64	88.2	0.209
$T_1=\Delta t_1.U/D=0.0008$		25	1.048	1.28	87.155	0.208
		50	1.022	1.44	87.153	0.207
		75	1.0297	1.46	87.1524	0.207
		100	1.0324	1.46	87.15492	0.207
$T_2=\Delta t_2.U/D=0.001$		25	1.04489	1.28	87.155	0.207
		50	1.02265	1.38	87.1549	0.208
		75	1.03191478	1.43	87.15502	0.207
		100	1.03	1.43	87.155	0.207
$T_3=\Delta t_3.U/D=0.01$		25	1.0565	1.280	87.15507	0.213
		45	1.042	1.47	87.15229	0.206
		57	1.041	1.52	87.153	0.207
		75	1.02446	1.51	87.15504	0.21
		100	1.028104	1.51	87.15229	0.21
		150	1.017596	1.52	87.15229	
$T_4=\Delta t_4.U/D=0.05$		25	0.98074	1.75	86.01379	0.198
		50	0.981235	1.79	86.01379	0.202
		75	0.975312	1.78	86.01379	0.204
		100	0.975348	1.73	86.01379	0.204
		125	0.977239	1.73	86.01398	0.204
		200	0.982845	1.73	86.01398	0.204

value is higher than 10 at adverse pressure gradient region, higher value of recirculation length (Lr=1.75) is computed after results are taken at 25 vortex shedding cycles. The converged value of recirculation length is observed after 100 vortex shedding cycles. In the current study, recirculation length value observed to be highly sensitive to non-dimensional time step and time-average statistics.

Figure 4.11 and Figure 4.12 present the mean streamwise and crossflow velocity at x/D=1, 3 and 5, where D is diameter of cylinder and x is distance from centre of cylinder. In Figure 4.11 and Figure 4.12, only the results computed after 25 vortex shedding cycles is included to observe the difference between the previous and current studies at different non-dimensional timestep. The difference is significant near the wake behind cylinder i.e. x/d=1 where the T4 case study show U-shaped profile which not agreed with the V-shaped profile of the Lourenco and Shih (1993), Liaw (2005) and Tremblay et al. (2002). As the non-dimensional time step decreased, the mean velocity profile becomes the V-shaped as shown in case of T_1 and T_2. At far wake region, the difference between the current case studies decreased and become negligible at x/D=5. Same behavior is observed in Figure 4.12 where the profile of mean streamwise velocity of T_1 and T_2 case studies is acceptable compared to the previous studies. At the far wake region behind the cylinder, the difference between T_1, T_2, T_3 and T_4 and previous studies is negligible.
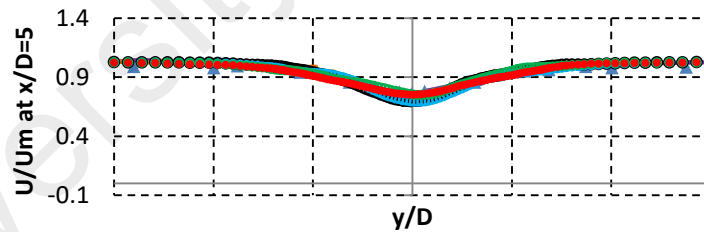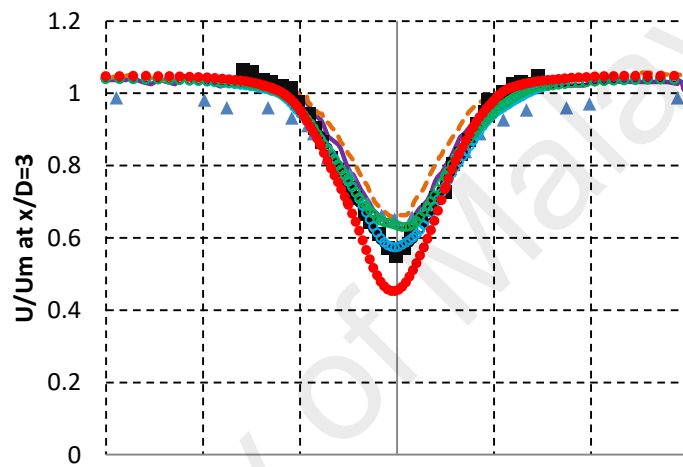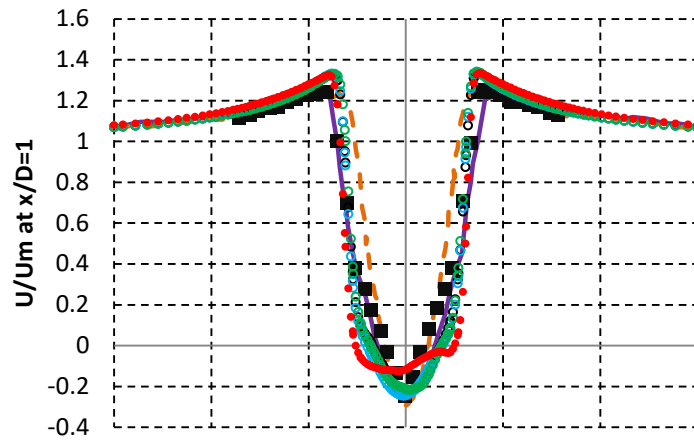
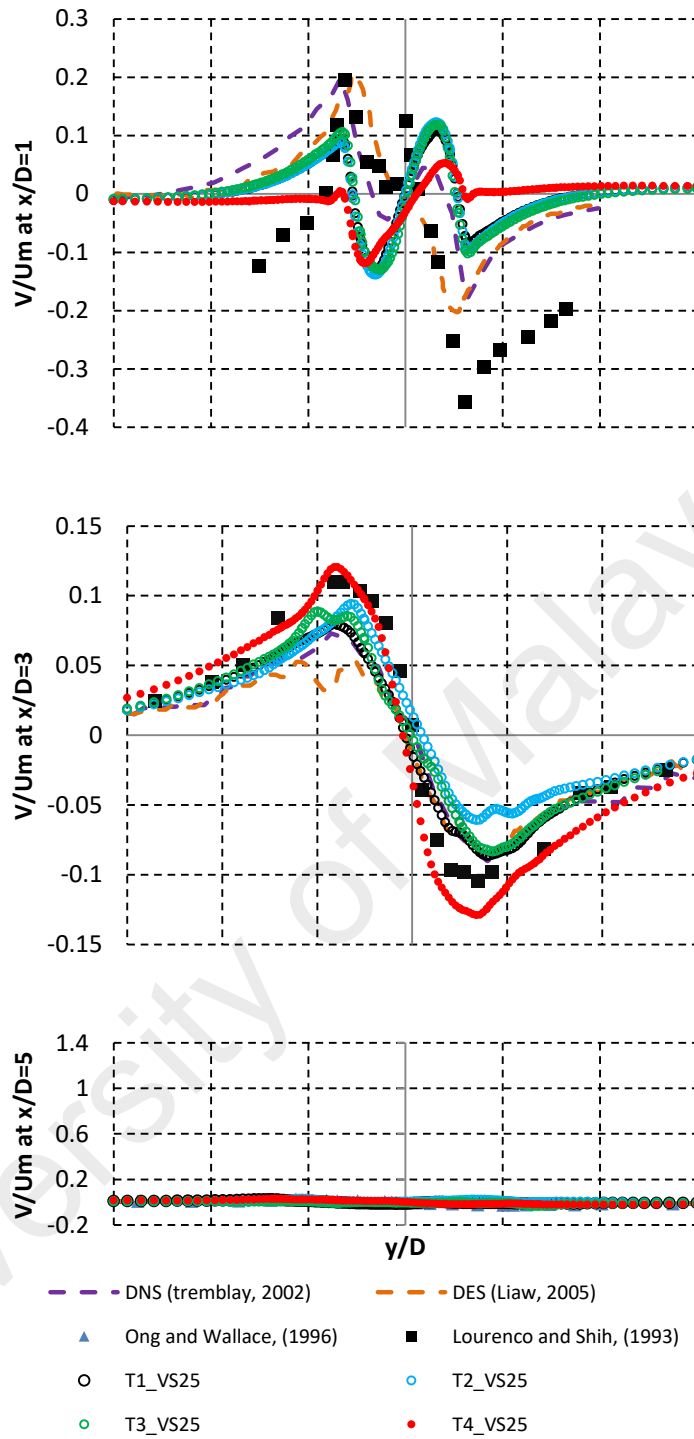**Figure 4.11: Mean streamwise velocity at x/D=1, 3 and 5**

Figure 4.12: Mean crossflow velocity at x/D=1, 3 and 5

4.2.2 Summary

Numerical simulations for flow around fixed cylinder at Reynolds number Re=3900 has been performed using LES code with dynamic SGS model. The study mainly analyzed the impact of non-dimensional timestep and averaging time statistic on the

hydrodynamic coefficients, angle of separation, Strouhal number, mean pressure coefficient and recirculation length. The mean streamwise and crossflow velocity profile is also investigated up to 5D behind the cylinder. The study concluded that averaging time has minimal influence on the Strouhal number, drag coefficient and angle of separation. Results for angle of separation are highly dependent on the grid size around the cylinder. In addition, it is observed that recirculation length is highly sensitive to the averaging time and non-dimensional timestep. Lower averaging time underestimate the recirculation length whereas higher recirculation is observed at higher non-dimensional time step. On the basis of the results, it is observed that recirculation length is primary parameter to judge the accuracy of the results. Furthermore, the higher value of non-dimensional timestep results in U-shaped profile for mean streamwise velocity in the wake behind the cylinder which contradict the experimental results found in literature

CHAPTER 5: FLOW AROUND CYLINDER FREE TO OSCILLATE (VIV STUDY)

This chapter presents numerical investigation of Vortex-induced vibration (VIV) phenomenon for elastically mounted rigid cylinder using a computational fluid dynamics (CFD) tool. Numerical simulations have been conducted, for a fixed-cylinder case with Reynolds number (Re) = 10^4 and for a cylinder that is free to oscillate in the transverse direction and possesses a low mass-damping ratio. Previously, similar studies have been performed with 3-dimensional and comparatively expensive turbulent models. In first section of the chapter, the study has been performed using 2D and 3D Reynolds-averaged Navier-Stokes (RANS) shear–stress-transport (SST) k-ω equations. The capability and accuracy of the shear–stress-transport (SST) k-ω model are validated, and the results of this model are compared with those of detached eddy simulation, direct numerical simulation, and large eddy simulation models. All three response branches and the maximum amplitude are well captured. The 2-dimensional case with the RANS shear–stress transport k-ω model, which involves minimal computational cost, is reliable and appropriate for analyzing the characteristics of VIV. Vortex shapes mode, Strouhal number and corresponding power spectra of lift coefficient, non-dimensional amplitude, and other hydrodynamic coefficients are also discussed in detail. ANSYS FLUENT 16 tool is used for all the numerical simulations reported in this chapter.

In the second section of the chapter, numerical simulations have been conducted for fixed cylinder case at Reynold number=10^4 and for cylinder free to oscillate in cross-flow direction, at Reynold number O (104), mass-damping ratio= 0.011 and range of frequency ratio w_t=0.4 to 1.4 using Realizable k-ε (RKE) model. The results obtained from Realizable k-ε (RKE) model are compared with SST k-ω model.

In the final section of the chapter, the VIV phenomenon for elastically mounted rigid cylinder is investigated for very low mass-damping ratio for the range of reduced velocity= 2 to 16 which corresponds to Reynolds number 1700 to 14000 using RANS SST kw model.

5.1 Numerical investigation of Vortex-induced-vibration phenomenon of an elastically mounted circular cylinder using SST k-ω model.

5.1.1 Computational domain, mesh and boundary condition

The size of domain has significant impact on the behavior of the flow, both in the steady and unsteady state. Various domain sizes have been used in literature. Shao and Zhang (2006) used the domain size of 30D × 16D for flow around cylinder study using RANS code. In the numerical investigation of the hydrodynamic performance, a domain size of 8D was adopted in the transverse direction by Fang and Han (2011). Domain sizes of 25D × 20D and 27D × 9D were used by Franke and Frank (2002) and Fang and Han (2011), respectively . In the current work, a computational domain size of 45D × 20D is used (Figure 5.1). Based on previous studies, in which a smaller domain was selected, the current domain size is sufficiently large to avoid the disturbance caused by boundary conditions. Furthermore, 5% of the blockage ratio is assumed to be adequate to diminish the impact of boundary conditions on the flow field, as suggested by Zdravkovich (1990).
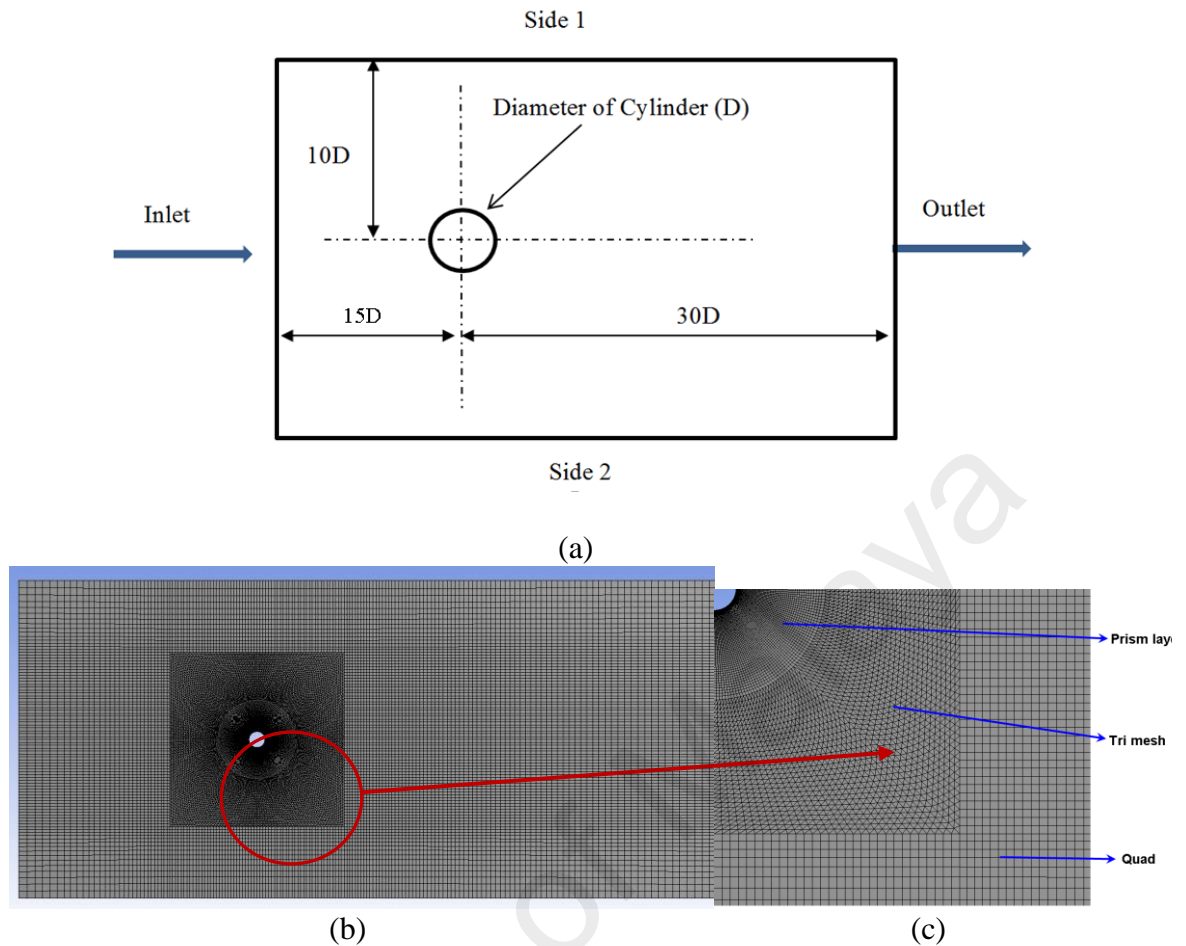
Figure 5.1: Computational domain and mesh (a) Geometry with boundary conditions (b) Mesh (c) Mesh detail section view near cylinder

In all case studies, a hybrid unstructured mesh is created in such a manner that the meshes are very fine around the wall of the cylinder and coarse at the far region. The distance between the first node and cylinder is important in extracting accurate results. According to (ANSYS Inc. ANSYS Elements manual), the y+ value, which depends on the distance between the first node and cylinder wall, should be less than or equal to unity to ensure the adequate resolution of the grid near the cylinder in simulation. In the current study, y+ = 1 is maintained in all cases with U_r ranging from 3 to 14. The grid is divided in several zones with the condition that the grid is symmetric and smooth throughout the domain to ensure stability and convergence (Figure 5.1b and Figure 5.1c). A prism is created around the cylinder having quad mesh with first node at a distance of 0.001D and growth rate of 1.05 in radial direction. Following quad mesh, a

tri mesh is created up to distance of 5D from centre of cylinder. The tri mesh has the capability to deform and re-mesh with oscillation of cylinder. Overall, the grid is smooth, symmetric and divided into several zones to avoid the numerical instability. A user defined function (UDF) code written in C language is used to allow the oscillation of cylinder and record the fluid forces with amplitude of cylinder during each iteration. In current study, dynamic mesh update method is used to allow the cylinder to oscillate in y-direction. In dynamic mesh method, diffusion based smoothing technique is utilized to update the volume mesh. In smoothing method, the number of nodes and their connectivity remain constant with the motion of zones which avoid the negative volume error/ skewness in prism layers. After prism layers, the tri mesh is created which have the ability to re-mesh and regenerate during volume mesh update. Grid independence tests are conducted, by varying the grid resolution at the cylinder wall and near-field grid, at U_r=5.84, m*=11, ζ=0.001, Re=10000 for the results of the maximum cylinder response amplitude (A_y/D) [Table 5.1]. Results of maximum cylinder response amplitude is validated against the experimental (Hover, Miller, & Triantafyllou, 1997) and numerical study (Nguyen & Nguyen, 2016). Table **5.1** presents the results for six different meshes. It is observed that T3 is able to achieve acceptable value of maximum response amplitude and further refinement in the mesh have negligible impact on the results. Therefore, T3 is finalized for all the simulations in current study.

The inlet boundary, which is on the left side of the domain, is 15 D from origin of the cylinder; the outlet boundary, which is at the right side of the cylinder, is 30 D from the origin of cylinder. A uniform velocity of 0.3149 m/s is applied at the domain inlet, which corresponds to Re=10^4 (where D = 1 m, density = 1000 kg/m^3, and viscosity = 0.03149 kg/m-s). In current study, all the important physical parameters like Re, m*, ζ and frequency ratio, are dimensionless in nature. Value of D, U, ρ, υ, k, m* and ζ are taken in such a way that the important non-dimensional parameters are similar to those

used in the experiments (Hover et al., 1997) and numerical simulations (Nguyen & Nguyen, 2016). An average static reference pressure of 0 Pa is applied at the outlet boundary. A symmetric condition is assigned to the lower and upper sides and maintained at a distance of 10 D from the cylinder center. No-slip condition is assigned to cylinder wall where velocity increases from zero at cylinder wall to the free stream velocity in the far region.

Table 5.1: Grid independence study with RANS SST k-ω model (Ur=5.84, m*=11, ζ=0.001, Re=10000)

	Cylinder wall	Near-field grid	Total elements	Max A_y/D	Experimental A_y/D (Hover et al., 1997)	Numerical A_y/D (Nguyen & Nguyen, 2016)
T1	120	7200	24220	0.8628		
T2	120	9600	28310	0.8453		
T3	240	7200	45720	0.9210		
T4	240	9600	52650	0.9216	1.003	0.9230
T5	360	7200	72640	0.9242		
T6	360	9600	77240	0.9242		

The unsteady segregated algorithm is adopted in the calculation. Pressure–velocity coupled equations are solved with the SIMPLE algorithm [explained in the (ANSYS Inc. ANSYS Elements manual)], and the implicit 1st-order scheme is utilized for unsteady terms. The 2nd-order scheme is used for k-ω transport equations and for convection terms in the momentum equations. The upwind scheme, which is of the first order, is applied to the diffusion terms.

5.1.2 Results and discussions

Numerical simulation is conducted initially for a fixed-cylinder case to test the capability of the mesh and RANS SST k-ω with 2-dimensional and 3-dimensional models. The simulation is performed at Re = 10,000. After the fixed-cylinder case, VIV

is analyzed with a single degree of freedom (DOF) at Reynolds number = 10^4 and a mass ratio of 11. All physical parameters are the same as those used in experimental (Hover et al., 1997) and numerical studies (Nguyen & Nguyen, 2016). In all case studies, y+ value equal to unity is maintained. A non-dimensional time step of 0.005 is used in all case studies.

5.1.2.1 Fixed cylinder case

Numerical simulations for flow around fixed cylinder is performed with two-dimensional and three-dimensional model at Reynold number Re=10^4 by using RANS SST k-ω. The main purpose of these case studies is to test the RANS SST k-ω model and the capability of the selected mesh to extract the results. The impact of spanwise length is reduced by assigning the periodic boundary conditions in the spanwise direction. Due to complex shape of cylinder, a variation in pressure distribution occurs on the cylinder surface due to the vortex-shedding phenomenon. The non-uniform pressure distribution along the cylinder wall results in a fluctuation in the lift forces acting on the cylinder, which leads to cross-flow oscillation and VIV. Table 5.2 presents a comparison between current results, experimental (Gopalkrishnan, 1993; Norberg, 2003) and numerical results [(Dong et al., 2006) (Nguyen & Nguyen, 2016) (Wornom et al., 2011)] for the fixed-cylinder case. Drag coefficient is defined as $C_d = 2F_d / (\rho U^2 A)$, where F_d is the drag force in stream-wise direction integrated over cylinder surface and ρ, U and A are density of fluid, Inlet velocity and projected frontal area of the cylinder, respectively. Lift coefficient is defined as $C_l = 2F_l / (\rho U^2 A)$, where F_l is the lift force on the cylinder surface in the cross-flow direction. Calculations are based on Finite volume method (FVM). The drag and lift is calculated by integrating components (cells) values around the cylinder. The root-mean-square value of C_l is calculated from the time history data of C_l (Figure 5.2a). The time histories of C_d, C_l, and corresponding St

obtained from the current simulations are shown in Figure 5.2. The C_d and St values are well computed by the RANS SST k-ω model. However, a deficiency exists in computing the root-mean-square C_l. The difference in the results is due to the impact of the aspect ratio, as investigated by Norberg (2003) and Nguyen and Nguyen (2016) in their experimental and numerical studies, respectively. The study suggested a high aspect ratio to obtain a low value of root-mean-square C_l. Figure 5.2b shows the plot of power spectrum density of lift force coefficient history against St. Strouhal frequency computed using the SST k-ω model agrees well with the experimental results.

(a)   (b)
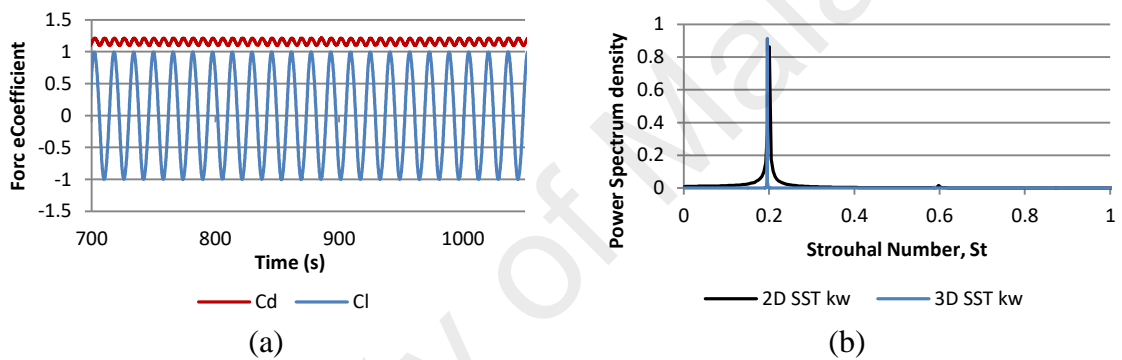
Figure 5.2: Force coefficients and corresponding b) Strouhal number for flow past fixed cylinder at Re=10000

Figure 5.3 presents the plot of the mean pressure coefficient along the cylinder wall. In the numerical simulation, the pressure coefficient is calculated as $C_p = 2P/(\rho U^2)$, where P, ρ, and U are the pressure, density, and uniform inlet velocity of fluid, respectively. Comparison of results depict a slight variation at the flow separation region (i.e., 70° to 80°), which shows the deficiency of the SST k-ω model in extracting the results in this specific region. Figure 5.4 shows the detailed instantaneous wake structure behind the cylinder at maximum and minimum C_l. Alternative vortex shedding from the upper and lower regions of the cylinder is observed at maximum and minimum C_l, respectively, which results in periodic forces on the cylinder. These periodic forces are assumed to be responsible for the VIV phenomenon.
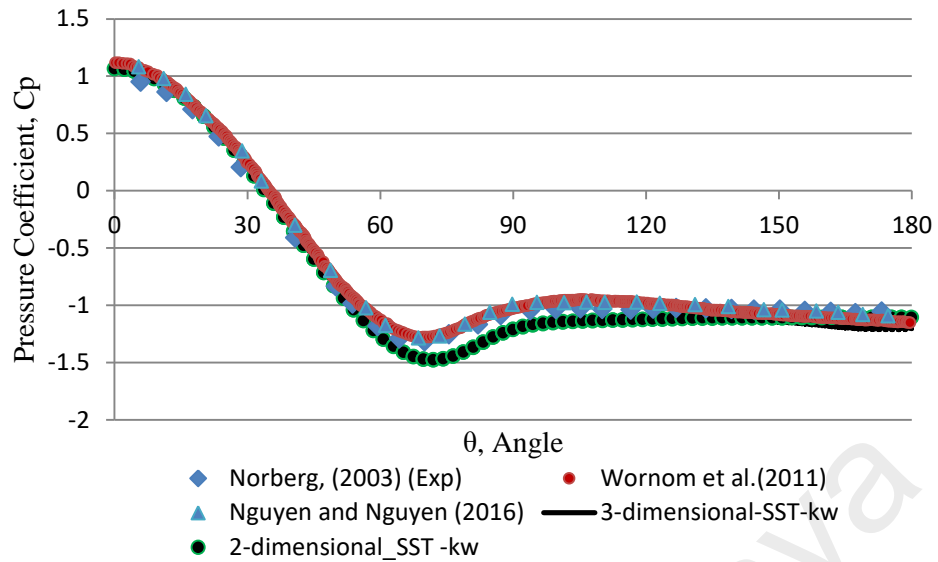
Figure 5.3: Comparison of mean pressure coefficient distribution at cylinder surface for fixed cylinder at Re=10000
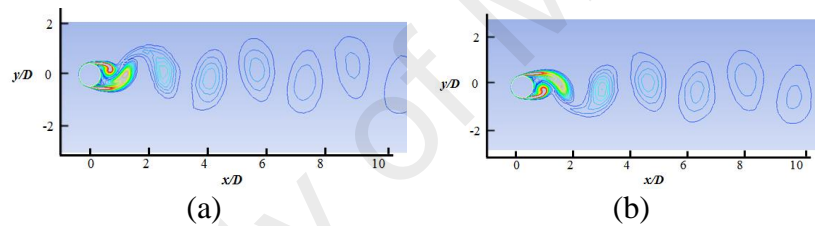

(a)   (b)

Figure 5.4: Instantaneous wake strutures at (a)maximum lift coefficeint and (b) minimum lift coefficient at Reynolds number Re=10,000

This comparison of results indicates that 2-dimensional SST k-ω, which is less expensive than DNS (Dong et al., 2006), LES (Wornom et al., 2011), and DES (Nguyen & Nguyen, 2016), can extract acceptable results at Re = 10,000. With this conclusion, numerical study is extended to analyze the VIV phenomenon in which cylinder is allow to oscillate in cross flow direction at Re = 10^4 and mass ratio m* = 11.

Table 5.2: Comparison of C_d, C_l, and St at Re = 10,000 with numerical and experimental results available in literature

	$C_{d, mean}$	$C_{l.rms}$	St
Experimental (Norberg, 2003)	-	0.25-0.46	0.202
Experimental (Gopalkrishnan, 1993)	1.19	-	0.193
LES(Wornom et al., 2011)	1.22	0.476	0.20
DES (Nguyen & Nguyen, 2016)	1.133	0.262	0.2005
DNS (Dong et al., 2006)	1.143	0.448	0.203
2-dimensional- SST k-ω	1.150	0.701	0.201
3-dimensional - SST k-ω	1.210	0.646	0.203

5.1.2.2 VIV analysis for smooth circular cylinder free to oscillate in the cross-flow direction (1 DOF)

After the numerical investigation of flow around a fixed cylinder, the study is extended to the case study in which cylinder is allow to oscillate in the y- direction, as shown in Figure 5.5. Cylinder oscillation is constrained in the y-direction by a spring-damper system with spring constant K and damping coefficient c. Analysis is performed at Re = 10^4, damping ζ = 0.001, and mass ratio m* = 11. These parameters were also used in the experimental studies (Hover et al., 1997) and numerical simulation (Nguyen & Nguyen, 2016). Numerical simulations are performed with U_r ranging from 3 to 14. The change in U_r is obtained by changing the frequency ratio w_t while maintaining the velocity. (Hover et al., 1997) indicated that cylinder vibration is characterized by frequency ratio w_t (ratio of damped natural frequency to fixed-cylinder vortex-shedding frequency).
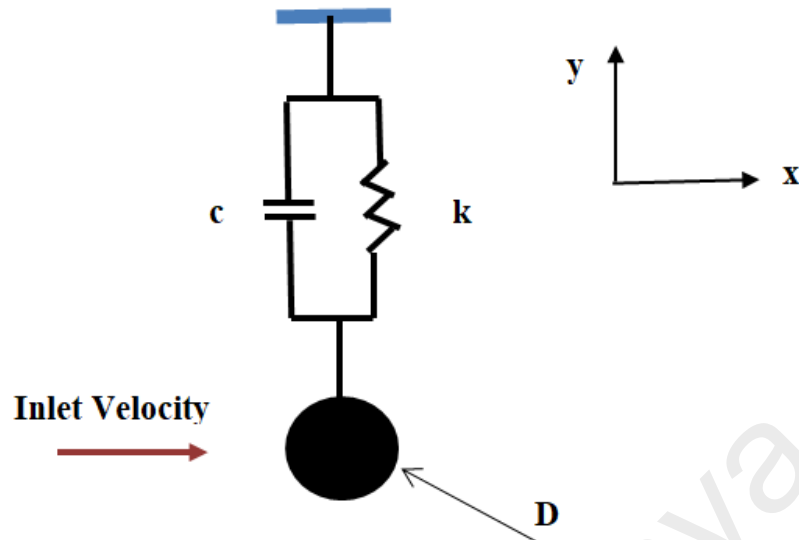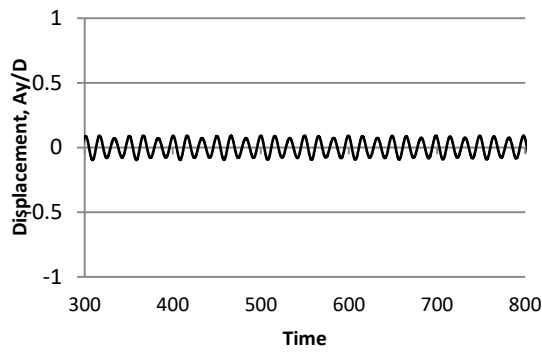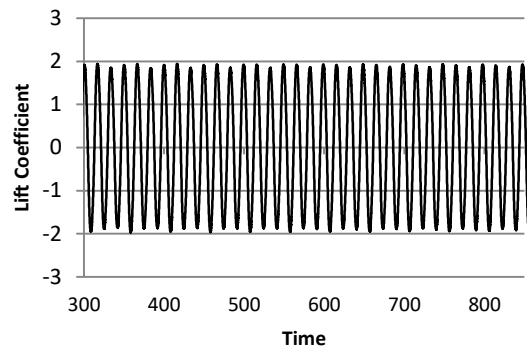
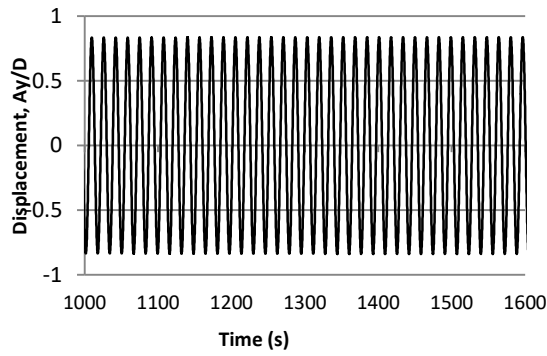**Figure 5.5: Flow around cylinder with 1DOF**

The time histories of non-dimensional cylinder amplitude and C_l at various frequency ratios are shown in Figure 5.6. The corresponding power spectra for cylinder amplitude and C_l are shown in Figure 5.7. When the natural frequency of the structure approaches the vortex-shedding frequency, the lock-in phenomenon or synchronization occurs, which in turn causes the cylinder oscillation to reach the maximum amplitude. This behavior is observed in Figure 5.6, in which the highest amplitude is found at frequency ratios wt = 1.0 and 0.8. A low value of cylinder response is also observed at wt = 1.4 and 0.5. Furthermore, single frequency in the cylinder displacement amplitude is observed, and the lift force coefficients have multiple peaks (Figure 5.7). Figure 5.8 compares the time history of the instantaneous C_d and C_l at various frequency ratios. It is observed that there is weak correlation between instantaneous C_d and C_l, since the simulations is carried out using 2-dimensional model. In addition to the highest amplitude and multiple peaks in the power spectra of C_l, high values of drag forces are also found in the upper branch, as shown in Figure 5.8b and Figure 5.8c. Out of the lock-

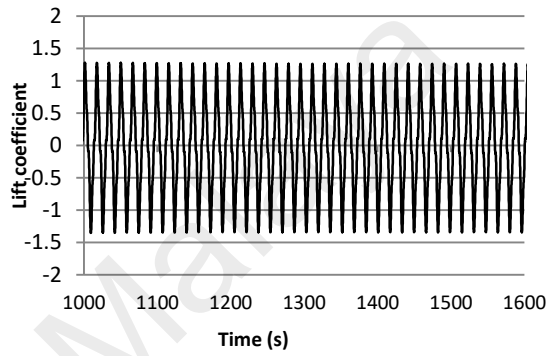**Figure 5.6: Time history of non-dimensional amplitude and lift coefficient at various ratio, (m*=11, ζ=0.001, Re=10000)**
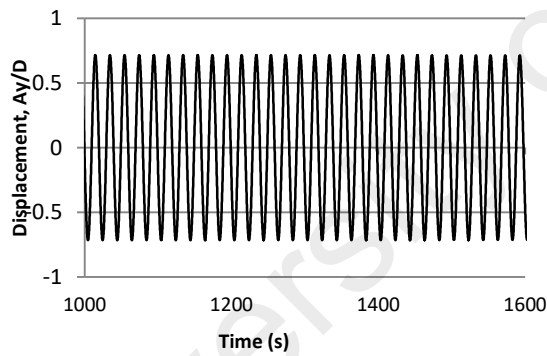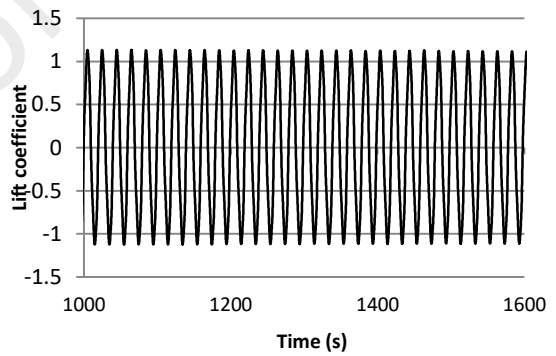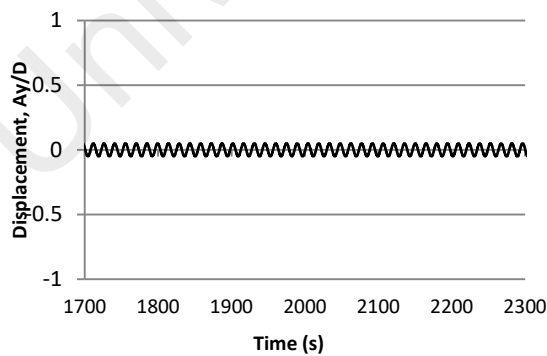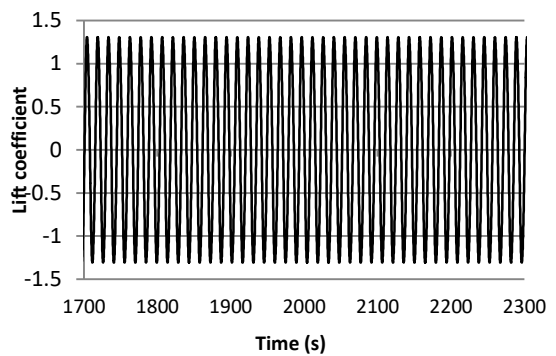
(a) wt 1.4

(b) wt=1.4

(c) wt 1.0
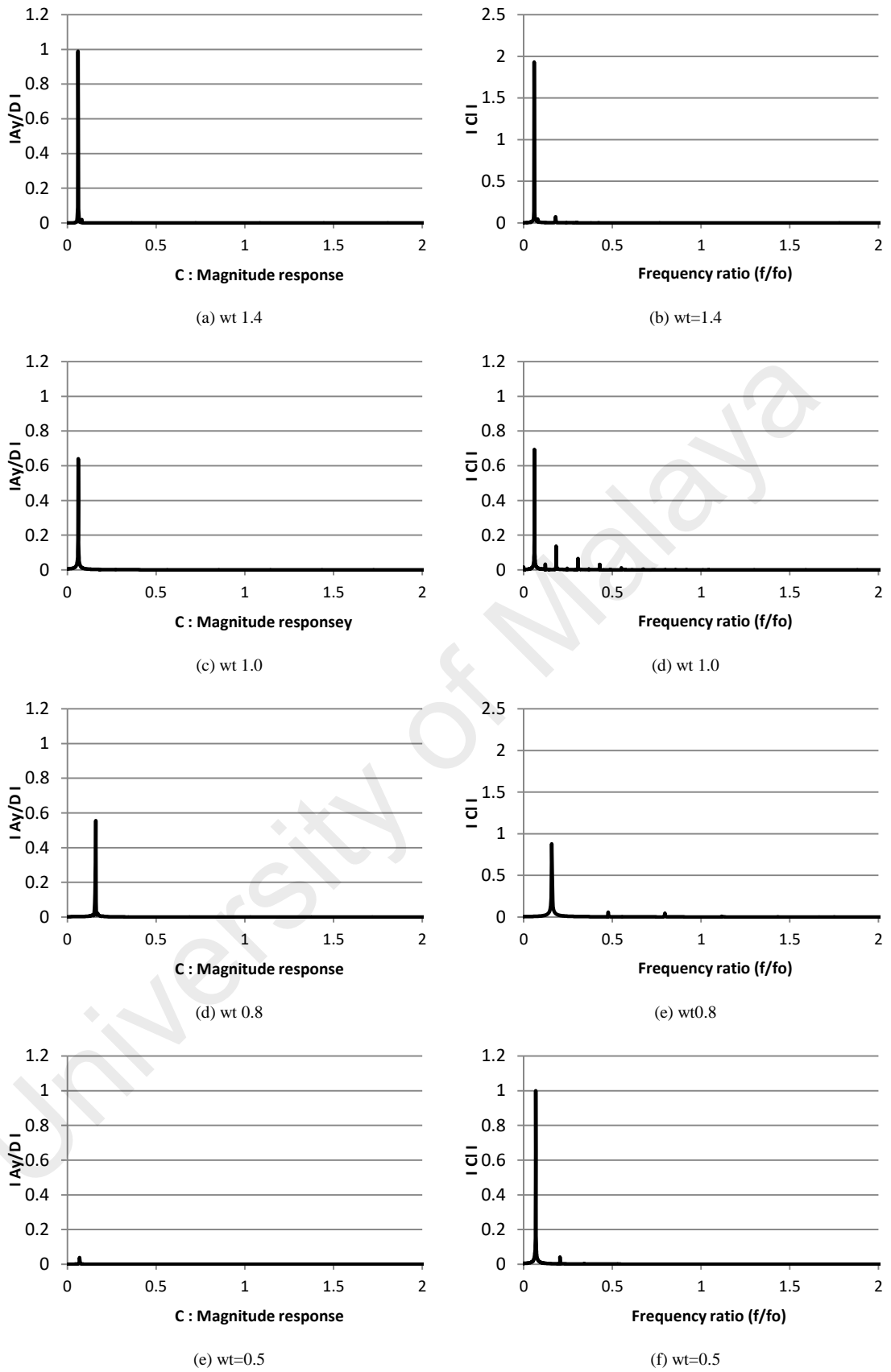
(d) wt 1.0

(d) wt 0.8

(e) wt0.8

(e) wt=0.5

(f) wt=0.5

Figure 5.7: Power spectra non-dimensional amplitude and lift coefficient at Re=10000 (m*=11, ζ=0.001)

-in region, comparatively small values of drag forces are observed. This behavior of drag forces has also been reported by Bishop and Hassan (1964).
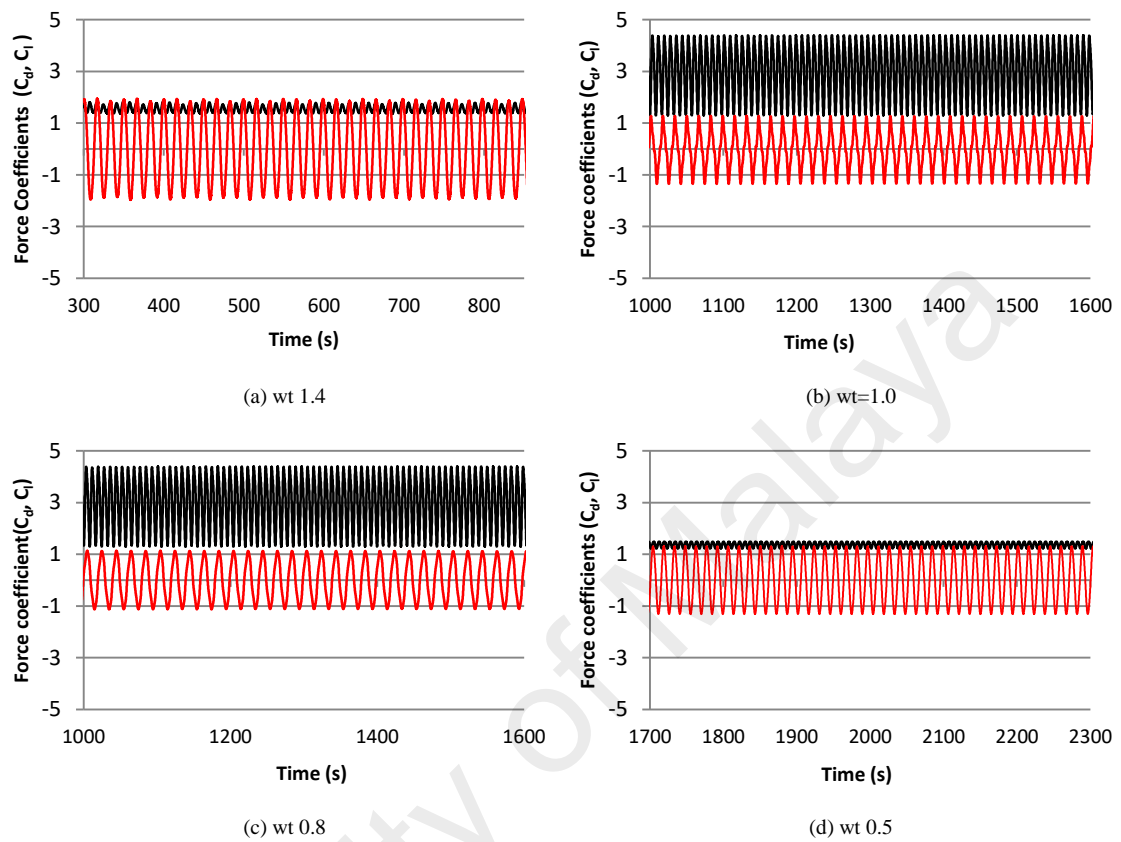

(a) wt 1.4

(b) wt=1.0

(c) wt 0.8

(d) wt 0.5

Figure 5.8: Time history of C_d (black-line) and C_l (red-line) at various frequency ratio, (m*=11, ζ=0.001, Re=10000)

The non-dimensional amplitude of the cylinder computed in the current study is compared with that of a 3-dimensional DES study (Nguyen & Nguyen, 2016) and experimental results (Hover et al., 1997), as shown in Figure 5.9. Cylinder response is extracted from Figure 5.6, which shows the time history of cylinder transverse displacement. In all these cases, $Re = 10^4$ is kept constant, and the change in Re is obtained by changing the frequency ratio. The cylinder response is categorized in three distinct branches according to classification of Khalak and Williamson (1997a) i.e. "initial branch", "upper branch" and "lower branch. All the three types of response are well captured by SST k-ω model as shown in Figure 5.9. Similar to the 3-dimensional

DES approach, the SST k-ω model also reveals the transition between the initial and upper branches at $U_r = 4.7$. The maximum amplitude response of $Ay/D = 0.92$ is observed in the upper branch at $U_r = 5.84$ (wt = 0.9), which agrees well with the 3-dimensional DES approach. However, comparatively early transition at $U_r = 8.1$ ($w_t = 0.65$) is observed between the upper and lower branches. Comparison of the results shows good agreement among the results of the current SST k-ω model, DES (Nguyen & Nguyen, 2016), and experimental results (Hover et al., 1997).
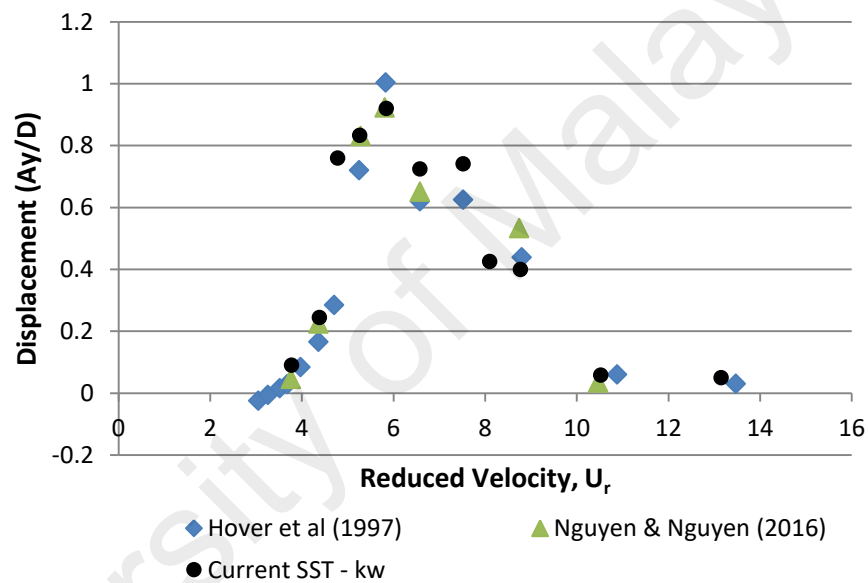

Figure 5.9: Comparison of cylinder response amplitude using SST k-ω model with experimental data and numerical DES data (m*=11, ζ=0.001, Re=10000)

The details of the wake structures behind the cylinder are shown in Figure 5.10 to Figure 5.13, for reduced velocity Ur=3.78, Ur=5.84, Ur=7.52 and Ur=8.77, respectively. The 2P and 2S vortex modes observed in the current study agree well with those in the DES study (Nguyen & Nguyen, 2016). Jauvtis and Williamson (2004) , Jauvtis and Williamson (2004),and Williamson and Roshko (1988) stated that the 2S vortex mode indicates that each half cycle results in single vortex shedding into a wake, whereas the 2P vortex mode indicates that each half cycle results in a pair of vortex shedding. As concluded in a previous study (Jauvtis & Williamson, 2004), the vortex

mode behind the cylinder is affected by the fluctuation in cylinder transverse displacement. At U_r = 3.78, the 2S vortex mode is observed, as shown in Figure 5.10. It is observed that cylinder response is small (Ay/D<0.3) at the initial branch. At peak amplitude or in lock-in region (Figure 5.11 and Figure 5.12), pairs of vortices shedding are observed which is resemblance with 2P vortex mode as reported in earlier studies ((Jauvtis & Williamson, 2004; Williamson & Roshko, 1988).
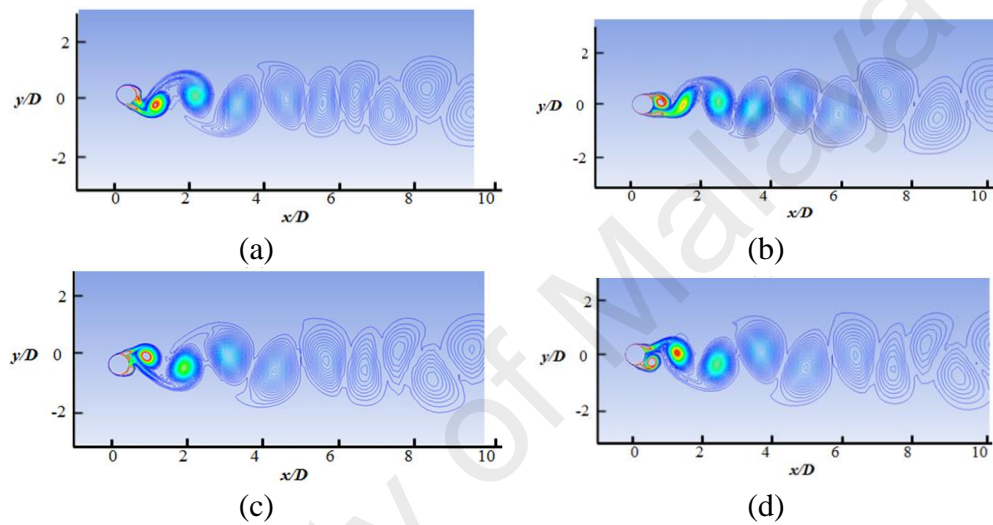
Figure 5.10: Instantaneous Vorticity contour at Ur=3.78 (m*=11, ζ=0.001, Re=10000)
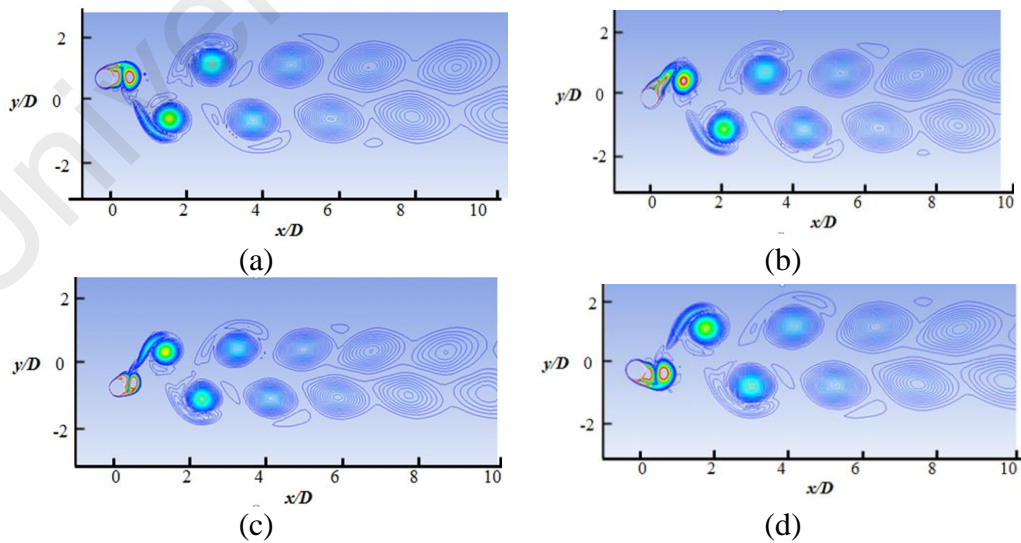
Figure 5.11: Instantaneous Vorticity contour at Ur=5.84 (m*=11, ζ=0.001, Re=10000)

The higher displacement response in upper branch is clearly depicted at Ur=5.84 and Ur=7.52 in Figure 5.11and Figure 5.12, respectively. At Ur=8. 77 (Figure 5.13), which comes under the lower branch, the second vortex is very weak in position and sheds rapidly. The wake pattern and vortex modes justify the 2P shapes in the lock-in region.

(a)

(b)

(c)

(d)

Figure 5.12: Instantaneous Vorticity contour at Ur=7.52 (m*=11, ζ=0.001, Re=10000)

(a)

(b)

(c)

(d)

Figure 5.13: Instantaneous Vorticity contour at Ur=8.77 (m*=11, ζ=0.001, Re=10000)

5.1.3 Summary

Numerical simulations are conducted to test the performance of the RANS model for a fixed-cylinder case and for a cylinder that is free to oscillate in the transvers direction at Re = 10^4, mass ratio m* = 11, and ζ = 0.001. This stu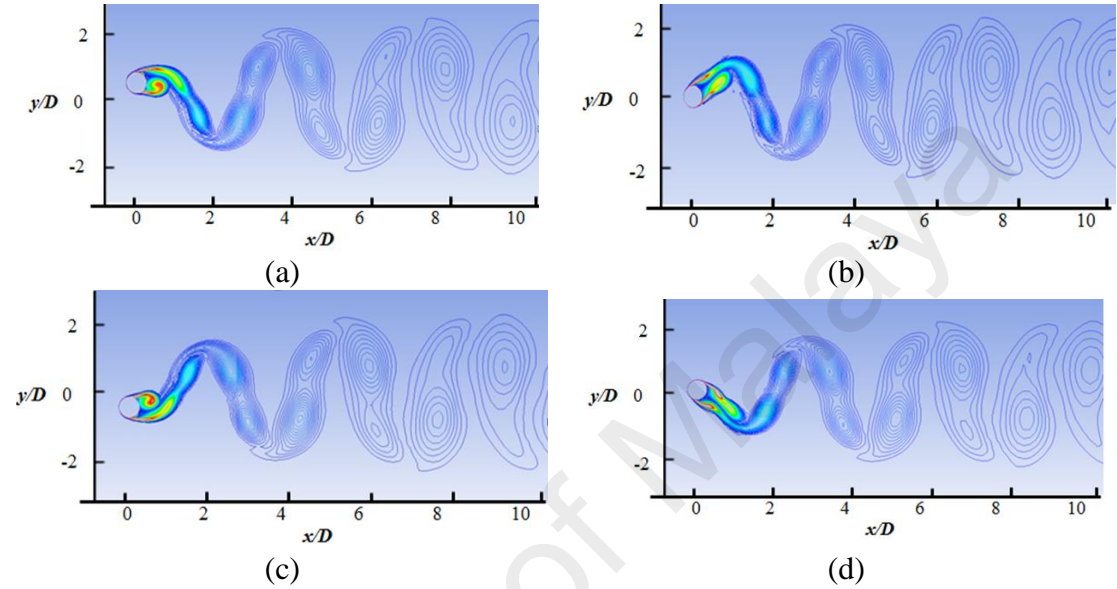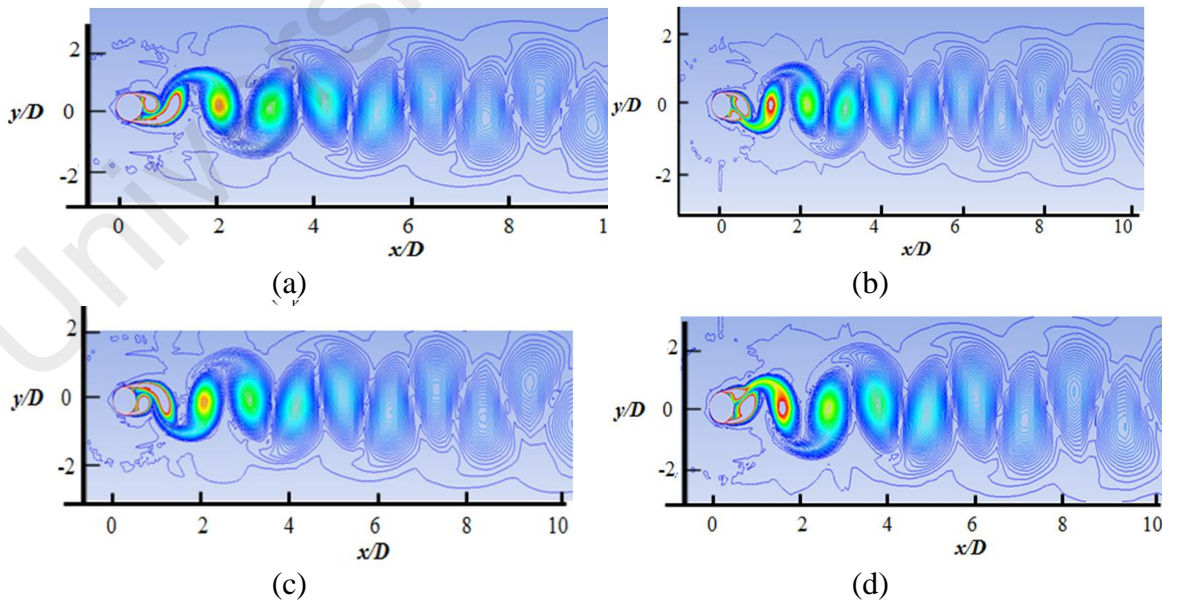dy focuses on the capability of the RANS model to analyze the flow around cylinder at Re = 10^4, mass ratio m* = 11, and ζ = 0.001. For fixed cylinder case at Re = 10,000, the performances of the mesh and RANS model are tested through 2-dimensional and 3-dimensional numerical simulations. The results are validated with 3-dimensional numerical DES, LES, and experimental results. The fixed-cylinder case reveals that the 2-dimesnsional RANS SST k-ω turbulent model can produce acceptable results. However, a high value of C_1 is obtained due to the low aspect ratio. To investigate the VIV phenomenon, numerical simulations are performed for an elastically mounted rigid cylinder that is free to oscillate in the cross flow direction at U_r = 3 to 14 with constant Re (Re = 10^4) and mass ratio (m* = 11). The 2-dimensional SST- k-ω results agree well with those of the 3-dimensional DES and experimental studies. The maximum amplitude, A_y/D = 0.92, is observed at the upper branch, which agrees well with the 3- dimensional DES results. Compared with the DES study and experimental results, the current study observed earlier transition from upper to lower branch. The RANS SST k-ω model confirms the formation of different vortex modes at U_r = 3 to 14. The agreement with experimental and 3-dimensional computationally expensive DES and LES results builds confidence in using the 2-dimensional RANS SST k-ω turbulent model and paves the way for highly complex analyses.

5.2 Numerical investigation of Vortex-induced-vibration of an elastically mounted circular cylinder: Comparison between SST k-ω and Realizable k-ε (RKE) model results

In this section, numerical analysis of VIV phenomenon has been carried out using Realizable k-ε (RKE) model and results are compared with SST k-ω model. All the parameters used in the study are same as used in previous section. Main focus of this work is to compare the accuracy and capability of RANS SST k-ω and Realizable k-ε (RKE) turbulent model in study of flow around fixed cylinder at Reynold number=10^4 and for cylinder free to oscillate in cross-flow direction, at Reynold number O (10^4), mass-damping ratio= 0.011 and range of frequency ratio wt=0.4 to 1.4. Standard k-ω model have several limitations like sensitivity to free-stream boundary for free shear flows. SST k-ω model is improved version of standard k-ω model in which cross-diffusion term is included in the ω equation by Menter (1994). In addition the prediction feature is enhanced by including an improved definition of eddy-viscosity for boundary layer flows. Similarly, RKE model (Shih et al. 1995) is an improved form of standard k-ε model which have alternative formulation for turbulent viscosity. Also, the equation for the dissipation rate is derived from exact equation for the transport of mean-square vorticity fluctuation. RKE model is better than k-ε standard model in a way that characteristics of turbulent flow are consistent with the Reynolds stresses. According to (ANSYS Inc. ANSYS Elements manual), the RKE model have capability to perform comparatively better in a case where the flow in complex in nature but still there is need to investigate the model performance along curvature, vortex shedding and rotation. Further details about SST k-ω and RKE model is explained by Menter (1994) and Shih et al. (1995), respectively.

The computational domain, mesh pattern and boundary conditions used in the study is same as used in section 5.1. In case of Realizable k-ε (RKE) model, enhanced wall

treatment (EWT) option is utilized which makes the simulation independent of y+ wall treatment(ANSYS Inc. ANSYS Elements manual). The results extracted from simulation are compared with the experimental results (Hover et al., 1997) and 3-dimensional numerical study (Nguyen & Nguyen, 2016). All simulations have been carried out using ANSYS FLUENT 16 tool.

5.2.1 Results and discussions

Numerical tests are first carried out for fixed cylinder case followed by the case studies in which cylinder is free to oscillate in cross-flow direction. The physical parameters used in current study are same as those used by Hover et al. (1997) in experimental testing and Nguyen and Nguyen (2016) in numerical testing using DES turbulent model, except the 2-D simplification.

5.2.1.1 Fixed cylinder case

Numerical study for flow around fixed cylinder has been carried out at Re=10^4 using 2D and 3D RANS (SST k-ω and RKE) model. Results extracted from the study have been compared with numerical and experimental results available in literature. In case of three dimensional model, span-wise length of $4D_o$ (where D_o is diameter of cylinder) is used in which top and bottom face were assigned as periodic boundary condition. Figure 5.14 shows the plot of mean pressure coefficient obtained from present studies (SST k-ω and RKE results), experimental study (Norberg, 2003) and numerical study ((Wornom et al., 2011) & (Nguyen & Nguyen, 2016)). RKE (2D and 3D) results agreed with the experimental results before the flow separation point region. After the flow separation region, RKE model unable to capture the acceptable results. In case of SST k-ω, the mean pressure coefficient graph agreed well with the numerical and experimental results, except the slight differences at flow separation region. Figure 5.15 illustrate the comparison of drag, lift and Strouhal number taken from current studies,

experimental results from Norberg (2003) and numerical results from Wornom et al. (2011) and Nguyen and Nguyen (2016). Figure 5.15 presents time history of force coefficient i.e. drag and lift coefficient, and power spectral density versus Strouhal number (St=f D_o /U) where f is fluctuation force of lift force. From Figure 5.15b, Strouhal number St=0.20 computed for $2D_o$ and $3D_o$ case of SST k-ω agreed well with the literature references while a higher value of Strouhal number is obtained in case of RKE model. From these comparisons, it is observed that SST k-ω turbulence model, which is computationally less expensive than DNS (Dong et al., 2006), DES (Nguyen & Nguyen, 2016) and LES (Wornom et al., 2011), have the capability to capture the results up to good extent.
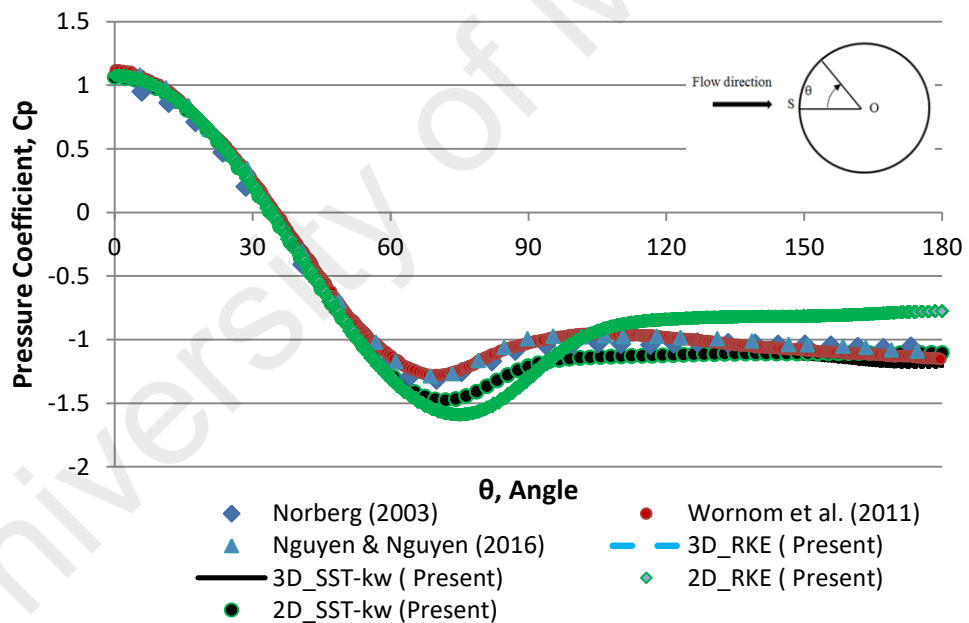

Figure 5.14: Mean pressure coefficient distribution around cylinder surface, where θ is angle starting from stagnation point (S) in clock-ωise direction

Table 5.3: Comparison of drag, lift and Strouhal number at Re=10000 with numerical and experimental results available in literature

	Cd	$C_{l.rms}$	St
LES (Wornom et al., 2011)	1.22	0.476	0.2
DES (Nguyen & Nguyen, 2016)	1.133	0.262	0.2005
DNS (Dong et al., 2006)	1.143	0.448	0.203
2D- SST k-ω (Present)	1.149	0.700	0.200
3D- SST k-ω(Present)	1.211	0.645	0.202
2D- RKE (Present)	0.910	0.325	0.220
3D- RKE (Present)	0.880	0.261	0.230

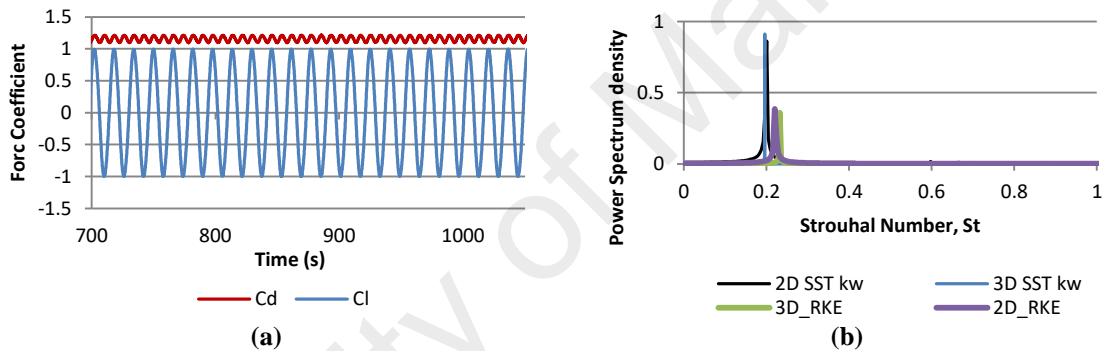(a)   (b)

Figure 5.15: Time histories for (a) Force coefficients and corresponding (b) Strouhal number for flow past fixed cylinder at Re=10000

5.2.1.2 Vortex Induced vibration of smooth circular cylinder free to oscillate in cross-flow direction (1-Degree of freedom)

All the case studies are performed at Re=10000, mass ratio, m*=11 and ζ=0.001. To study the VIV phenomenon, the cylinder is allowed to move in y-direction as shown in Figure 5.5. The cylinder motion is constrained by spring-damper system with spring constant k and damping coefficient c. Numerical analyses are conducted for the varying range of reduced velocity (2-13). The variation in reduced velocity is achieved by altering the value of w_t while the velocity is same in all the case studies. Due to constant velocity, single mesh with y+=1 is used for all the cases. Enhanced wall treatment

option is utilized for RKE testing to make the simulation independent of y+ value (ANSYS Inc. ANSYS Elements manual). According to Hover et al. (1997), vibration of cylinder is characterized by ratio of damped natural frequency to the fixed cylinder vortex shedding frequency ($w_t = w_n/w_s$).
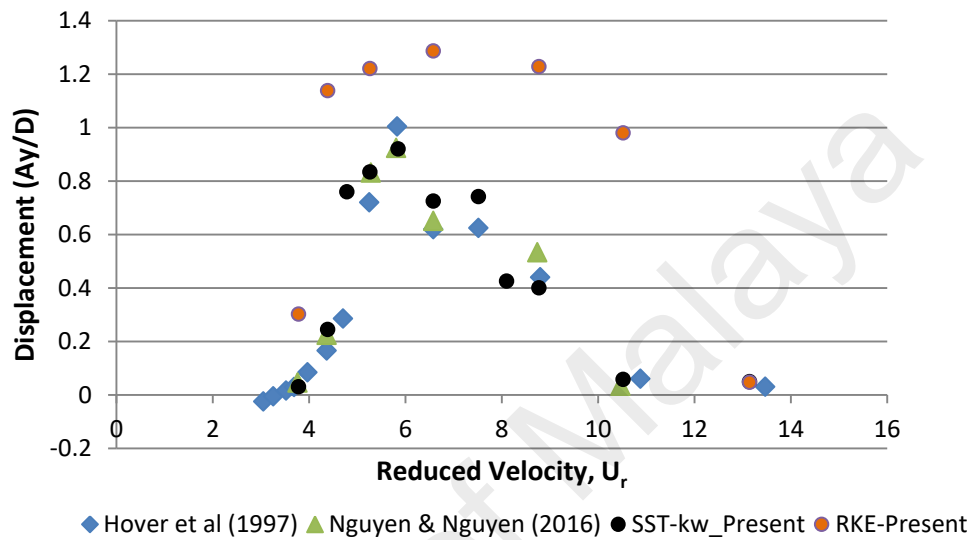

Figure 5.16: Cylinder amplitude response comparison using SST k-ω and RKE model, Hover experimental data and numerical DES data (m*=11, ζ=0.001, Re=10000)

Cylinder response amplitude (Ay/ D_o) obtained from current study (SST k-ω & RKE) is compared with experimental and numerical results, as shown in Figure 5.16. The normalized amplitude data is obtained from displacement time history graphs [Figure 5.17 and Figure **5.18**] at different frequency ratio ranging 1.4 to 0.4 whereas the Reynold number is kept constant i.e. Re=10000. It is observed that SST k-ω turbulent model capture all the three responses branches i.e. Initial, Upper and lower branch. Like 3-Dimensional DES approach, SST k-ω model also show the transition between initial and upper branch at reduced velocity Ur=4.7. Maximum amplitude response Ay/D=0.92 is observed at reduced velocity Ur=5.84 (wt=0.9), which agreed well with the 3-dimensional DES approach. Transition between upper and lower branch is

observed at reduced velocity Ur=8.1 (w_t=0.65) which is slightly earlier than DES (Nguyen & Nguyen, 2016) case (w_t=0.7). RKE model behaved differently compared to SST k-ω in term of capturing the mode of vortex and maximum amplitude. The maximum displacement (Ay/D>=1.29) attained by RKE model, during the 'lock-in' phenomenon, is higher than the DES (Nguyen & Nguyen, 2016) and experimental results (Hover et al., 1997) but deficiency in capturing the initial and lower branch is observed. The transition between upper and lower is very delayed and attained at Ur=10.5 which results in broad range of 'lock-in' region. Also, comparatively high value of normalized amplitude (Ay/D=0.302) is obtained at initial branch.

The wake behind structure captured by SST-k-ω at different instant step of reduced velocity Ur=3.78, Ur=5.84 and Ur=8.77 are shown in Figure 5.19, Figure 5.20 and Figure 5.21, respectively. Figure 5.20 shows pair of vortices resembling the 2P vortex mode while 2S vortex is observed in Figure 5.19.

(a) wt 1.4

(b) wt=1.2

(c) wt 1.0

(d) wt 0.9

(d) wt 0.8

(e) wt0.7

(e) wt=0.6

(f) wt=0.5
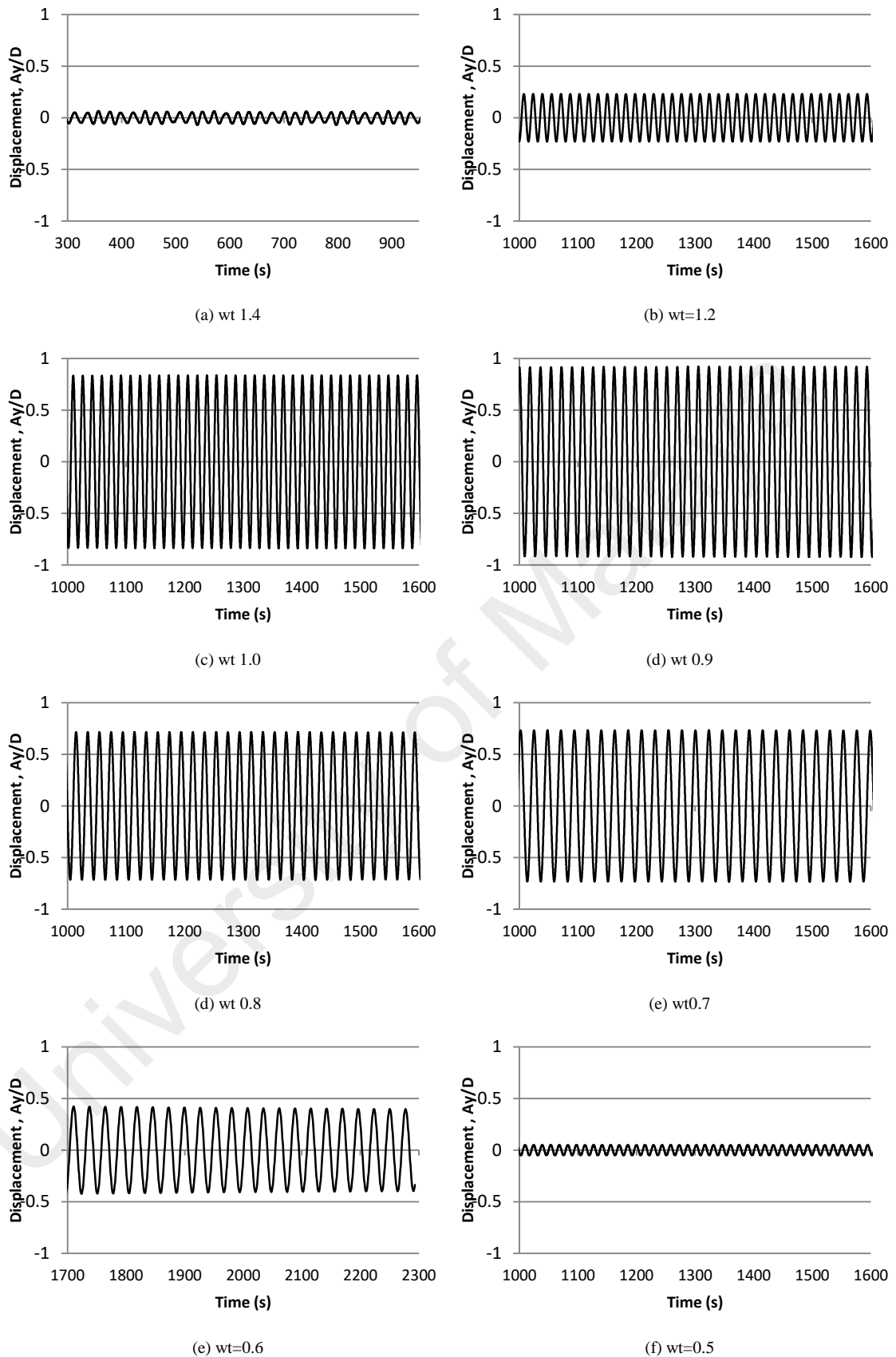
Figure 5.17: Displacement time history at different frequency ratio, (m*=11, ζ=0.001, Re=10000) using SST-k-ω model
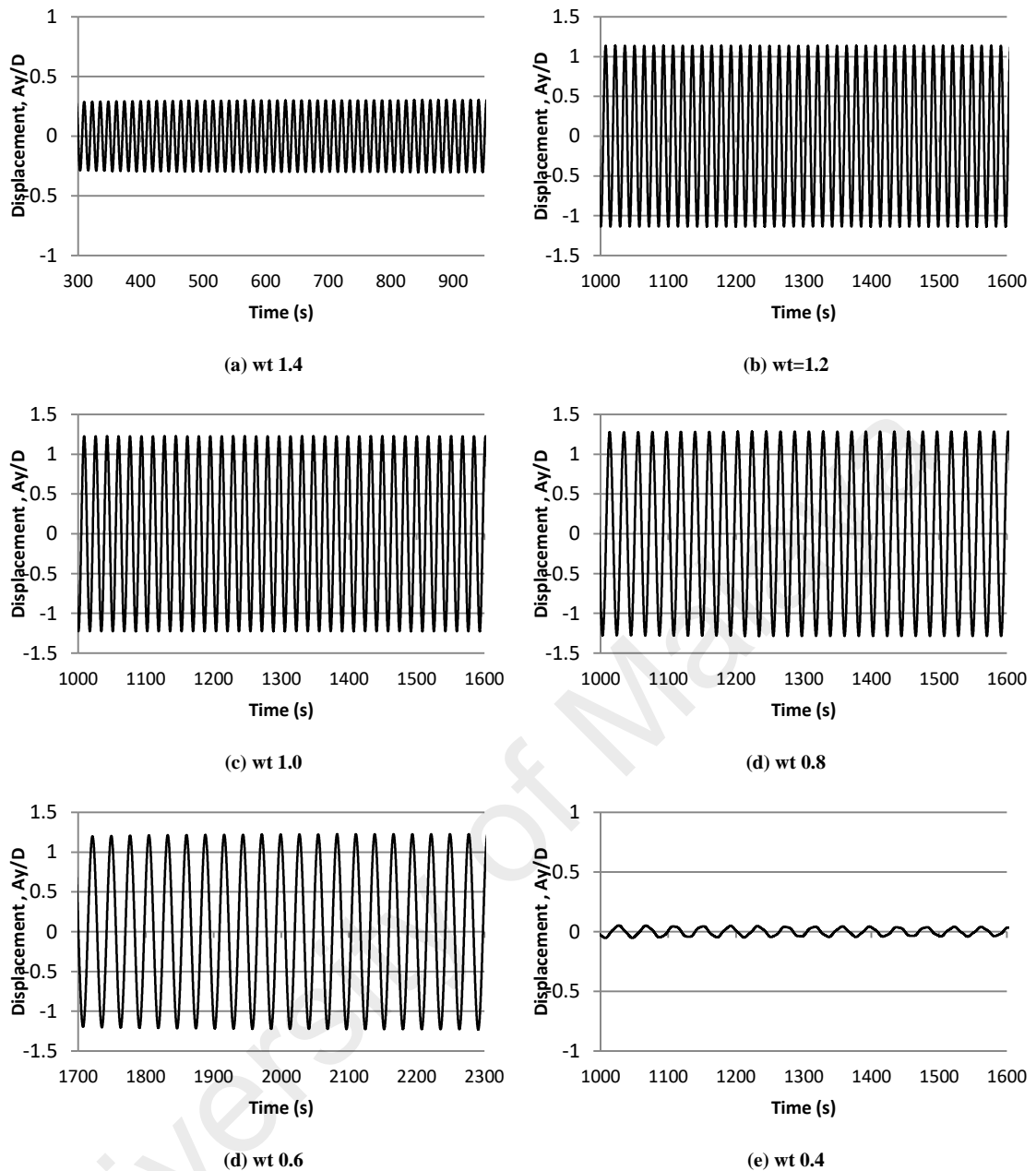
Figure 5.18: Displacement time history at different frequency ratio, (m*=11, ζ=0.001, Re=10000) using RKE model

At Ur=8.77 (Figure 5.21), 2P vortex mode is observed with the difference from Figure 5.19 in a sense that second vortex is in very weak position. The wake behind structures obtained using RKE model are shown in Figure 5.22,Figure 5.23 and Figure 5.24 at reduced velocity Ur=3.78, Ur=5.26 and Ur=8.77, respectively. Like SST-k-ω cases, pairs of vortices are also observed using RKE in the lock-in region. RKE model failed to capture 2S vortex shedding mode at initial branch.
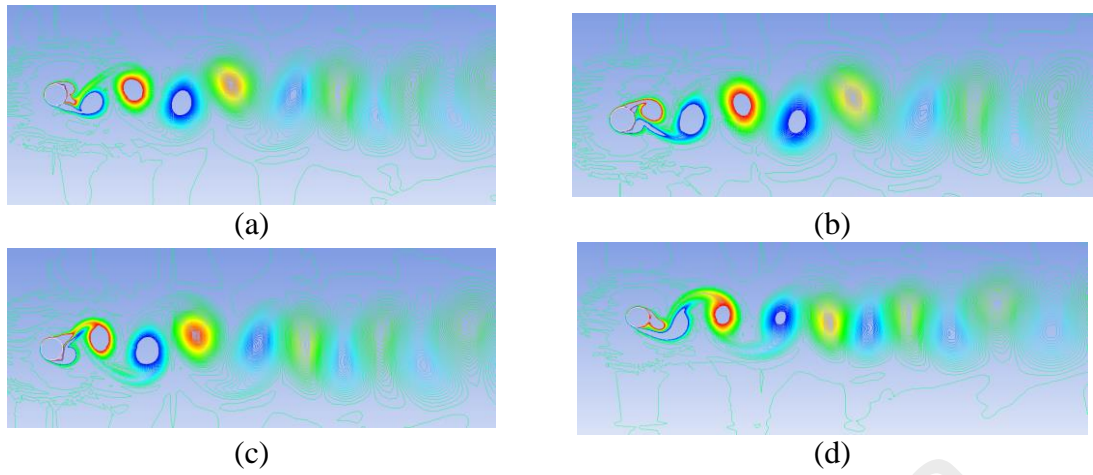
Figure 5.19: Vorticity contour at Ur=3.78 (m*=11, ζ=0.001, Re=10000)
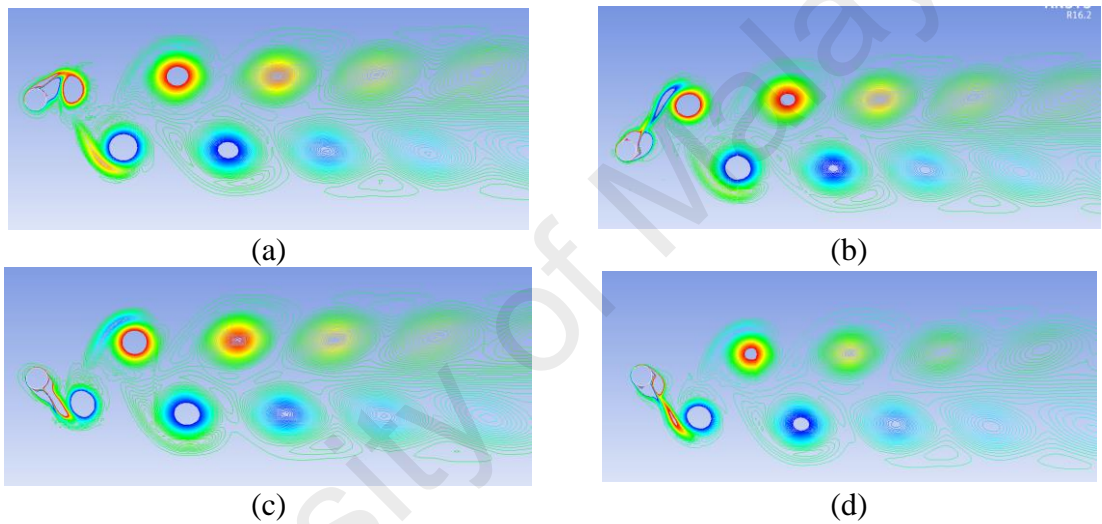
Figure 5.20: Vorticity contour at Ur=5.84 (m*=11, ζ=0.001, Re=10000)
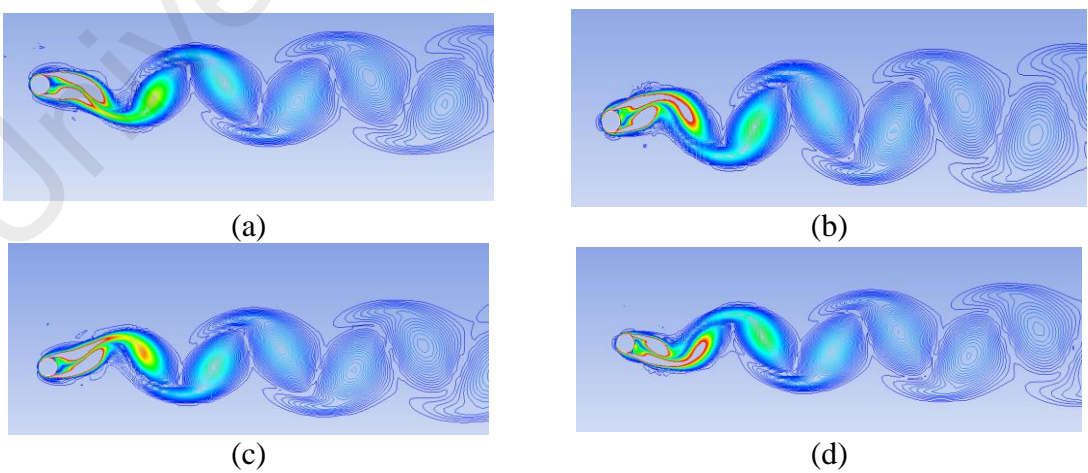
Figure 5.21: Vorticity contour at Ur=8.77 (m*=11, ζ=0.001, Re=10000)

126

(a)　　　　　　　　　　(b)

(c)　　　　　　　　　　(d)
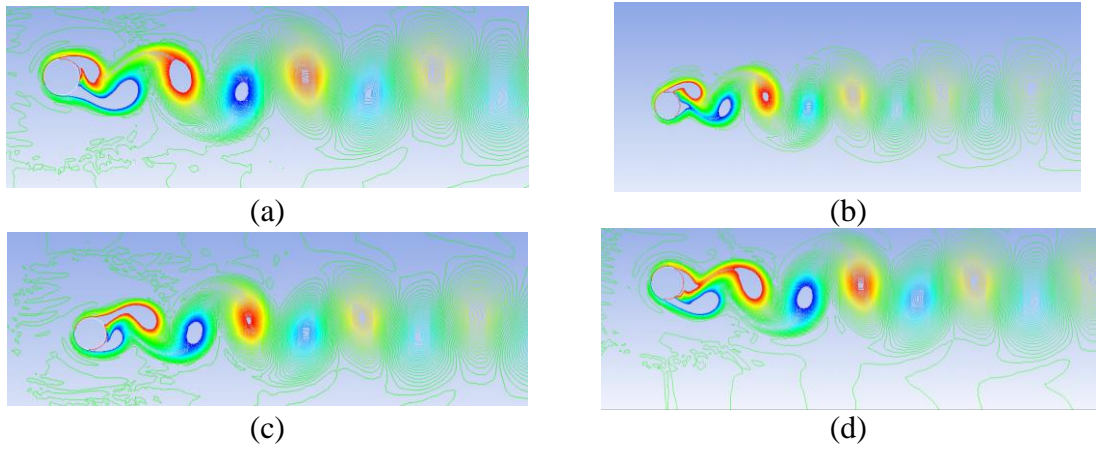
Figure 5.22: Vorticity contour at Ur 3.78 using RKE

(a)　　　　　　　　　　(b)

(c)　　　　　　　　　　(d)
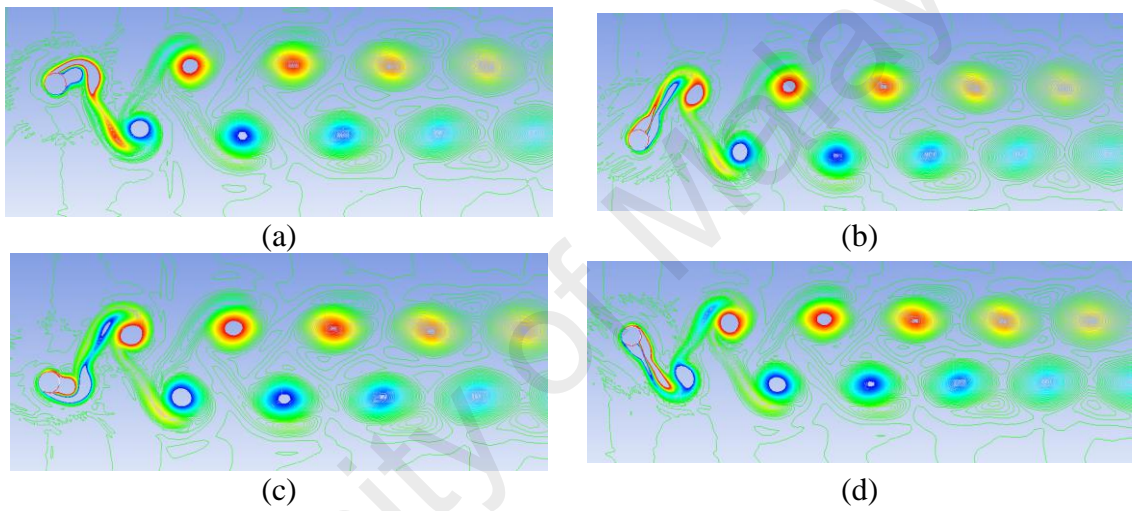
Figure 5.23: Vorticity contour at Ur= 5.26 using RKE
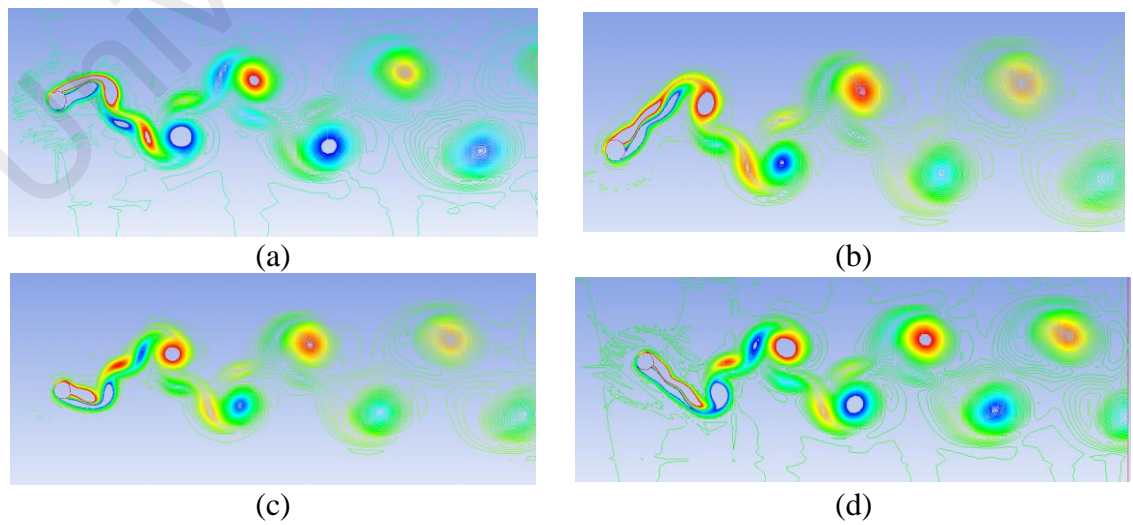
(a)　　　　　　　　　　(b)

(c)　　　　　　　　　　(d)

Figure 5.24: Vorticity contours at Ur=8.77 using RKE

5.2.2 Summary

The study mainly focused on the capability of RANS turbulent model, which is comparatively less expensive, to predict the vortex mode and amplitude response of elastically mounted rigid cylinder at high Reynold number Re=10000. Numerical investigation is carried out using 2-D and 3-D model and results are compared with experimental and 3-Dimensional DES test results available in literature. It is found in the fixed cylinder case study that 2-dimensional RANS SST k-ω turbulent model well captured the forces and responses at high Reynold number. 2D and 3D RKE model show deficiency in computing the acceptable results after the flow separation occurs. 2D RANS SST k-ω and RKE model are also tested for VIV study of circular cylinder which is free to oscillate in cross-flow direction, at Re=10^4. SST k-ω agreed well with 3-dimensional DES study and experimental studies available in literature whereas RKE model was unable to capture the three modes of branches. Maximum amplitude captured by RKE model is higher than experimental and three dimensional DES results whereas SST k-ω model results agreed well with the experimental and 3D DES results. Also the broad range of lock-in region is observed during RKE study. RANS SST k-ω model confirmed the formation of different vortex mode in the range of reduced velocity Ur=3 to Ur=13. The agreement, with experimental and 3-dimensional computationally expensive DES and LES results, built the confidence in 2-dimensional RANS SST k-ω turbulent model study and open the way for more complex analysis.

5.3 VIV study of an elastically mounted cylinder having low mass-damping ratio by using the RANS model

This section addresses the VIV phenomenon of an elastically mounted rigid cylinder oscillating freely in the cross-flow direction and subjected to a low mass damping ratio. Two-dimensional RANS equations are simulated for this purpose. The study is carried out with a mass damping ratio of 0.0013 in the range of reduced velocity of 2 to 16,

which corresponds to the *Re* ranging from 1700 to 14000. Similar previous studies were performed numerically but were limited in achieving the maximum cylinder response. In the current study, comparatively high value of maximum amplitude of a cylinder is computed. However, delays in transition from 'upper branch' to 'lower branch' are recorded. In addition to maximum amplitude, other hydrodynamic coefficients are discussed. The results extracted from the current simulations are compared with those of previous experimental and numerical studies.

5.3.1 Computational mesh and boundary conditions

Figure 5.25 presents the computational domain used in the current study. Computational domain size has significant impact on the flow behavior and need to be large enough to avoid the disturbance due to boundaries. In current work, domain size of 20D X 45D is used which is assumed to be larger enough to avoid disturbance due to boundary. Furthermore, the domain size is comparatively larger than the domain size used in previous studies (Franke & Frank, 2002), (Fang & Han, 2011). In addition, Zdravkovich (1990) suggested 5% of blockage ratio to diminish the boundaries effect which is fulfilled in the current study. . Inlet is located at 15D toward the left hand side, while outlet is at distance of 25D right hand side of the cylinder. An average static reference pressure of 0 Pa is applied at the outlet boundary. Top and bottom sides, which are assigned with symmetry condition, are at a distance of 10D from the cylinder surface. No-slip effects are assigned on the cylinder wall surface where velocity increases from zero at cylinder surface to free-stream velocity away from surface.

Mesh distribution plays significant role in predicting the complex flow dynamics of flow around cylinder problems. Multi-block hybrid unstructured mesh is used here, with the condition that mesh is very fine near the cylinder and comparatively coarser in the far-region, as shown in Figure 5.25(a) - (c).

The block is divided into number of subdomain in such a way that output mesh is smooth, symmetric and continuous throughout domain to ensure the stability, accuracy and convergence of the solution. The region near the cylinder wall is made of prim layers having quad elements. Prism layers, which covered approximately 3.5Do around the cylinder, are followed by tri elements. After the tri-elements region, all the remain domain is meshed with quad elements. During all the case studies, first node is kept at a distance which ensure the y+ value equal to or less than unity. Grids sensitivity tests are performed by varying number of elements on the cylinder surface. Finally, 240 nodes at surface of cylinder and total of 45230 elements are chosen, based on the mesh independence test. In order to maintain Courant-Friedrichs Lewy (CFL) condition value equal to or less than unity for RANS SST kw model, a non-dimensional timestep is set to 0.0001 in all case studies. The VIV study involved oscillation of cylinder which result in deformation and remeshing of the grid. In current study, the prism layers around cylinder oscillate along with cylinder. The tri-mesh has the capability to deform and re-mesh with oscillation of the cylinder. To avoid the negative volume error and instability in simulation, the whole domain is made continues and smooth by making the grid symmetric with constant growth rate of 1.05 throughout.

In current study, dynamic mesh update method is used to allow the cylinder to oscillate in y-direction. In dynamic mesh method, diffusion based smoothing technique is utilized to update the volume mesh. In smoothing method, the number of nodes and their connectivity remain constant with the motion of zones which avoid the negative volume error/ skewness in prism layers. After prism layers, the tri mesh is created which have the ability to re-mesh and regenerate during volume mesh update.

Figure 5.26 shows the schematic representation of flow around a circular which is free to oscillate in cross flow direction. The elastic system has 'c' as a damping constant and 'k' as a spring constant in y-direction.
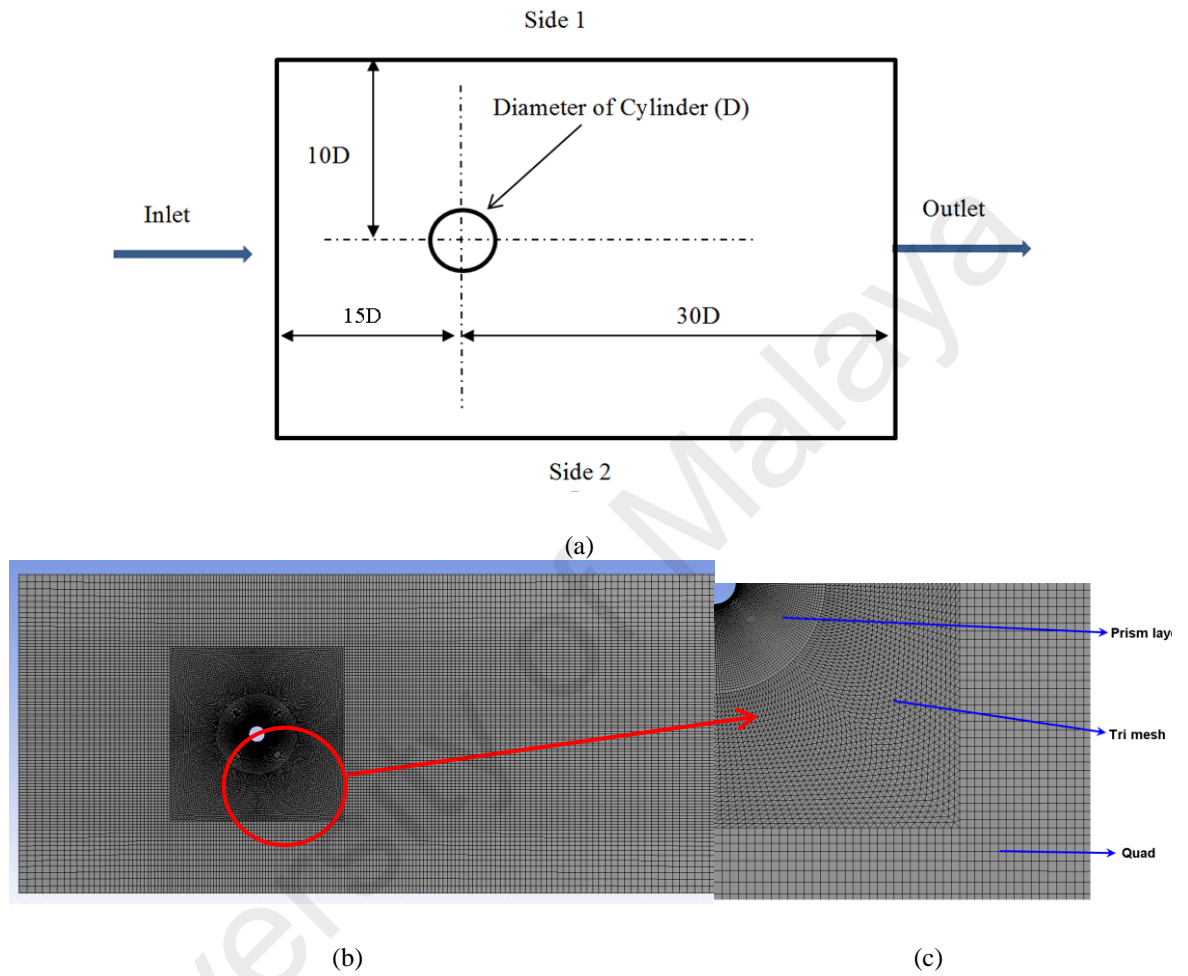

(a)

(b)   (c)

Figure 5.25: (a) Computational domain and (b)-(c) mesh details
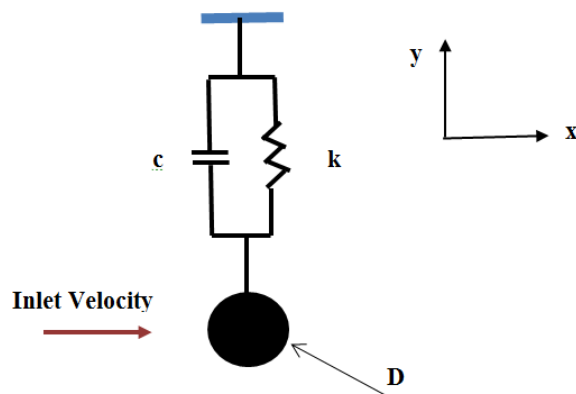

**Figure 5.26: Cylinder free to oscillate in cross-flow direction**

5.3.2 Results and discussions

Numerical analyses are performed for flow around rigid cylinder with 1-DOF, as show in Figure 5.26. As depicted in the Figure 5.26., the cylinder is free to vibrate in the crossflow-direction by a spring damper system. Analysis are executed for range of Reynolds number Re=1700 to 14000 which correspond to Ur=2 to 16. The variation in reduced velocity is obtained by altering the uniform inlet velocity. All physical parameters used in the current study are same as used by Khalak and Williamson (1996), Li et al. (2014) and Pan et al. (2007).

Figure 5.27 shows the time history of cylinder response (Ay/D) and corresponding instantaneous force coefficients at different reduced velocity. Cd is coefficient of drag force calculated over cylinder surface in streamwise direction whereas Cl is the coefficient of lift force calculated over cylinder surface in cross-flow direction. Drag and lift forces are computed on the bases of finite volume method. Reduced velocity is defined as uniform inlet velocity normalized by diameter and natural frequency of cylinder. Figure 5.31 examines cylinder response as a function of reduced velocity together with the experimental and numerical results. Cylinder response (Ay/D) is extracted from the time history of displacement. All the three branches, namely initial, upper and lower, are observed in the study as depicted from Figure 5.31. Initial branch is observed in the range of reduced velocity Ur=2-3, followed by upper branch in the range of reduced velocity Ur 5-9. The lock-in phenomenon is observed during the upper range at which the cylinder natural frequency is equal or close to vortex shedding frequency.

It is clearly depicted that at region of upper branch, high value of displacement is observed. In current study, maximum non dimensional cylinder response value Ay/D=0.86 is observed at reduced velocity Ur=7.5 which is comparatively better than

the numerical results of Li et al. (2014) and Pan et al. (2007). Pan et al. (2007) and Li et al. (2014) found the maximum cylinder response Ay/D=0.70 and Ay/D=0.747, respectively, which is quite smaller than experimental value Ay/D=1. The higher value of cylinder response also validated the occurrence of lock-in phenomenon in upper branch. After upper branch, the transition to the lower branch is observed at reduced velocity Ur=11 where cylinder response reduced to Ay/D=0.2-0.1 which agreed well with the other experimental and numerical results. From Figure 5.27, weak correlation is observed between Cd and Cl due to two dimensionality of the model. Furthermore, there is correlation between instantaneous drag coefficient and maximum amplitude. Higher mean drag coefficient values are observed at upper branch where the maximum non-dimensional amplitude is observed as shown is Figure 5.27(d) – (e), whereas at out of the 'lock-in' region, the smaller mean value of drag coefficient is observed. Figure 5.28, Figure 5.29 and Figure 5.30 present instantaneous vorticity mode at Ur=2 (initial branch), Ur=7. 5 (upper branch) and Ur= 11 (transition from upper to lower branch). 2S vortex mode, in which each half cycle results in single vortex shedding into a wake, is found at Ur=2 and 2P vortex mode, in which each half cycle results in a pair of vortex shedding, is found at upper branch at Ur=7.5. At Ur=11, 2S vortex mode is observed as shown in Figure 5.30.
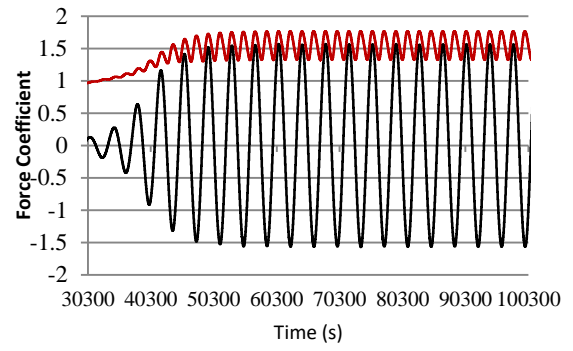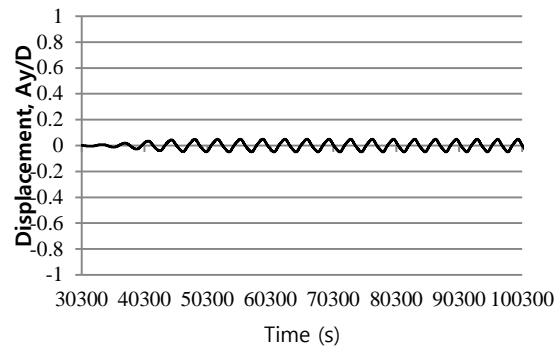
(a) Ur=2

(b) Ur=2

(c) Ur=5

(d) Ur=5

(d) Ur 7.5

(e) Ur 7.5

(e) Ur 11
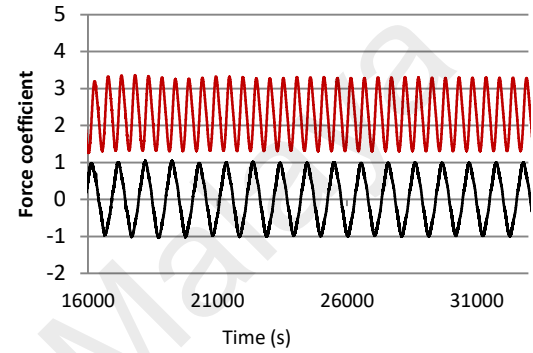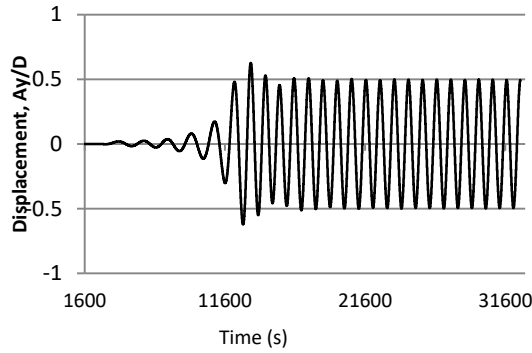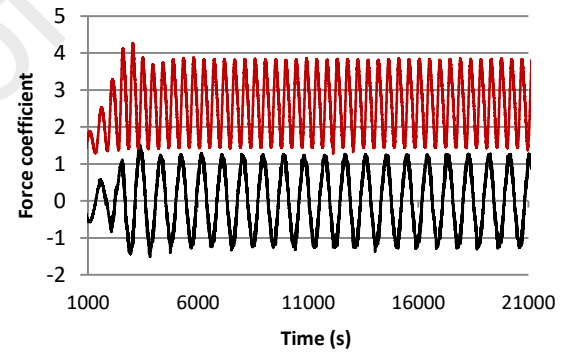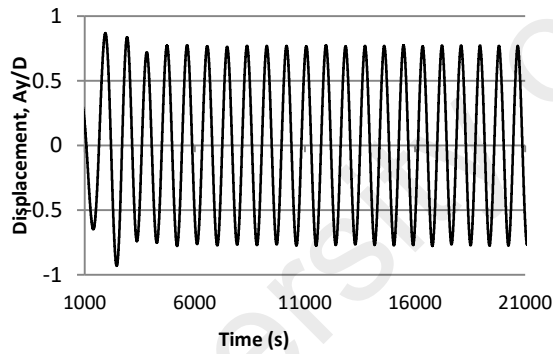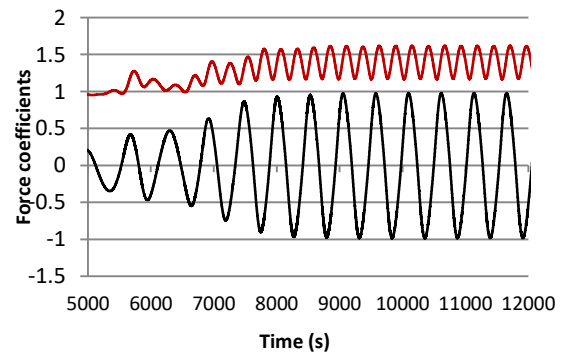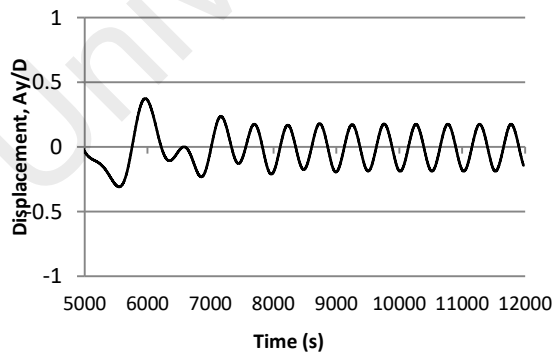
(f) Ur 11

Figure 5.27: Time history of cylinder response (Ay/D) and force coefficients (drag force-red color and lift force-black color) at different reduced velocity

134
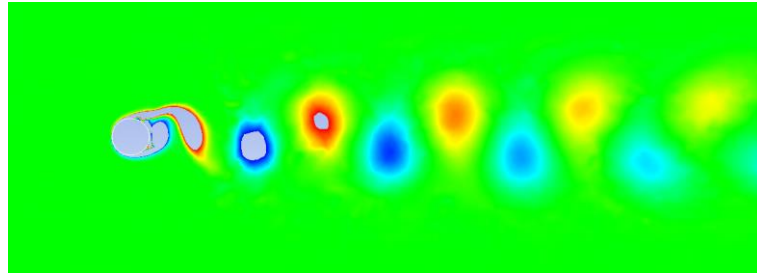
Figure 5.28: Instantaneous vorticity contour at Ur=2, Re=1700 and m.ζ=0.0013
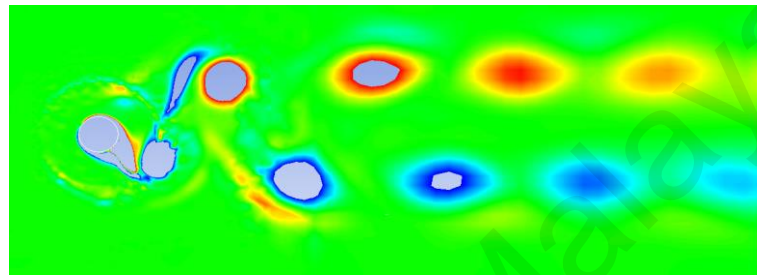
Figure 5.29: Instantaneous vorticity contour at Ur=7.5, Re=6250 and m.ζ=0.0013
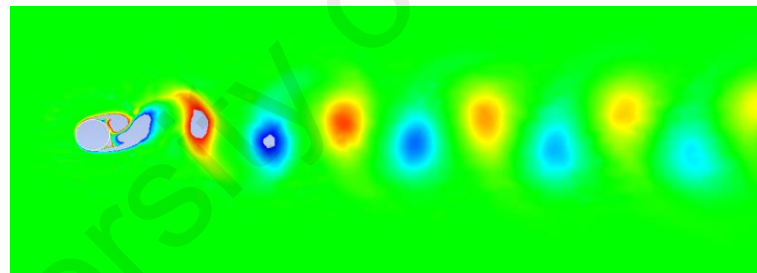
Figure 5.30: Instantaneous vorticity contour at Ur=11, Re=9166 and m.ζ=0.0013
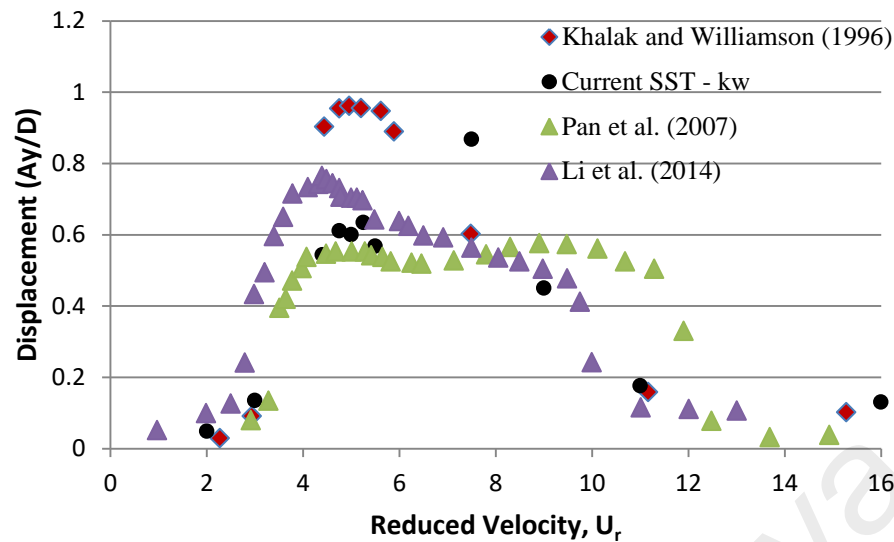
Figure 5.31: Cylinder response (Ay/D) at range of reduced velocity (Ur)

5.3.3 Summary

The current work presents the numerical investigation into the VIV phenomenon of an elastically mounted rigid cylinder with a low mass ratio by using the RANS SST kω model. The numerical results are compared with those of existing experimental and numerical studies. All three branches of the VIV phenomenon are observed in the study. Small values of cylinder response and drag forces are observed at the initial branch, whereas the maximum values of cylinder response are observed at the upper branch. The maximum cylinder amplitude observed in the current study is comparatively superior to the existing results. However, higher cylinder response occurs in the later phase of the upper branch. The lock-in phenomenon with a high value of cylinder amplitude and drag forces is observed at a reduced velocity of 4–9, which presents a wider range compared with those in other studies. We also emphasise the need to investigate the impact of blockage ratio and prism mesh distribution to achieve good quality results.

CHAPTER 6: SUMMARY AND FUTURE WORK RECOMMENDATIONS

6.1 Conclusion

Flow around a cylinder at *Re* = 3900 is a 3D problem, and the spanwise domain exerts a significant impact on flow characteristics. 2D numerical study cannot accurately capture turbulence behaviour. 2D analysis results in over-predicted values of force coefficients, underestimated Strouhal numbers, short recirculation length and delays in the angle of separation. Mesh resolution in the spanwise direction is an important parameter affecting the accuracy and quality of results. Coarse mesh density in the spanwise direction results in a short recirculation length. In addition, turbulence in the wake behind a cylinder cannot be well captured. In the case of flow around a fixed cylinder, aspect ratio is an important parameter in experimental studies, whereas in numerical studies, the effect of aspect ratio can be reduced by assigning the periodic boundary condition to the end surface. With periodic boundary conditions at the end surface, the increase in spanwise domain exerts a negligible impact on the results, thus keeping the mesh density constant. The results of the force coefficients and angle of separation are highly dependent on the grid size at the cylinder surface and near-field grid. With constant mesh density in the spanwise domain, the coarse mesh at the cylinder surface and near-field grid results in overestimated values of drag forces and delays in capturing the angle of separation. Recirculation length is the most significant parameter to assess the accuracy and quality of results.

In the temporal discretisation study, a high Courant–Friedrichs–Lewy (CFL) condition results in over-predicted values of recirculation length and captures the U-shape profile for mean streamwise velocity in the wake behind a cylinder. Such outcome contradicts the experimental results found in the literature. In addition, turbulence statistics sampled at low vortex shedding cycles result in non-converged solutions. The study recommends fulfilling the CFL condition and capturing the results

after 50 vortex shedding cycles. Drag coefficient and Strouhal number are less sensitive, whereas recirculation length appears to be highly dependent on the average time statistics and non-dimensional time step.

The 2D RANS SST kω turbulent model can capture all three response branches, and the maximum amplitude in the VIV study of flow around an elastically mounted rigid cylinder with a low mass damping ratio at $Re = 10^4$. However, the values of lift forces are low due to the small aspect ratio, and the mean pressure coefficient at the flow separation region is low due to the adverse pressure gradient. The 2S and 2P vortex modes are effectively captured by the 2D RANS SST kω turbulent model for cylinders with low mass damping ratios at $Re = 10^4$.

The RKE model cannot capture all three response branches during the VIV phenomenon at a high Reynolds number and low mass damping ratio. In addition, the broad range of the 'lock-in' region because of delays in capturing the transition from the upper to the lower branches demonstrates the deficiency of the RKE model.

In the numerical investigation of the VIV phenomenon, the RANS SST kω model can compute high values of maximum amplitude in problems involving low mass damping ratios. However, delays in capturing the transition between the upper and lower branches result in a broad lock-in regime. The blockage ratio and mesh distribution around the field need to be addressed to capture accurate results.

6.2 Future Recommendation

In the current study, the flow around a fixed cylinder at $Re = 3900$ was investigated numerically using a large eddy simulation code. The impact of spanwise domain, mesh resolution in the spanwise direction and near-field grid, non-dimensional time step and time statistic average on the accuracy of statistical quantities, Strouhal number, mean

pressure coefficient, angle of separation, recirculation length and other hydrodynamic coefficients was also investigated. The capability, reliability and accuracy of different RANS models in the investigation of the VIV phenomenon were determined. The current study may be used to improve the understanding of problems involving flow around cylinders. However, further improvements can be made to extend the current research in the future.

- The current study mainly focuses on flow around a cylinder in the subcritical regime. Hence, the scope needs to be extended to the upper-critical and transition regimes. Despite the advancement in computational technologies, the DNS model is still unlikely to be applied in the near future. An advanced numerical model must be developed to predict and analyse the detailed insights into flow around cylinders.

- The LES model provides excellent insight into the problem of flow around a cylinder but entails high computational cost at high Reynolds number. The RANS model is less expensive than the LES model but is prone to several limitations and deficiencies, particularly at adverse pressure gradients. Therefore, the hybrid of the LES and RANS models (also known as the detached eddy simulation [DES] model) may produce comparatively good results. The capability and accuracy of the DES model in predicting flow characteristics and the VIV phenomenon need to be investigated in future studies.

- The current study mainly focuses on cross flow oscillation (one degree of freedom), but the VIV of a circular cylinder is a two-degree-of-freedom (in the streamwise and crossflow directions) problem. The study can be extended to multiple degrees of freedom with the RANS model.

- Although the 2D numerical simulation to investigate the VIV phenomenon entails high computation cost, the study needs to be extended to a 3D numerical analysis to gain a clear understanding of the forces on a cylinder, cylinder oscillation and vortex modes.

- Most studies available in the literature explored the VIV phenomenon for elastically mounted rigid cylinders. In practical engineering, slender structures, such as pipes, spar hulls (with roughness), mooring lines and risers, are flexible in nature. Owing to rapid advancement in computational technologies, the numerical investigation can now be extended to flow around flexible cylinders.

- The impact of surface roughness on the VIV phenomenon for elastically mounted rigid cylinders should be investigated under conditions of high Reynolds numbers by using a RANS equation.

- The sensitivity of the VIV phenomenon with respect to changes in Reynolds numbers should be studied numerically for different regimes.

- Most existing studies focused on the VIV phenomenon associated with a circular geometry. The VIV phenomenon for other common cross section shapes, such as D-shape and triangular shape needs to be addressed.

REFERENCES

Achenbach, E. (1968). Distribution of local pressure and skin friction around a circular cylinder in cross-flow up to Re= 5× 10 6. *Journal of Fluid Mechanics, 34*(04), 625-639.

Achenbach, E., & Heinecke, E. (1981). On vortex shedding from smooth and rough cylinders in the range of Reynolds numbers 6× 10 3 to 5× 10 6. *Journal of Fluid Mechanics, 109*, 239-251.

Afgan, I., Kahil, Y., Benhamadouche, S., & Sagaut, P. (2011). Large eddy simulation of the flow around single and two side-by-side cylinders at subcritical Reynolds numbers. *Physics of Fluids (1994-present), 23*(7), 075101.

Amann, O. (1941). T. von K arm an, and GB Woodruff. *The Failure of the Tacoma Narrows Bridge. Federal Works Agency*.

ANSYS Inc. ANSYS Elements manual, t. e., 2016.

Batchelor, G. (1970). K. 1967 an introduction to fluid dynamics: Cambridge University Press.

Bearman, P. (2011). Circular cylinder wakes and vortex-induced vibrations. *Journal of fluids and structures, 27*(5), 648-658.

Bearman, P., & Zdravkovich, M. (1978). Flow around a circular cylinder near a plane boundary. *Journal of Fluid Mechanics, 89*(01), 33-47.

Behara, S., & Sotiropoulos, F. (2016). Vortex-induced vibrations of an elastically mounted sphere: The effects of Reynolds number and reduced velocity. *Journal of fluids and structures, 66*, 54-68.

Benitz, M., Carlson, D., Seyed-Aghazadeh, B., Modarres-Sadeghi, Y., Lackner, M., & Schmidt, D. (2016). CFD simulations and experimental measurements of flow past free-surface piercing, finite length cylinders with varying aspect ratios. *Computers & Fluids, 136*, 247-259.

Bin, J., LUO, X.-w., PENG, X.-x., & WU, Y.-l. (2013). Three-dimensional large eddy simulation and vorticity analysis of unsteady cavitating flow around a twisted hydrofoil. *Journal of Hydrodynamics, Ser. B, 25*(4), 510-519.

Bishop, R., & Hassan, A. (1964). *The lift and drag forces on a circular cylinder oscillating in a flowing fluid.* Paper presented at the Proceedings of the Royal Society of London A: Mathematical, Physical and Engineering Sciences.

Blackburn, H. M., Govardhan, R., & Williamson, C. (2001). A complementary numerical and physical investigation of vortex-induced vibration. *Journal of fluids and structures, 15*(3-4), 481-488.

Blazek, J. (2015). *Computational fluid dynamics: principles and applications*: Butterworth-Heinemann.

Bloor, M. S. (1964). The transition to turbulence in the wake of a circular cylinder. *Journal of Fluid Mechanics, 19*(02), 290-304.

Bouard, R., & Coutanceau, M. (1980). The early stage of development of the wake behind an impulsively started cylinder for 40< Re< 10 4. *Journal of Fluid Mechanics, 101*(03), 583-607.

Bourdier, S. (2008). *Vortex-Induced Vibrations of a non-linearly supported rigid cylinder.* University of Southampton.

Boussinesq, J. (1877). Th éorie de l'écoulement tourbillant (theories of swirling flow), mé m. prés. par div. savantsa l'acad. *Sci. Paris, 23*.

Braza, M., Chassaing, P., & Minh, H. H. (1986). Numerical study and physical analysis of the pressure and velocity fields in the near wake of a circular cylinder. *Journal of Fluid Mechanics, 165*, 79-130.

Breuer, M. (1998a). Large eddy simulation of the subcritical flow past a circular cylinder: numerical and modeling aspects. *International Journal for Numerical Methods in Fluids, 28*(9), 1281-1302.

Breuer, M. (1998b). Numerical and modeling influences on large eddy simulations for the flow past a circular cylinder. *International Journal of Heat and Fluid Flow, 19*(5), 512-521.

Brika, D., & Laneville, A. (1993). Vortex-induced vibrations of a long flexible circular cylinder. *Journal of Fluid Mechanics, 250*, 481-481.

Cantwell, B., & Coles, D. (1983). An experimental study of entrainment and transport in the turbulent near wake of a circular cylinder. *Journal of Fluid Mechanics, 136*, 321-374.

Chaplin, J., Bearman, P., Huarte, F. H., & Pattenden, R. (2005). Laboratory measurements of vortex-induced vibrations of a vertical tension riser in a stepped current. *Journal of fluids and structures, 21*(1), 3-24.

Colomés, O., Badia, S., & Principe, J. (2016). Mixed finite element methods with convection stabilization for the large eddy simulation of incompressible turbulent flows. *Computer methods in applied mechanics and engineering, 304*, 294-318.

D'Alessandro, V., Montelpare, S., & Ricci, R. (2016). Detached–Eddy Simulations of the flow over a cylinder at Re= 3900 using OpenFOAM. *Computers & Fluids*(136), 152-169.

Deng, G., Piquet, J., Queutey, P., & Visonneau, M. (2014). Vortex-shedding flow predictions with eddy-viscosity models. *Eng. Turb. Modelling and Experiments, 2*, 143-152.

Dennis, S. (1973). *The numerical solution of the vorticity transport equation*. Paper presented at the Proceedings of the third international conference on numerical methods in fluid mechanics.

Dong, Karniadakis, G., Ekmekci, A., & Rockwell, D. (2006). A combined direct numerical simulation–particle image velocimetry study of the turbulent near wake. *Journal of Fluid Mechanics, 569*, 185-207.

Dong, & Karniadakis, G. E. (2005). DNS of flow past a stationary and oscillating cylinder at. *Journal of fluids and structures, 20*(4), 519-531.

Dryden, H. L., & Hill, G. C. (1930). *Wind pressure on circular cylinders and chimneys*: US Government Printing Office.

Fang, Y. Y., & Han, Z. L. (2011). *Numerical experimental research on the hydrodynamic performance of flow around a three dimensional circular cylinder*. Paper presented at the Applied Mechanics and Materials.

Feng, C. (1968). MS Thesis.

Ferziger, J. H., & Peric, M. (2012). *Computational methods for fluid dynamics*: Springer Science & Business Media.

Ferziger, J. H., Peric, M., & Leonard, A. (1997). Computational methods for fluid dynamics: AIP.

Fornberg, B. (1985). Steady viscous flow past a circular cylinder up to Reynolds number 600. *Journal of Computational Physics, 61*(2), 297-320.

Franke, J., & Frank, W. (2002). Large eddy simulation of the flow past a circular cylinder at Re D= 3900. *Journal of Wind Engineering and Industrial Aerodynamics, 90*(10), 1191-1206.

Fröhlich, J., & Rodi, W. (2002). Introduction to large eddy simulation of turbulent flows. *Closure strategies for turbulent and transitional flows, 1*(8), 197-224.

Fröhlich, J., Rodi, W., Kessler, P., Parpais, S., Bertoglio, J., & Laurence, D. (1998). Large eddy simulation of flow around circular cylinders on structured and unstructured grids *Numerical Flow Simulation I* (pp. 319-338): Springer.

Gabbai, R., & Benaroya, H. (2005). An overview of modeling and experiments of vortex-induced vibration of circular cylinders. *Journal of Sound and Vibration, 282*(3), 575-616.

Germano, M., Piomelli, U., Moin, P., & Cabot, W. H. (1990). *A dynamic subgrid-scale eddy viscosity model*. Paper presented at the Studying Turbulence Using Numerical Simulation Databases. 3: Proceedings of the 1990 Summer Program.

Germano, M., Piomelli, U., Moin, P., & Cabot, W. H. (1991). A dynamic subgrid-scale eddy viscosity model. *Physics of Fluids A: Fluid Dynamics (1989-1993), 3*(7), 1760-1765.

Gopalkrishnan, R. (1993). *Vortex-induced forces on oscillating bluff cylinders*. DTIC Document.

Govardhan, R., & Williamson, C. (2000). Modes of vortex formation and frequency response of a freely vibrating cylinder. *Journal of Fluid Mechanics, 420*, 85-130.

Griffin. (1972). Flow near self-excited and forced vibrating circular cylinders. *Journal of Engineering for Industry, 94*(2), 539-547.

Griffin, & Ramberg. (1975). On vortex strength and drag in bluff body wakes. *Journal of Fluid Mechanics, 69*(Part 4), 721-728.

Griffin, O., Skop, R., & Koopmann, G. (1973). The vortex-excited resonant vibrations of circular cylinders. *Journal of Sound and Vibration, 31*(2), 235IN231-249IN233.

Guilmineau, E., & Queutey, P. (2004). Numerical simulation of vortex-induced vibration of a circular cylinder with low mass-damping in a turbulent flow. *Journal of fluids and structures, 19*(4), 449-466.

He, X., & Doolen, G. D. (1997). Lattice Boltzmann method on a curvilinear coordinate system: Vortex shedding behind a circular cylinder. *Physical Review E, 56*(1), 434.

Heggernes, K. K. (2005). *Numerical simulation of three-dimensional viscous flow around marine structures*. (Ph. D, Thesis).

Henderson, R. D. (1995). Details of the drag curve near the onset of vortex shedding. *Physics of Fluids, 7*(9), 2102-2104.

Hinze, J. O. (1970). *Turbulence*. Newyork: McGraw-Hill Publishing Co.

Hoffman, J., Jansson, J., Jansson, N., & De Abreu, R. V. (2015). Towards a parameter-free method for high Reynolds number turbulent flow simulation based on adaptive finite element approximation. *Computer methods in applied mechanics and engineering, 288*, 60-74.

Hover, F., Miller, S., & Triantafyllou, M. (1997). Vortex-induced vibration of marine cables: experiments using force feedback. *Journal of fluids and structures, 11*(3), 307-326.

Islam, S. U., Zhou, C., Shah, A., & Xie, P. (2012). Numerical simulation of flow past rectangular cylinders with different aspect ratios using the incompressible lattice Boltzmann method. *Journal of Mechanical Science and Technology, 26*(4), 1027.

Jauvtis, N., & Williamson, C. (2004). The effect of two degrees of freedom on vortex-induced vibration at low mass and damping. *Journal of Fluid Mechanics, 509*, 23-62.

Jordan, S. A. (2002). Investigation of the cylinder separated shear-layer physics by large-eddy simulation. *International Journal of Heat and Fluid Flow, 23*(1), 1-12.

Khalak, & Williamson. (1996). Dynamics of a hydroelastic cylinder with very low mass and damping. *Journal of fluids and structures, 10*(5), 455-472.

Khalak, & Williamson. (1997a). Fluid forces and dynamics of a hydroelastic structure with very low mass and damping. *Journal of fluids and structures, 11*(8), 973-982.

Khalak, & Williamson. (1997b). Investigation of relative effects of mass and damping in vortex-induced vibration of a circular cylinder. *Journal of Wind Engineering and Industrial Aerodynamics, 69*, 341-350.

Khalak, & Williamson. (1999). Motions, forces and mode transitions in vortex-induced vibrations at low mass-damping. *Journal of fluids and structures, 13*(7-8), 813-851.

Khashehchi, M., Abdi, I. A., & Hooman, K. (2015). Characteristics of the wake behind a heated cylinder in relatively high Reynolds number. *International Journal of Heat and Mass Transfer, 86*, 589-599.

Kim, Y.-H., Vandiver, J., & Holler, R. (1986). Vortex-induced vibration and drag coefficients of long cables subjected to sheared flows. *ASME J. Energy Resour. Technol, 108*, 77-83.

Kiu, K., Stappenbelt, B., & Thiagarajan, K. (2011). Effects of uniform surface roughness on vortex-induced vibration of towed vertical cylinders. *Journal of Sound and Vibration, 330*(20), 4753-4763.

Kondo, N., & Yamada, S. (1995). Third-order upwind finite element computation of the incompressible Navier-Stokes equations Part I. Computation of flow around rectangular cylinders. *Computer methods in applied mechanics and engineering, 127*(1), 87-97.

Kravchenko, A. G., & Moin, P. (2000). Numerical studies of flow over a circular cylinder at ReD= 3900. *Physics of Fluids (1994-present), 12*(2), 403-417.

Laroussi, M., Djebbi, M., & Moussa, M. (2014). Triggering vortex shedding for flow past circular cylinder by acting on initial conditions: A numerical study. *Computers & Fluids, 101*, 194-207.

Launder, B., Reece, G. J., & Rodi, W. (1975). Progress in the development of a Reynolds-stress turbulence closure. *Journal of Fluid Mechanics, 68*(3), 537-566.

Launder, B., & Spalding, D. Lectures in mathematical models of turbulence, 1972: Academic Press, London, England.

Li, Li, J., & Liu, S. (2014). *Numerical simulation of vortex-induced vibration of a circular cylinder at low mass and damping with different turbulent models.* Paper presented at the OCEANS 2014-TAIPEI.

Li, Y., Chan, C., Mei, B., & Zhu, Z. (2015). LES of incompressible heat and fluid flows past a square cylinder at high Reynolds numbers. *International Journal of Computational Fluid Dynamics, 29*(3-5), 272-285.

Liangjie, M., Qingyou, L., & Shouwei, Z. (2014). Experimental study of the vortex-induced vibration of drilling risers under the shear flow with the same shear parameter at the different Reynolds numbers. *PloS one, 9*(8), e104806.

Liaw, K. (2005). *Simulation of flow around bluff bodies and bridge deck sections using CFD.* University of Nottingham.

Lie, H., Larsen, C., & Vandiver, J. (1997). *Vortex induced vibrations of long marine risers; model test in a rotating rig.* Paper presented at the Proceedings of the International conference on offshore mechanics and arctic engineering.

Lilly, D. K. (1992). A proposed modification of the Germano subgrid-scale closure method. *Physics of Fluids A: Fluid Dynamics (1989-1993), 4*(3), 633-635.

Lin, J.-C., Towfighi, J., & Rockwell, D. (1995). Instantaneous structure of the near-wake of a circular cylinder: on the effect of Reynolds number. *Journal of fluids and structures, 9*(4), 409-418.

Linke, W. (1931). New measurements on aerodynamics of cylinders particularly their friction resistance. *Phys. Z, 32*, 900.

Lu, X., Dalton, C., & Zhang, J. (1997). Application of large eddy simulation to flow past a circular cylinder. *Journal of Offshore Mechanics and Arctic Engineering, 119*(4), 219-225.

Lysenko, D. A., Ertesvåg, I. S., & Rian, K. E. (2012). Large-eddy simulation of the flow over a circular cylinder at Reynolds number 3900 using the OpenFOAM toolbox. *Flow, turbulence and combustion, 89*(4), 491-518.

Lysenko, D. A., Ertesvåg, I. S., & Rian, K. E. (2014). Large-eddy simulation of the flow over a circular cylinder at Reynolds number 2× 104. *Flow, turbulence and combustion, 92*(3), 673-698.

Ma, X., Karamanos, G.-S., & Karniadakis, G. (2000). Dynamics and low-dimensionality of a turbulent near wake. *Journal of Fluid Mechanics, 410*, 29-65.

Mani, A., Moin, P., & Wang, M. (2009). Computational study of optical distortions by separated shear layers and turbulent wakes. *Journal of Fluid Mechanics, 625*, 273-298.

Mannini, C., Šoda, A., & Schewe, G. (2010). Unsteady RANS modelling of flow past a rectangular cylinder: Investigation of Reynolds number effects. *Computers & Fluids, 39*(9), 1609-1624.

Meneghini, J., & Bearman, P. (1995). Numerical simulation of high amplitude oscillatory flow about a circular cylinder. *Journal of fluids and structures, 9*(4), 435-455.

Menter, F. R. (1994). Two-equation eddy-viscosity turbulence models for engineering applications. *AIAA journal, 32*(8), 1598-1605.

Meyer, M., Hickel, S., & Adams, N. (2010). Assessment of implicit large-eddy simulation with a conservative immersed interface method for turbulent cylinder flow. *International Journal of Heat and Fluid Flow, 31*(3), 368-377.

Mimeau, C., Cottet, G.-H., & Mortazavi, I. (2016). Direct numerical simulations of three-dimensional flows past obstacles with a vortex penalization method. *Computers & Fluids, 136*, 331-347.

Mittal, & Moin. (1997). Suitability of upwind-biased finite difference schemes for large-eddy simulation of turbulent flows. *AIAA journal, 35*(8), 1415-1417.

Mittal, R., & Moin, P. (1997). Suitability of Upwind-Biased Finite Difference Schemes for Large-Eddy Simulation of Turbulent Flows (tn). *AIAA Journal-American Institute of Aeronautics and Astronautics, 35*(8), 1415-1416.

Mittal, S., Kumar, V., & Raghuvanshi, A. (1997). Unsteady incompressible flows past two cylinders in tandem and staggered arrangements. *International Journal for Numerical Methods in Fluids, 25*(11), 1315-1344.

Morgans, R., Dally, B., Nathan, G., Lanspeary, P., & Fletcher, D. (1999). *Application of the revised Wilcox (1998) k-ω turbulence model to a jet in co-flow.* Paper presented at the Second International Conference on CFD in the Mineral and Process Industries, Melbourne, Australia.

Morkovin. (1964). *Flow around circular cylinder—a kaleidoscope of challenging fluid phenomena.* Paper presented at the ASME Symposium on Fully Separated Flows.

Nguyen, V.-T., & Nguyen, H. H. (2016). Detached eddy simulations of flow induced vibrations of circular cylinders at high Reynolds numbers. *Journal of fluids and structures, 63*, 103-119.

Niemann, H.-J., & Hölscher, N. (1990). A review of recent experiments on the flow past circular cylinders. *Journal of Wind Engineering and Industrial Aerodynamics, 33*(1), 197-209.

Nieuwstadt, F., & Keller, H. (1973). Viscous flow past circular cylinders. *Computers & Fluids, 1*(1), 59-71.

Noca, F., Park, H., & Gharib, M. (1998). *Vortex formation length of a circular cylinder (300< Re< 4000) using DPIV.* Paper presented at the Proceedings of ASME Fluids Engineering Division Summer Meeting.

Norberg. (1987). Effects of Reynolds number and a low-intensity freestream turbulence on the flow around a circular cylinder. *Chalmers University, Goteborg, Sweden, Technological Publications, 87*(2).

Norberg. (1994). An experimental investigation of the flow around a circular cylinder: influence of aspect ratio. *Journal of Fluid Mechanics, 258*, 287-316.

Norberg. (2003). Fluctuating lift on a circular cylinder: review and new measurements. *Journal of fluids and structures, 17*(1), 57-96.

Ong, & Wallace. (1996). The velocity field of the turbulent very near wake of a circular cylinder. *Experiments in fluids, 20*(6), 441-453.

Ong, M. C., Utnes, T., Holmedal, L. E., Myrhaug, D., & Pettersen, B. (2009). Numerical simulation of flow around a smooth circular cylinder at very high Reynolds numbers. *Marine Structures, 22*(2), 142-153.

Ongoren, A., & Rockwell, D. (1988). Flow structure from an oscillating cylinder Part 1. Mechanisms of phase shift and recovery in the near wake. *Journal of Fluid Mechanics, 191*, 197-223.

Ouvrard, H., Koobus, B., Dervieux, A., & Salvetti, M. V. (2010). Classical and variational multiscale LES of the flow around a circular cylinder on unstructured grids. *Computers & Fluids, 39*(7), 1083-1094.

Pan, Z., Cui, W., & Miao, Q. (2007). Numerical simulation of vortex-induced vibration of a circular cylinder at low mass-damping using RANS code. *Journal of fluids and structures, 23*(1), 23-37.

Pang, A. L. J., Skote, M., & Lim, S. Y. (2016). Modelling high Re flow around a 2D cylindrical bluff body using the k-ω (SST) turbulence model. *Progress in Computational Fluid Dynamics, an International Journal, 16*(1), 48-57.

Park, N., Lee, S., Lee, J., & Choi, H. (2006). A dynamic subgrid-scale eddy viscosity model with a global model coefficient. *Physics of Fluids, 18*(12), 125109.

Parkinson, G. (1989). Phenomena and modelling of flow-induced vibrations of bluff bodies. *Progress in Aerospace Sciences, 26*(2), 169-224.

Parnaudeau, P., Carlier, J., Heitz, D., & Lamballais, E. (2008). Experimental and numerical studies of the flow over a circular cylinder at Reynolds number 3900. *Physics of Fluids (1994-present), 20*(8), 085101.

Perry, A., Chong, M., & Lim, T. (1982). The vortex-shedding process behind two-dimensional bluff bodies. *Journal of Fluid Mechanics, 116*, 77-90.

Placzek, A., Sigrist, J.-F., & Hamdouni, A. (2009). Numerical simulation of an oscillating cylinder in a cross-flow at low Reynolds number: forced and free oscillations. *Computers & Fluids, 38*(1), 80-100.

Pope, S. B. (2001). Turbulent flows: IOP Publishing.

Prsic, M. A., Ong, M. C., Pettersen, B., & Myrhaug, D. (2014). Large Eddy Simulations of flow around a smooth circular cylinder in a uniform current in the subcritical flow regime. *Ocean Engineering, 77*, 61-73.

Qun, W., Chen, H.-x., & Zheng, M. (2016). An hybrid RANS/LES model for simulation of complex turbulent flow. *Journal of Hydrodynamics, Ser. B, 28*(5), 811-820.

Rajani, B., Kandasamy, A., & Majumdar, S. (2012). On the reliability of eddy viscosity based turbulence models in predicting turbulent flow past a circular cylinder using URANS approach. *Journal of Applied Fluid Mechanics, 5*(11), 67-79.

Rajani, B., Kandasamy, A., & Majumdar, S. (2016). LES of Flow past Circular Cylinder at Re= 3900. *Journal of Applied Fluid Mechanics, 9*(3).

Rodi, W., Ferziger, J., Breuer, M., & Pourquie, M. (1997). Status of large eddy simulation: results of a workshop. *Transactions-American Society of Mechanical Engineers Journal of Fluids Engineering, 119*, 248-262.

Roshko, A. (1961). Experiments on the flow past a circular cylinder at very high Reynolds number. *Journal of Fluid Mechanics, 10*(03), 345-356.

Sainsbury, R., & King, D. (1971). The flow induced oscillation of marine structures. *Proceedings of the Institution of Civil Engineers, 49*(3), 269-302.

Sarpkaya, T. (1979). Vortex-induced oscillations. *Journal of applied mechanics, 46*(2), 241-258.

Sarpkaya, T. (2004). A critical review of the intrinsic nature of vortex-induced vibrations. *Journal of fluids and structures, 19*(4), 389-447.

Schewe, G. (1983). On the force fluctuations acting on a circular cylinder in crossflow from subcritical up to transcritical Reynolds numbers. *Journal of Fluid Mechanics, 133*, 265-285.

Shao, J., & Zhang, C. (2006). Numerical analysis of the flow around a circular cylinder using RANS and LES. *International Journal of Computational Fluid Dynamics, 20*(5), 301-307.

Shih, Liou, W. W., Shabbir, A., Yang, Z., & Zhu, J. (1995). *A new k-ϵ eddy viscosity model for high reynolds number turbulent flows*. Computers & Fluids, (24, 3).

Shimada, K., & Ishihara, T. (2002). Application of a modified k–ε model to the prediction of aerodynamic characteristics of rectangular cross-section cylinders. *Journal of fluids and structures, 16*(4), 465-485.

Singh, S. P., & Chatterjee, D. (2014). Impact of transverse shear on vortex induced vibrations of a circular cylinder at low Reynolds numbers. *Computers & Fluids, 93*, 61-73.

Singha, S., Nagarajan, K. K., & Sinhamahapatra, K. (2016). Numerical study of two-dimensional flow around two side-by-side circular cylinders at low Reynolds numbers. *Physics of Fluids (1994-present), 28*(5), 053603.

Skaug, L. (1998). New designs advance spar technology into deeper water. *Oil & gas journal, 96*(44), 47-47.

Smagorinsky, J. (1963). General circulation experiments with the primitive equations: I. The basic experiment. *Monthly weather review, 91*(3), 99-164.

Sohankar, A. (2006). Flow over a bluff body from moderate to high Reynolds numbers using large eddy simulation. *Computers & Fluids, 35*(10), 1154-1168.

Spalart, P. R. (2000). Strategies for turbulence modelling and simulations. *International Journal of Heat and Fluid Flow, 21*(3), 252-263.

Stansby, P. (1976). The locking-on of vortex shedding due to the cross-stream vibration of circular cylinders in uniform and shear flows. *Journal of Fluid Mechanics, 74*(4), 641-665.

Starr, M. (2012). High-order methods for steady, unsteady and transitional flow over a cylinder.

Stoesser, T. (2001). *Development and validation of a CFD-code for turbulent open-channel flows.* University of Bristol.

Stringer, R., Zang, J., & Hillis, A. (2014). Unsteady RANS computations of flow around a circular cylinder for a wide range of Reynolds numbers. *Ocean Engineering, 87*, 1-9.

Stroud, K. A. (1990). *Further engineering mathematics: programmes and problems*: Springer.

Sumer, B. M., & Fredsøe, J. (1997). *Hydrodynamics around cylindrical structures*: World Scientific.

Sumer, B. M., & Fredsøe, J. (2006). *Hydrodynamics around cylindrical strucures* (Vol. 26): World scientific.

Sumner, D. (2010). Two circular cylinders in cross-flow: a review. *Journal of fluids and structures, 26*(6), 849-899.

Szepessy, S., & Bearman, P. (1992). Aspect ratio and end plate effects on vortex shedding from a circular cylinder. *Journal of Fluid Mechanics, 234*, 191-217.

Takami, H., & Keller, H. B. (1969). Steady Two-Dimensional Viscous Flow of an Incompressible Fluid past a Circular Cylinder. *The Physics of Fluids, 12*(12), II-51-II-56.

Tao, X. (2015). A general framework for verification and validation of large eddy simulations. *Journal of Hydrodynamics, Ser. B, 27*(2), 163-175.

Termekes, H., & Lumley, J. (1972). A First Course in Turbulence. *MIT Press, Cambridge, Mass, 22*, 63-88.

Thom, A. (1929). *An investigation of fluid flow in two dimensions*: HM Stationery Office.

Townsend, A. (1949). The fully developed wake of a circular cylinder. *Australian Journal of Chemistry, 2*(4), 451-468.

Tremblay, Manhart, M., & Friedrich, R. (2002). LES of flow around a circular cylinder at a subcritical Reynolds number with cartesian grids *Advances in LES of Complex flows* (pp. 133-150): Springer.

Tremblay, F. (2001). *Direct and large-eddy simulation of flow around a circular cylinder at subcritical Reynolds numbers.* Ph. D. dissertation, Fachgebiet Strömungsmechanik, Technische Univerität München, Munich, Germany.

Trias, F., Gorobets, A., & Oliva, A. (2015). Turbulent flow around a square cylinder at Reynolds number 22,000: a DNS study. *Computers & Fluids, 123*, 87-98.

Tu, J., Zhou, D., Bao, Y., Ma, J., Lu, J., & Han, Z. (2015). Flow-induced vibrations of two circular cylinders in tandem with shear flow at low Reynolds number. *Journal of fluids and structures, 59*, 224-251.

Tutar, M., & Holdø, A. E. (2000). Large eddy simulation of a smooth circular cylinder oscillating normal to a uniform flow. *Journal of fluids engineering, 122*(4), 694-702.

Vandiver, J. K. (1983). *Drag coefficients of long flexible cylinders.* Paper presented at the Offshore technology conference.

Vandiver, J. K., Allen, D., & Li, L. (1996). The occurrence of lock-in under highly sheared conditions. *Journal of fluids and structures, 10*(5), 555-561.

Versteeg, H., & Malalasekera, W. (1995). An introduction to computational fluid dynamics: Harlow, England: Prentice Hall.

Versteeg, H. K., & Malalasekera, W. (2007). *An introduction to computational fluid dynamics: the finite volume method*: Pearson Education.

Wilcox, D. C. (1998). *Turbulence modeling for CFD* (Vol. 2): DCW industries La Canada, CA.

Williamson. (1989). Oblique and parallel modes of vortex shedding in the wake of a circular cylinder at low Reynolds numbers. *Journal of Fluid Mechanics, 206*, 579-627.

Williamson. (1996). Vortex dynamics in the cylinder wake. *Annual review of fluid mechanics, 28*(1), 477-539.

Williamson, & Govardhan. (2008). A brief review of recent results in vortex-induced vibrations. *Journal of Wind Engineering and Industrial Aerodynamics, 96*(6), 713-735.

Williamson, & Roshko. (1988). Vortex formation in the wake of an oscillating cylinder. *Journal of fluids and structures, 2*(4), 355-381.

Wissink, & Rodi. (2008). Large-scale computations of flow around a circular cylinder *High Performance Computing on Vector Systems 2007* (pp. 71-81): Springer.

Wood, J. N., De Nayer, G., Schmidt, S., & Breuer, M. (2016). Experimental Investigation and Large-Eddy Simulation of the Turbulent Flow past a Smooth and Rigid Hemisphere. *Flow, turbulence and combustion*, 1-41.

Wootton, L., Warner, M., Sainsbury, R., & Cooper, D. (1972). Oscillation of piles in marine structures. *Construction Industry Research and Information Association (CIRIA), Report, 41*.

Wornom, S., Ouvrard, H., Salvetti, M. V., Koobus, B., & Dervieux, A. (2011). Variational multiscale large-eddy simulations of the flow past a circular cylinder: Reynolds number effects. *Computers & Fluids, 47*(1), 44-50.

Wu, X., Ge, F., & Hong, Y. (2012). A review of recent studies on vortex-induced vibrations of long slender cylinders. *Journal of fluids and structures, 28*, 292-308.

Yakhot, V., & Orszag, S. A. (1986). Renormalization group analysis of turbulence. I. Basic theory. *Journal of scientific computing, 1*(1), 3-51.

Yamada, H., Kuwata, Y., Osaka, H., & Kageyama, Y. (1980). Turbulence measurements in a two-dimensional turbulent wake. *Technology reports of the Yamaguchi University, 2*(4), 329-339.

Young, M., & Ooi, A. (2007). *Comparative Assessment of LES and URANS for Flow Over a Cylinder at a Reynolds Number of 3900.* Paper presented at the 16th Australasian Fluid Mechanics Conference (AFMC).

Zdravkovich, M. (1990). Conceptual overview of laminar and turbulent flows past smooth and rough circular cylinders. *Journal of Wind Engineering and Industrial Aerodynamics, 33*(1-2), 53-62.

Zdravkovich, M. (1997). Flow around circular cylinders; vol. i fundamentals. *Journal of Fluid Mechanics, 350*(1), 377-378.

Zhang, H., YANG, J.-m., XIAO, L.-f., & LÜ, H.-n. (2015). Large-eddy simulation of the flow past both finite and infinite circular cylinders at Re= 3900. *Journal of Hydrodynamics, Ser. B, 27*(2), 195-203.

Zhao, X., Cheng, D., Zhang, D., & Hu, Z. (2016). Numerical study of low-Reynolds-number flow past two tandem square cylinders with varying incident angles of the downstream one using a CIP-based model. *Ocean Engineering, 121*, 414-421.

LIST OF PUBLICATIONS

- ISI indexed Journal Articles

1. **Khan NB**, Ibrahim Z, Nguyen LTT, Javed MF, Jameel M (2017) Numerical investigation of the vortex-induced vibration of an elastically mounted circular cylinder at high Reynolds number (Re = 10^4) and low mass ratio using the RANS code. *PLoS ONE* 12(10): e0185832. https://doi.org/10.1371/journal.pone.0185832 **(Published-Q1)**

2. **Khan, N. B**., Ibrahim, Z., Khan, M. I., Hayat, T., & Javed, M. F. (2018). VIV study of an elastically mounted cylinder having low mass-damping ratio using RANS model. *International Journal of Heat and Mass Transfer, 121*, 309-314. **(Published-Q1)**

3. **Khan, N. B**., Ibrahim, Z., Bin Mohamad Badry, A. B., Jameel, M., & Javed, M. F. (2018). Numerical investigation of flow around cylinder at Reynolds number= 3900 with large eddy simulation technique: Effect of spanwise length and mesh resolution. *Proceedings of the Institution of Mechanical Engineers, Part M: Journal of Engineering for the Maritime Environment*, 1475090217751326 **(Published-Q2)**

4. **Khan, N. B**., & Ibrahim, Z. (2018). Numerical investigation of vortex-induced vibration of an elastically mounted circular cylinder with One-degree of freedom at high Reynolds number using different turbulent models. *Proceedings of the Institution of Mechanical Engineers, Part M: Journal of Engineering for the Maritime Environment*, 1475090217751992. **(Pubished-Q2)**

5. **Khan, N. B**., Abid, M**.,** Jameel, M., & Wajid, H. A. (2015). Joint strength of gasketed bolted pipe flange joint under combined internal pressure plus axial load with different (industrial and ASME) bolt-up strategy.

Proceedings of the Institution of Mechanical Engineers, Part E: Journal of Process Mechanical Engineering, 0954408915614460 **(Published-Q2)**

6. **Niaz B Khan**, Zainah Ibrahim, Oyejobi, Damilola. O, Khaled Ghaedi, Large eddy simulation of flow around circular cylinder at Reynolds number =3900: Impact of averaging time on the accuracy of statistical quantities **(Q1-under review)**

- Conference proceedings

1. **Niaz B Khan**, Zainah Ibrahim, Muhammad Faisal Javed *Numerical investigation of the vortex-induced vibration of an elastically mounted circular cylinder having low mass ratio using the RANS code*, The 2017 World congress on Advances in Structural Engineering and Mechanics (ASEM17), 28th August -1 september, 2017, Ilsan (Seoul), Korea.

2. **Khan, N. B**., Jameel, M., Badry, A. B. B. M., & Ibrahim, Z. B. (2016). *Numerical Study of Flow Around a Smooth Circular Cylinder at Reynold Number= 3900 With Large Eddy Simulation Using CFD Code.* Paper presented at the ASME 2016 35th International Conference on Ocean, Offshore and Arctic Engineering.